

DISSERTATION

SUBMITTED TO THE
COMBINED FACULTY OF NATURAL SCIENCES AND
MATHEMATICS
OF HEIDELBERG UNIVERSITY, GERMANY
FOR THE DEGREE OF
DOCTOR OF NATURAL SCIENCES

Put forward by

Martin Braß

Born in Speyer, Germany

Oral examination: 13 January 2021

Ab initio calculations of the electron capture spectrum in ^{163}Ho

Martin Braß

Referees: PROF. DR. MAURITS W. HAVERKORT
PROF. DR. KLAUS BLAUM

Abstract

Neutrino masses can be determined by measuring how released energies in electron capture decay of ^{163}Ho are distributed between created Neutrino and daughter atom. Therefore, theoretical calculations of the energy spectrum are necessary and are performed in this thesis by means of ab initio methods.

Using techniques from core-level spectroscopy like exact diagonalization and configuration interaction, these calculations are capable of explaining and reproducing experimentally observed spectral features including dominant resonances, multiplet structures and energy-dependent, asymmetric line-broadening due to the Auger-Meitner effect. While multiplets and resonances can be described by bound states, broadening is treated in terms of a self-energy describing coupling between those bound states and unbound states having continuous energy spectrum. Calculations are compared to experimental data and the totally released energy, or Q-value, is determined using Bayesian parameter estimation. A different approach to determine Q is Penning-trap mass-spectroscopy. There, the mass difference between ionized mother and daughter atom is measured, which needs to be corrected for binding energies of the ions to determine the Q-value of neutral atoms. A scheme for binding energy determination is presented and applied to $^{187}\text{Re}^{29+}$ and $^{187}\text{Os}^{29+}$ which may serve as a system for accuracy bench-marking of calculations and measurements.

Zusammenfassung

Durch das Messen der bei Elektroneneinfang in ^{163}Ho freigesetzten Energie und deren Verteilung zwischen erzeugtem Neutrino und Tochteratom ist es möglich Neutrino-Massen zu bestimmen. Dafür sind Berechnungen des Energiespektrums notwendig und werden in dieser Arbeit mittels ab initio Methoden durchgeführt.

Unter Verwendung von Techniken aus der core-level Spektroskopie, wie exakter Diagonalisierung und Konfigurationswechselwirkung, können diese Rechnungen die experimentell beobachteten spektralen Merkmale – insbesondere dominante Resonanzen, Multiplets und energieabhängige, asymmetrische, durch den Auger-Meitner Effekt entstandene Linienverbreiterung – reproduzieren und erklären. Während gebundene Zustände Multiplets und Resonanzen beschreiben, wird die Linienverbreiterung durch eine Selbstenergie bestimmt, welche die Kopplung zwischen jenen gebundenen Zuständen und ungebundenen Zuständen mit kontinuierlichem Energiespektrum beinhaltet. Die Berechnungen werden mit experimentell gewonnenen Daten verglichen und die gesamte, beim Zerfall freigesetzte Energie, der Q-Wert, wird mittels bayesscher Parameterbestimmung ermittelt. Eine weitere Methode zur Bestimmung von Q ist Massenspektroskopie mittels Penningfalle, wobei die Massendifferenz von ionisiertem Mutter- und Tochteratom gemessen wird. Diese muss bezüglich der Bindungsenergie der Ionen korrigiert werden, um den Q-Wert neutraler Atome zu erhalten. Eine Methode zur Bestimmung der Bindungsenergie wird präsentiert und auf $^{187}\text{Re}^{29+}$ und $^{187}\text{Os}^{29+}$ angewandt, welche zur Genauigkeitsbestimmung von Theorie und Experiment verwendet werden können.

Contents

1. Introduction	1
1.1. Neutrinos guiding towards new physics	3
1.2. Determination of Neutrino masses	5
1.2.1. Determination of neutrino masses from nuclear decay	6
1.2.2. Measurement principle for the electron capture spectrum in ^{163}Ho performed by ECHO	9
1.3. Theoretical descriptions of the electron capture spectrum in ^{163}Ho	10
1.4. Electron capture in medicine	14
2. Theory of electron capture spectroscopy	17
2.1. Calculating spectra: Fermi's golden rule vs Kubo's formula	17
2.2. An effective Hamiltonian	19
2.3. Neutrino masses and oscillations	22
2.4. From fields to bound atomic orbitals	24
2.4.1. Kohn-Sham orbitals as single particle basis	25
2.4.2. Dirac Hamiltonian on a Kohn-Sham basis	27
2.4.3. Mutual electronic interactions on a Kohn-Sham basis	27
2.4.4. Weak Hamiltonian	29
2.5. Spectral function	31
3. Numerical Methods	37
3.1. Configuration interaction	38
3.2. Lanczos' algorithm	39
3.3. Lanczos and CI	42
4. Bound state resonances in the electron capture spectrum	45
4.1. How to calculate the electron capture spectrum	45
4.2. Determination of the Q-value	51
4.3. Outlook: Hyperfine interaction	53
5. Unbound states and line-broadening	57
5.1. The Auger-Meitner effect	57
5.2. A single-particle basis made of eigen-differentials	58
5.3. Self-energy	62
5.4. How to calculate self-energy and spectrum	66
5.5. Outlook: Fluorescence	70

6. Broadening due to Auger-Meitner effect in x-ray spectroscopy	73
6.1. X-ray absorption spectroscopy	74
6.2. Resonant inelastic x-ray spectroscopy	77
6.3. Outlook: Including the chemical environment	79
7. Highly charged ions	83
7.1. Determination of a meta-stable state's excitation energy	83
7.2. Binding energies	86
8. Rotated spherical harmonics	89
8.1. Proof of existence	90
8.2. Construction of rotated spherical harmonics	91
9. Summary	95
A. Weak interaction on spherical basis	99
B. List of publications	107
Bibliography	109
Acknowledgments	117

1. Introduction

Nowadays, Neutrinos are the only fundamental particles with unknown masses. Hence, it is of great interest of particle physics and cosmology to determine these. Besides many different other methods, electron capture spectroscopy is one approach to tackle this quest. What kind of spectrum does this technique observe? How is it related to masses of Neutrinos? To understand what experimentalists from diverse collaborations are measuring, how this spectrum can be explained with the aid of theoretical calculations and how to infer information about Neutrino masses from the combined experimental and theoretical data, we need to study nuclear decay and atomic relaxation processes. At the heart of this thesis there is the calculation of the electron capture spectrum of ^{163}Ho from first principles, i. e. starting from the fundamental physical laws we know. This calculation shall support the experimental search for Neutrino masses by providing an unbiased description of the spectral shape.

Electron capture is a nuclear decay process in which an electron, bound to an atom, is captured by the atom's nucleus thereby transforming a proton into a neutron. This changes the atom's nuclear charge by one unit of elementary electric charge and creates a hole in the inner atomic shell from which the electron has been captured. In the case of ^{163}Ho this implies the transition from the Ho ground state to an excited state of the ^{163}Dy daughter atom. The daughter atom can de-excite into its ground-state by filling the created hole with an electron from its valence shell and releasing the energy of the latter. If only mother and daughter atom were involved in this process, the energy released by the daughter would always be the same, namely the difference between the masses of mother and daughter, which is called Q-value. However, electron capture is a decay mediated by the weak force and hence a neutrino is involved. This particle is created during the decay and carries some amount of the totally released energy Q . The remaining energy is stored in the excitation of the daughter and can be measured when the atom de-excites. In section 1.2 we describe how such measurements are performed.

As the neutrino can obtain an arbitrary energy larger than its rest-mass m_ν and smaller than the Q-value, the de-excitation energy assumes values between zero and $Q - m_\nu c^2$. If electron capture decay is observed multiple times, one can make a histogram of the observed energies, which resembles the so-called electron capture spectrum.

From this discussion it is clear that the endpoint of the electron capture spectrum depends on the created neutrino's mass. However, neutrinos are not simply created in a state with definite mass. Instead they are in a superposition of at least three mass-states which oscillate in time. As a consequence the full spectrum is given by the sum of multiple spectra, one for each mass-state. While this affects the electron

1. Introduction

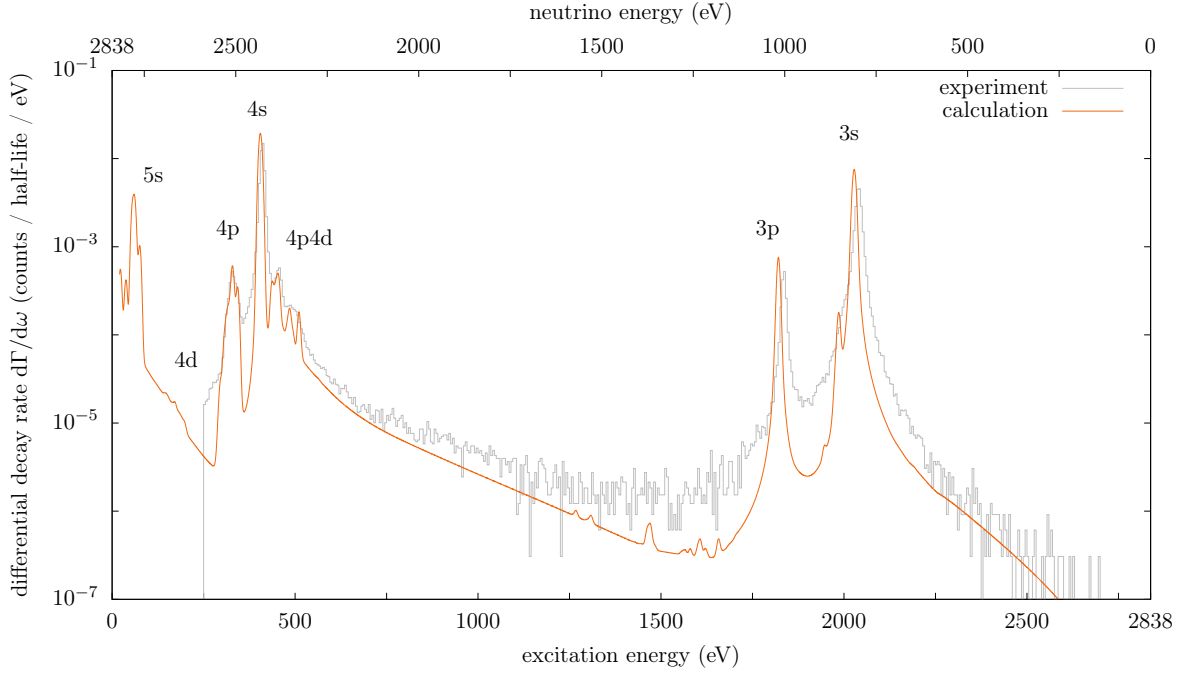


Figure 1.1.: Electron capture decay of ^{163}Ho results in an excited daughter ^{163}Dy atom. Excitations are due to single holes in electronic shells as a result of electron capture or due to multiple holes as a result of relaxation processes subsequent to electron capture. Experimentally a spectrum can be obtained by measuring these excitation energies from multiple decays. Resonances are labeled according to holes in inner shells of the corresponding excited state of Dy. Taken from [3].

capture spectrum only marginally, the observation of neutrino oscillations lead to the discovery of neutrinos being massive particles as we will outline in section 1.1. There we give a brief historical overview of discoveries concerning neutrinos. This is meant to demonstrate how neutrinos have been involved in the development of our understanding of particle physics and thereby motivates the experimental search for their masses. The mechanism of neutrino flavor oscillations is discussed in section 2.3.

While the decay itself is subject to nuclear physics, the following de-excitation is governed almost purely by atomic dynamics. Coulomb interaction between the remaining electrons leads to interesting spectral features as shown in figure 1.1.

One observes sharp and broad resonances, satellite structures close to the N_1 (4s) edge, as well as large wings on the side towards higher energies of peaks. To reproduce these features and predict further excitations which are hidden in the experimental data due to the given detector resolution, accurate electronic structure calculations have to be performed.

In section 1.3 we summarize approaches for calculating the electron capture spec-

trum by different authors and outline differences to this work. The mathematical framework on which all calculations in this thesis are based is presented in chapter 2 and the applied numerical methods can be found in chapter 3. Calculated electron capture spectra, results and further methodological details related to publications [1–3] are presented in chapters 4 and 5. While chapter 4 deals with those spectral features which can be attributed to locally bound states, line-broadening of resonances due to unbound states is studied in chapter 5.

To show that the methods developed in these chapters have a broader range of application, we apply them to x-ray spectroscopy of Nickel oxide in chapter 6. At the end of the chapter an outlook describes how to improve calculations of both x-ray and electron capture spectra by inclusion of the chemical environment in which the probed atom resides.

Precise determination of the Q-value is also important to infer neutrino masses from an electron capture spectrum and can be done using Penning trap mass-spectroscopy [5]. This method determines the Q-value for highly charged ions instead of neutral atoms. To obtain Q of the latter, one has to correct for the binding energy of the removed electrons. Hence, in chapter 7 we present a method to estimate this energy as well as the uncertainties accompanying the involved calculations.

In chapter 8 we present a group-theoretic proof that a basis for atomic orbitals, corresponding to any irreducible representation of the group of rotations $SO(3)$, can always be chosen such that the basis-orbitals have the same shape and differ in orientation only.

A summary of this thesis can be found in chapter 9.

1.1. Neutrinos guiding towards new physics

From the beginning of the last century and until today neutrinos have been and are being involved in discoveries of physical phenomena and developments of theoretical models. In 1914, eighteen years after Henry Becquerel, Marie and Pierre Curie discovered nuclear decay, James Chadwick provided the first experimental evidence showing that the energy spectrum of an electron emitted in β -decay is continuous [6]. This posed a great enigma, since conservation of energy and momentum requires that the decay of one nucleus into another via emission of a single particle leads to a discrete energy-spectrum of the latter, as it has been observed for α -decay. Furthermore, it has been found that certain nuclei change their angular momentum by an integer multiple of Planck's constant \hbar during β -decay, although the outgoing electron has half-integer angular momentum. Apparently, also conservation of angular momentum seems to be violated [7].

Different solutions for these observations have been developed, where Wolfgang Pauli's suggestion was the successful one. He proposed the existence of a new particle that participates in β -decay, thereby allowing for a continuous energy-spectrum alongside the validity of the conservation laws mentioned above [7]. In 1934 Enrico Fermi acted on Pauli's idea and developed a mathematical description of β -decay,

1. Introduction

which used the concept of second quantization and creation of particles out of energy. Not only did he coin the name of Pauli's particle as neutrino, he also took the first step in the development of a theory of weak interaction and outlined how to infer the neutrino's mass from a β -spectrum [8], which is nowadays the basis of modern neutrino-mass experiments [9–15].

From here, it took 22 years until in 1956 Clyde Cowan and coworkers finally detected the neutrino [16]. The reason it took so long is in the faint nature of weak-interaction. The Neutrino, being an electrically neutral particle, interacts via weak-processes only, making experimental detection difficult. However, until its detection the neutrino and Fermi's theory of β -decay sparked further research - both experimental and theoretical.

After nuclear β^+ -decay via emission of a positron had been discovered, in 1934 Gian-Carlo Wick proposed an extension of Fermi's theory that predicts nuclear decay via capture of an electron of the decaying atom [17]. The experimental confirmation followed only three years later. Luis Alvarez produced radioactive Vanadium ^{48}V by deuterium-bombardment of Titanium. The former decays both via electron capture and β^+ decay. Hence, he was able to measure the ratio of created γ -rays from produced positrons and created x-rays from electron capture of K electrons. The agreement of this ratio with theoretical predictions proved the existence of decay via electron capture [18].

Ettore Majorana raised a problem in 1937 that remains unsolved until today. He provided a new quantization scheme describing Fermions which are their own anti-particles, so called Majorana-Fermions, and claimed that there is no reason to distinguish between neutrino and anti-neutrino [20]. So far there is no experimental evidence proving or contradicting the hypothesis of neutrinos being their own anti-particles. However, the consequences of this are testable via the ongoing search for neutrinoless double β -decay. If neutrinos are Majorana-Fermions, it should be possible to detect nuclear decay where two neutrons decay into two protons while emitting two electrons and no neutrinos. Such processes have half-lives larger than 10^{25} years [21–24] and violate conservation of lepton-number as there are two more leptons after the decay than before.

The violation of lepton-number conservation manifests itself in many other hypotheses different from Majorana's one. After the muon neutrino had been discovered in pion decays $\pi^\pm \rightarrow \mu^\pm + \nu_\mu/\bar{\nu}_\mu$ [25], Bruno Pontecorvo discussed the possibility of neutrino-flavor oscillations $\nu_e \leftrightarrow \nu_\mu$ as mechanism leading to violation of lepton-number conservation in 1967, noting that these oscillations would lead to a reduced flux of solar electron-neutrinos compared to the total flux of neutrinos created in our sun [26].

The next year Raymond Davis Jr. and his team of the Homestake experiment discovered a puzzle for which Pontecorvo has already provided the solution. In an underground goldmine they investigated the reaction $^{37}\text{Cl} + \nu_e \rightarrow ^{37}\text{Ar} + e^-$ to measure the solar-neutrino flux and found it to be smaller than predicted from the solar standard model [27]. However, experimental verification of neutrino-flavor oscillations to be the cause for the observed deviation took 33 years.

In 2001 the collaboration of the Sudbury Neutrino Observatory published measurements of the total neutrino flux from the sun and of the solar electron-neutrino flux [28]. While the latter has been determined via a deuterium reaction $d + \nu_e \rightarrow 2p + e^-$ which is sensitive to electron-neutrinos only, the former has been estimated via elastic scattering $\nu_x + e^- \rightarrow \nu_x + e^-$. Observing that the total flux is larger than the one of electron-neutrinos confirmed that neutrinos of different flavors are present, although not created within the carbon-nitrogen-oxygen (CNO) cycle of the sun. Furthermore, the total flux agreed with calculations from the solar standard model, thereby solving the solar neutrino problem.

The above and further experiments [29–31] established flavor oscillations which are only possible if neutrinos are massive particles and their flavor-eigenstates are not eigenstates of the Hamiltonian. This raises questions concerning which absolute values the neutrino masses take, whether they are of Dirac or Majorana nature and whether there are additional massive sterile neutrinos.

The latter have been and are still investigated in different experiments with neutrinos from nuclear reactors and serve as possible explanation for observed reduction of anti-neutrinos [32] or neutrinos [33–35] compared to theoretical predictions. The appearance of anti-electron-neutrinos from anti-muon-neutrino beams created in accelerators may also be attributed to sterile neutrinos [36–38]. However, statistical analyses show that for certain classes of sterile neutrino models there are tensions in the models' parameter spaces between data from reactor- and accelerator-neutrinos [39,40]. Furthermore, improved calculations reduced the discrepancy between observed and predicted neutrinos in reactor experiments based on Gallium detectors [41,42]. This demonstrates how neutrinos do not only indicate physics beyond established models, as we saw in their history of more than a century, but also challenge the precision of calculations and approximations within these models.

The latter aspect is crucial for most of the former, current and future neutrino experiments as they rely on precise calculations within well tested atomic, molecular, solid-state, nuclear or cosmological models. It is the aim of this thesis to study how well existing methods from atomic and condensed matter physics can be applied to describe the spectral shape of electron capture decay in ^{163}Ho and how insights from these methods affect the determination of the neutrino masses.

1.2. Determination of Neutrino masses

The previous section outlined discoveries around neutrinos as well as open questions which include the mass-eigenvalues $\{m_{\nu_i} \mid i = 1\dots 3\}$ of the neutrino mass-eigenstates. Obtaining these values is not only important from the metrological viewpoint, but also impacts observations in other fields of physics as Cosmology for instance. Neutrinos interact gravitationally and hence affect structure formation [44,45]. Thus, it is possible to infer upper bounds for the sum of the neutrino masses $\sum_{i=1}^3 m_{\nu_i} < 0.172$ eV at 95% confidence level from cosmological data [46].

Another approach to estimate bounds for the neutrino masses is given by neutri-

1. Introduction

neutrinoless double beta decay. There are nuclei ${}^A_Z X$ with even numbers of protons (Z) and neutrons ($A - Z$) which undergo normal double beta decay ${}^A_Z X \rightarrow {}^A_{Z-2} Y + 2e^- + 2\bar{\nu}_e$ instead of single beta decay, because due to pairing forces the former is energetically favorable while the latter is not [47]. Here two neutrinos are created as opposed to neutrinoless double beta decay. The energy difference between the groundstates of mother and daughter nucleus – called Q-value – is divided between those created neutrinos, electrons and the remaining nucleus. The energy spectrum of the electrons is continuous. If however, Majorana’s hypothesis is true such that neutrinos are their own anti-particles, double beta decay is possible without creation of neutrinos. In that case the electrons’ energy spectrum would be a peak around the Q-value [49]. Hence, one could distinguish between normal double beta decay and neutrinoless double beta decay. The decay rate of the latter is proportional to $m_{\beta\beta} \equiv \left| \sum_{i=1}^3 m_{\nu_i} U_{ei}^2 \right|$ [47], where U denotes the Pontecorvo-Maki-Nakagawa-Sakata (PMNS) matrix [97]. Recent studies have set an upper limit $m_{\beta\beta} < 0.15$ eV at 90% confidence level [50].

While this method to determine neutrino masses necessarily assumes Majorana’s hypothesis to be true, cosmological results are dependent on models of the early universe. However, model independent studies of neutrino masses are possible, too. These are based on determining kinematic properties of the created neutrinos.

One proposed approach is to measure the time of flight of neutrinos created in a supernova. Together with the neutrinos’ energies and the distance to the exploding star it would in principle be possible to determine neutrino masses [51,52]. A further study claims that with detectors currently in development it will be possible to reach a sensitivity that allows to probe the neutrinos’ mass hierarchy [53].

Further kinematics based approaches rely on measuring energy spectra, i.e. differential decay rates, from nuclear decay. One of these is electron capture spectroscopy. In this thesis we are calculating the electron capture spectrum of ${}^{163}\text{Ho}$. Hence, in the following section we outline how this can be used to determine the neutrino masses.

1.2.1. Determination of neutrino masses from nuclear decay

Neutrinos are created as products of weak decay. Especially important for the determination of neutrino masses are β -decay ${}^A_Z X \rightarrow {}^A_{Z+1} Y + e^- + \bar{\nu}_e$ and electron capture ${}^A_Z X + e^- \rightarrow {}^A_{Z-1} Y + \nu_e$. In the former channel, nucleus X with Z protons and atomic number A decays to nucleus Y via transforming a neutron into a proton and emitting an electron together with its anti-neutrino. The latter channel describes how a proton in the nucleus of an atom captures an electron out of one of the inner atomic shells (core shells) and becomes a neutron while emitting an electron-neutrino.

For these processes to occur in nature the energy difference, or Q-value $Q = E_0({}^A_Z X) - E_0({}^A_{Z\pm 1} Y)$, between the ground-states of mother and daughter atom has to be positive. This released energy is distributed between the decay products. In the case of electron capture the only products are neutrino and daughter atom which is in an excited state and releases its energy in further relaxation processes via emission of photons or Auger-Meitner electrons.

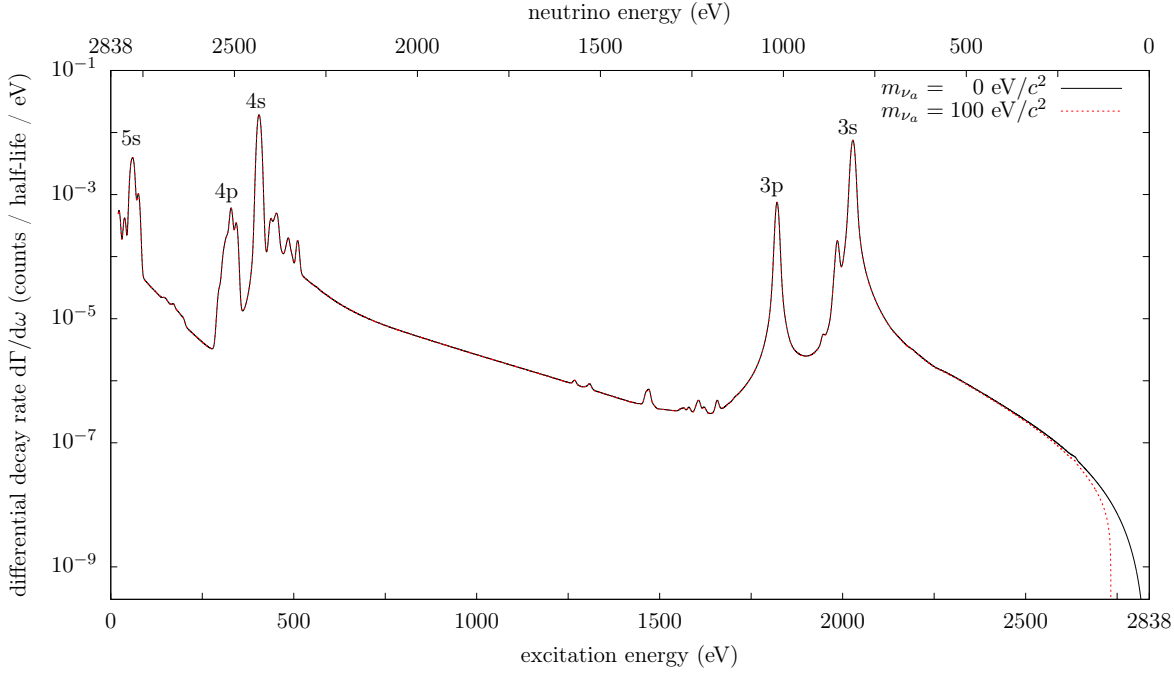


Figure 1.2.: Calculated electron capture spectrum of ^{163}Ho for vanishing and non-zero neutrino masses. The lower axis describes the excitation energy of the Dy daughter atom, which can be measured with a calorimeter and the upper axis denotes the energy of the neutrino created during EC which is determined by the difference between the Q-value and the excitation energy. Most dominant resonances belong to excitations of single holes which have been created by electron capture from the labeled orbitals. The spectral endpoint region is strongly affected by neutrino masses.

Measuring the energy ω of all products except the neutrino allows to calculate the neutrino energy $E_\nu = Q - \omega$. Performing such measurements multiple times, one can estimate the differential decay rate $\frac{d\Gamma}{d\omega}(\omega)$, i.e the number of decays per energy ω per unit of time. $\frac{d\Gamma}{d\omega}(\omega)$ is also often referred to as the energy spectrum of β -electrons in the case of β -decay, or as the electron capture spectrum of the mother atom.

This quantity is proportional to the number of states $\propto E_\nu p_\nu$ available for the created neutrino with energy E_ν and momentum $p_\nu = \sqrt{E_\nu^2 - m_\nu^2 c^2}/c$. Therefore the differential decay rate is sensitive to the neutrino mass near $\omega = Q - m_\nu c^2$ [8]. In particular the mass determines the endpoint of the differential decay rate beyond which no decays can occur, since out of the totally available energy Q at least the amount of the neutrinos rest-mass has to be put into the creation of the neutrino and thus cannot be assigned to the other decay products. This is illustrated in figure 1.2

Hence, neutrino masses can be determined by measuring differential decay rates, or energy spectra, of such decays and compare them to theoretical predictions of the corresponding spectral shape [8, 61]. This can be done for instance by fitting a cal-

1. Introduction

culated spectral shape with neutrino mass and Q-value as free parameter to experimental data. Besides high statistics and high energy resolution in experimental decay rates, one also needs highly accurate numerical calculations of the spectral shape in order to be sensitive to neutrino masses below $1 \text{ eV}/c^2$ [14].

This is challenging since the spectrum has many different features as shown in figure 1.2. These include major peaks which emerge from states with a hole in one of the inner shells created by the nucleus capturing an electron. Further smaller structures are present due to relaxation processes subsequent to electron capture. These involve the created core hole to scatter between different orbitals and can even lead to shake up of other electrons into unoccupied orbitals yielding states with multiple core holes. Ionization can occur when an electron is removed from the Dy daughter atom via the Auger-Meitner effect. This leads to line-broadening of the resonances as well as the observed increased, high energy tails.

All these spectral features have to be well understood, especially their impact on the endpoint region in order to extract the neutrino masses from such a spectrum. We will discuss them in chapters 4 and 5.

In practice, the neutrino is not created in one of the mass-eigenstates, but in a flavor-eigenstate instead, as described in section 1.1. The latter is a superposition of the former and hence one does not measure a single spectrum, but the sum of three spectra, each weighted with the corresponding phase space factor for a neutrino of mass m_{ν_i} , $i = 1..3$, and the overlap between mass- and flavor eigenstate $|U_{ei}|^2$. The mathematical aspects of neutrino masses and oscillations are described in section 2.3, the spectral shape in the endpoint region is discussed in section 2.5 and 5.4.

Currently there are two isotopes under investigation for neutrino mass determination. One is tritium ${}^3_1\text{H}$ which undergoes β -decay and the other is Holmium ${}^{163}_{67}\text{Ho}$ decaying via electron capture. While the underlying principle to determine neutrino masses are the same in both cases, the methods of measuring the energy spectra are quite different.

The Mainz experiment [9], the Troitsk experiment [10] and KATRIN [11] measure integrated β -spectra of molecular tritium with the help of MAC-E-Filters (Magnetic Adiabatic Collimation combined with an Electrostatic Filter). Project 8 uses Cyclotron radiation emission spectroscopy to obtain a differential β -spectrum of atomic tritium [12]. HOLMES uses transition edge sensors [13] and ECHo uses metallic magnetic calorimeters [14] to measure the electron capture spectrum in ${}^{163}\text{Ho}$, i. e. the decay energy stored in atomic excitations of the daughter atom.

${}^{163}\text{Ho}$ is chosen for electron capture spectroscopy due to its good properties. It has a low electron capture Q-value among those isotopes with half-lives that are long enough to perform precise measurements of the spectrum. On the other hand the half-life of ${}^{163}\text{Ho}$ is not too long such that it is possible create Ho samples with high activities. These properties assure that the measured electron capture spectrum has high statistics in the endpoint region which is most sensitive to neutrino masses [14].

Since this work is part of the ECHo project, we briefly describe it in the following section. However, our calculations are independent of the measurement principle and can be equally well applied to other experiments that measure electron capture

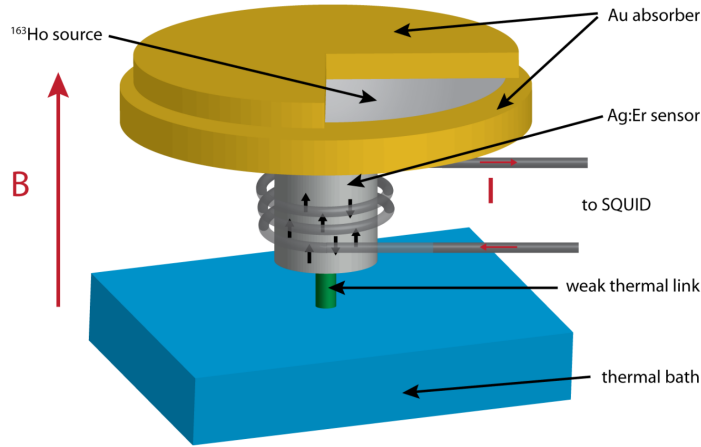


Figure 1.3.: Simplified scheme of a metallic magnetic calorimeter taken from [43].

spectra.

1.2.2. Measurement principle for the electron capture spectrum in ^{163}Ho performed by ECHO

The electron capture spectrum, or differential decay rate $\frac{d\Gamma}{d\omega}$, of ^{163}Ho is defined as the number of decays per energy per unit of time. Experimentally it can be obtained by measuring the energy ω of the excited decay-product ^{163}Dy for multiple decays and counting how many of these decay-events fall into a certain energy window $[\omega, \omega + d\omega]$. This way one obtains a histogram which resembles the differential decay rate in the limit of infinite number of measurements and infinitesimally small binning $d\omega$.

Hence, every experimental setup, that aims to be sensitive to the neutrino masses, needs a good energy resolution, in order not to smear out the spectral endpoint region, as well as a ^{163}Ho source with high activity. Furthermore, at high activities it is crucial to resolve two events in time, that occur almost simultaneously, to avoid that the sum of the energies of these events is assigned to a single event at higher energies. This is called unresolved pile-up and can be circumvented by a good time resolution of the detector.

As the energy of the excited daughter atom is released in relaxation processes, subsequent to electron capture, via photons or Auger-Meitner electrons, it is necessary to have a detector with high quantum efficiency, to avoid energy loss which can occur by not detecting portions of the released photons or Auger-Meitner electrons.

The metallic magnetic calorimeters designed by the ECHO collaboration fulfill these properties to good extent [14]. The operational principles are described in [14] and will be briefly summarized here. A simplified scheme of the detector is shown in figure 1.3.

1. Introduction

Using ion implantation, the radioactive ^{163}Ho source can be embedded within gold. The latter serves as an absorber for all of the released energy from the decay process which is not distributed to the neutrino. It is connected to a paramagnetic sensor made of gold (Au) or silver (Ag) doped with erbium (Er) and is enclosed by a superconducting coil. This system is coupled to a thermal bath via a weak thermal link. Every release of energy within the absorber material results in a change of its temperature which is approximately proportional to the released energy. Applying a constant magnetic field leads to magnetization of the Ag:Er sensor, which depends on the absorber's temperature according to Curie's law. If the induced change in temperature is small compared to the temperature of the heat bath, the change in magnetization is approximately proportional to the change in temperature and hence energy. This results in an induced current within the superconducting coil which in turn is inductively coupled to a superconducting quantum interference device (SQUID) that turns the induced current into a change in voltage. As the latter change is approximately proportional to all the former changes in current, magnetization, temperature and energy, one can determine the deposited energy from decaying Ho in the absorber by measuring the voltage change of the SQUID. In practice there are small non-linearities in these steps from energy to voltage, such that the functional dependence between the latter two is calibrated with a polynomial of second order [14].

The thickness of the absorber determines the quantum efficiency of the detector, which is nearly 1 in the ECHO experiment [14]. This implies that all of the daughter atom's excitation energy can be measured without losses and consequently the obtained spectrum is insensitive to the type of de-excitation channel, whether via photons, or Auger-Meitner electrons. For calculations of the differential decay rate this is a welcome simplification as there is no need to consider branching ratios of different relaxation channels of the daughter atom.

The next section gives an overview how such calculations have been performed by different authors in the past and outlines some of the differences between their approaches and the one pursued in this work.

1.3. Theoretical descriptions of the electron capture spectrum in ^{163}Ho

Alvaro De Rújula proposed to determine neutrino masses by calorimetric measurement of the electron capture spectrum of ^{163}Ho in 1981 [61]. The next year he published a theoretical calculation of the spectral shape [62]. Years later he [63, 64] and further authors like Amand Fäßler [65–68] or Hamish Robertson [69] developed this calculation further with the aim of reaching higher accuracy and better agreement with experimental data. This section describes these approaches, their differences and results, and thereby relates them to the calculations of this work.

All these previous calculations have in common that they describe the electron cap-

1.3. Theoretical descriptions of the electron capture spectrum in ^{163}Ho

ture spectrum, or differential decay rate $d\Gamma/d\omega$, by Fermi's golden rule [19]

$$\frac{d\Gamma}{d\omega} \propto (Q - \omega) \sum_{i=1}^3 |U_{ei}|^2 \sqrt{(Q - \omega)^2 - m_{\nu_i}^2} \sum_f \gamma_f \frac{|\langle f | \sum_j \psi_j(R) e_j | g \rangle|^2}{(\omega - E_f)^2 + \frac{\gamma_f^2}{4}}. \quad (1.1)$$

The Q-value Q is the energy difference between the ground-states of Ho and Dy. ω denotes the energy deposited in the calorimeter, i.e. the difference between Q and the energy of the created neutrino. Together with the PMNS matrix U and the masses m_{ν_i} of the neutrino mass-eigenstates, which will be introduced in section 2.3, they form the neutrino phase-space factor in front of the sum over all final states $|f\rangle$ of the Dy daughter atom. It has been assumed that every final state contributes to the spectrum with a lorentzian peak of width γ_f at energy E_f . These latter two parameters are usually taken from experimental data, which is the first difference compared to this work, where we aim to calculate the resonant energies and line-broadenings of excitations from first principles. To illustrate the discussion in the following, we present our calculations of the electron capture spectrum in figure 1.4

Differences between the authors from above are in their selection of final states, taken into account to the sum in (1.1), and in approximations of the matrix-elements $\langle f | \sum_j \psi_j(R) e_j | g \rangle$. Here e_j denotes an annihilation operator that removes an electron in orbital $\psi_j(\mathbf{x})$ from the Ho ground-state $|g\rangle$. The sum runs over all orbitals from which electron capture is most likely, which includes the 3s to 6s and 3p_{1/2} to 5p_{1/2} atomic orbitals. In these matrix-elements the wavefunctions $\psi(R)$ of the orbitals are evaluated at either the nuclear radius R or at the origin, depending on the choice of the authors.

In De Rújula's first description of the electron capture spectrum [62] he considers only final states that involve a single hole in one of the core-orbitals $\{3s, \dots, 6s, 3p_{1/2}, \dots, 5p_{1/2}\}$. He approximates the matrix-elements of these final states $\langle f | \sum_j \psi_j(R) e_j | g \rangle \approx \psi_f(0)$ by the wavefunction, corresponding to the orbital in which the hole has been created, evaluated at the origin. In this framework he calculates the relative intensities of the major resonances and draws conclusions on the sensitivity of calorimetric electron capture experiments with respect to Q-value and neutrino masses.

In a paper from 2014 [65] Amand Fäßler and coworkers calculated the spectrum from the same set of final states, but included overlap and exchange corrections. Therefore, they described ground- and final states by single Slater-determinants. For each final state's electronic configuration they ran a self-consistent, full relativistic Dirac-Fock calculation to obtain the single particle wave-functions from which the corresponding final state Slater-determinant was created. On this basis, they calculated the matrix elements $\langle f | \sum_j \psi_j(R) e_j | g \rangle$ where the orbital wavefunctions have been evaluated at the nuclear radius R . Apart from their claim that overlap and exchange corrections "have a large effect on the form of the spectrum" [65], the authors make the important remark, that configuration interaction leads to additional satellite-structures. This is intensively studied in chapter 4 of this work.

Since satellite-structures were observed in experiment on top of the high energy

1. Introduction

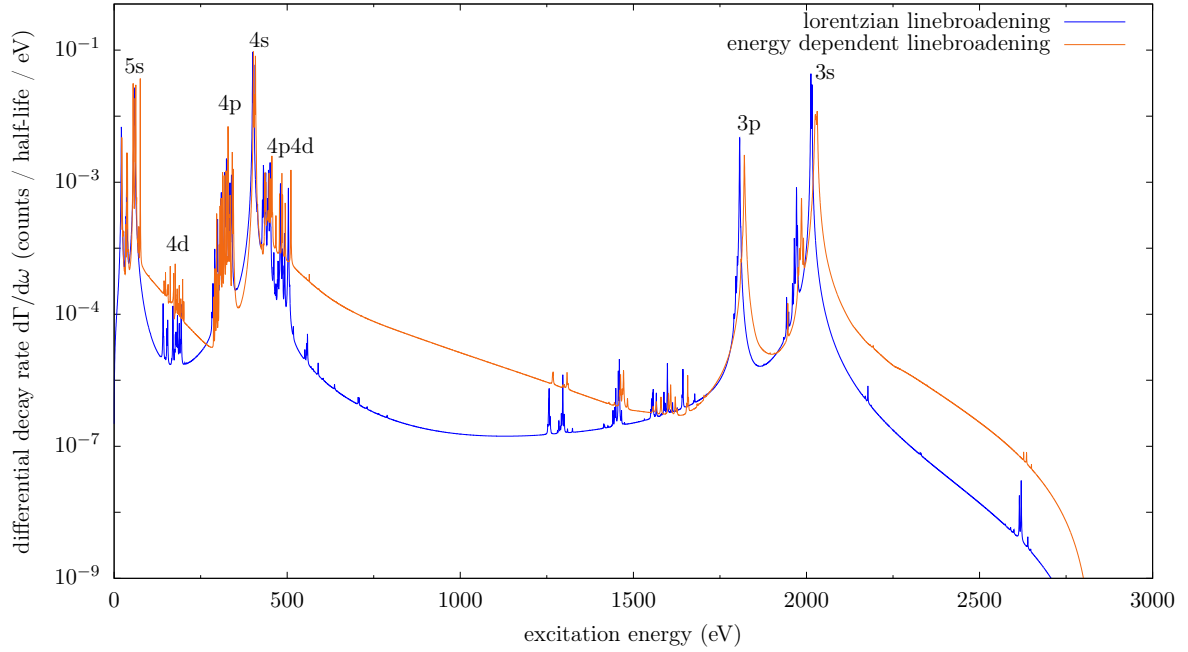


Figure 1.4.: Calculated electron capture spectrum of ^{163}Ho with different levels of theory described in chapter 4 (blue) and chapter 5 (orange). The most dominant resonances belong to excitations of single holes which have been created by electron capture from the labeled orbitals. Relaxation processes can scatter these holes and create smaller resonances corresponding to final states with holes in different orbitals like 4d for instance. The satellite structure to the right of 4s corresponds to final states with two core holes in 4p4d, created by Coster-Kronig transitions subsequent to electron capture. Literature refers to these peaks as shake-up features. While the blue curve assumes lorentzian broadening of all resonances, the orange curve includes shake-off effects – or Auger-Meitner transitions, which lead to energy dependent, asymmetric line-broadening. Taken from [3].

tail of the N_1 (4s) resonance (compare figure 1.4), they necessarily had to be included in the calculations. Thus Robertson [69] and Fäßler [66] added final states with two holes in core shells to the sum in (1.1) and even states with three core-holes [67]. The latter publication concluded that three-hole states have a negligible impact on the spectral shape; the former two publications demonstrated that two-hole states cannot be omitted.

Two problems emerged. First, the predicted two-hole excitations of Robertson [69] and Fäßler [66] disagree as was shown in figure 1 of the latter reference. Second, neither of the calculations were able to explain the observed N_1 (4s) satellite-structure. As shown in figure 1.4 and explained in chapter 4, these satellites are due to final states with two holes – one in 4p and one in the 4d shell – which emerge from the

scattering of one 4d electron into the 4s hole created by electron capture and simultaneously scattering a 4p electron into the 4f valence shell. The above publications strongly underestimated the intensities of these final states or did not include them and hence could not explain the satellite-structure.

The cause for the discrepancy between the two calculations themselves may be in the different approaches used to calculate the matrix elements of the two-hole states in (1.1). Robertson used an approximation within the shake-up and shake-off theory of Carlson and Nestor [70]. Fäßler on the other hand calculated the matrix-elements using single Slater-determinants obtained analogously to [65] as outlined above.

The latter approach becomes problematic if ground- or final state are not representable by a single Slater-determinant. Since this is the case for the Ho ground-state and many excited Dy states, as will be discussed in chapter 3 and 4, we here briefly outline this problem.

Consider two atomic configurations of electrons Ω_g and Ω_f , where the former is a set of N quantum numbers describing state $|g\rangle = \prod_{n \in \Omega_g} e_n^\dagger |0\rangle$ and the latter contains $N - 1$ quantum numbers describing state $|f\rangle = \prod_{n \in \Omega_f} e_n^\dagger |0\rangle$ after electron capture. These states are described in second quantization where e_n^\dagger creates an electron with quantum numbers n out of the vacuum $|0\rangle$. The matrix-element then yields

$$|\langle f | \sum_j \psi_j(R) e_j | g \rangle|^2 = \begin{cases} |\psi_i(R)|^2 & \text{if } \exists i \in \{3s, \dots, 6s, 3p_{1/2}, \dots, 5p_{1/2}\} : \Omega_f \cup \{i\} = \Omega_g \\ 0 & \text{otherwise} \end{cases} \quad (1.2)$$

Therefore, all matrix-elements where the configuration Ω_f differs in more than one quantum number from Ω_g vanish. Hence, two-hole states can only contribute to the spectral shape if either $|f\rangle = \prod_{n' \in \Omega_f} e_{n'}^\dagger |0\rangle$ is given by a different basis of single-particle wavefunctions which are not orthogonal to the basis in which $|g\rangle$ is given, or $|f\rangle$ and $|g\rangle$ are linear combinations of different configurations in the same basis. The former solution is employed by [66], but as soon as ground- or final states are not single Slater-determinant representable, this can lead to errors and hence the states have to be of multi-configurational nature.

So far only final states have been included where electrons were in bound orbitals. However, De Rújula [63, 64] and Fäßler [68] also considered the possibility of Auger-Meitner, or shake-off processes, where, during atomic relaxation after electron capture, electrons are scattered into unbound states, leaving an ionized atom behind. De Rújula uses an approximation analogous to [69, 70] for the calculation of the matrix elements $\langle f | e_j | g \rangle$ for final states with two core-holes and one electron either shaken up to a previously unoccupied bound level, or shaken off into the continuum. In this framework he concludes that "theoretical predictions of the two-hole probabilities do not agree with the data" [64]. Especially the N_1 (4s) satellite-structure cannot be reproduced, probably because the configurations with two holes in 4p and the 4d shell are missing. Furthermore, he remarks that his calculations predict a $M_1 N_{4/5}$ peak (one hole in 3s and one in 4d) which is not seen in experiment.

Fäßler [68] discusses the sensitivity of shake-up probabilities in the framework

1. Introduction

used by De Rújula, and comes to the conclusion that small errors in single-particle wavefunctions may lead to an overestimation of peak heights by two orders of magnitude. This might explain the too high intensity of the $M_1 N_{4/5}$ peak calculated by De Rújula, however, our results from [1] and chapter 4 show that configuration interaction also has an effect on the intensities of two-hole states, which is not negligible.

Another conclusion of Fäßler [68] claims that the contribution of final states where one electron is no longer bound (i. e. has been shaken off) does not affect the spectral shape significantly "and thus can probably not affect the determination of the electron neutrino mass" [68].

In frameworks that treat states as single Slater-determinants and neglect configuration interaction, this may be a valid conclusion. However, in chapter 5 we will show that Auger-Meitner (i. e. shake-off) processes do not only significantly modify the spectral shape, but also increase intensity in the end point region of the spectrum, which implies higher statistics for the determination of the neutrino mass. Furthermore, we will see that these processes determine the shape of the wings of the resonances, thereby allowing for a better understanding of the spectral shape in the end point region. As an outlook this is already presented in figure 1.4 and can be noticed when comparing the different line-shapes of the two spectral curves.

Note that in this work we are not pursuing the above approach (1.1), but are calculating response functions as described in section 2.1. However, there we will show that both approaches are equivalent and we can map one approach onto the other. Differences emerge from different approximations made to calculate the spectrum. This justifies the above comparisons between the work of different authors and ours.

In summary the previous work of different authors described above relies on finding a set of final states that most accurately describe the spectral shape and to optimize the single particle wave functions which serve as a basis for the single Slater-determinant final states. The single-particle basis used in this work is described in section 2.4.1. We will go beyond the single Slater-determinant approximation and include configuration interaction. In this framework, described in chapters 2 - 5, there will be no need to select final states and perform the corresponding sum in (1.1), as our algorithm automatically includes the most dominant electronic configurations, which is outlined in sections 2.1 and 3.2.

1.4. Electron capture in medicine

Besides chemical therapy and surgery, radio therapy is a widely used tool in cancer treatment. Different types of radiation are used to destroy cancerous cells via DNA double strand breaking (DSB). Isotopes that undergo nuclear decay via electron capture have promising properties to be used as radiotherapeutic agents [54–56]. They can be transported into cancerous cells via carrier molecules such that they deposit the energy released during decay in the nucleus of the cell, thereby breaking the DNA double strand and killing the tumor. The deposited energy is often released via Auger-Meitner electrons, created in relaxation processes subsequent to the nuclear

decay. These have low kinetic energies and hence a large stopping power in tissue. Thus, almost all of their energy is deposited within the cancerous cell reducing damage within healthy tissue. The dose of deposited energy in the tumor can be up to four orders of magnitude higher than from an external radiation source [57].

The dose itself is an important quantity when studying biological effects due to radiation in a cell. Hence, computational models have been developed to calculate such doses for a large variety of electron capture isotopes [58–60]. These rely, amongst others, upon methods from atomic, molecular and condensed matter physics to determine transition rates, excitation energies and the Auger electron yield.

The methods described in chapters 2 - 5 are developed to determine the differential decay rate of electron capture in ^{163}Ho , which is insensitive to whether the deposited energy comes from Auger electrons or X-rays. However, these methods are equally well suited to calculate the Auger electron yield and excitation energies for other electron capture isotopes. Hence, besides the search for the neutrino masses this work can also be motivated from the need of accurate models and algorithms in radio therapy.

2. Theory of electron capture spectroscopy

In this chapter the mathematical framework is described which forms the basis of this thesis. An expression for the electron capture spectrum is derived in section 2.1 and the Hamiltonian governing the dynamics of electron capture and atomic de-excitation is introduced in section 2.2. As neutrino masses and mixing of mass eigen-states are central for the endpoint region of the electron capture spectrum, we discuss one possible way of extending the standard model of particle physics to include massive neutrinos and how this leads to oscillations in section 2.3. Before we can present the final form of the spectral function used in numerical calculations and discuss how mixing of mass eigen-states affects the spectral shape in section 2.5, we express the Hamiltonian on a basis of Kohn-Sham orbitals, which is suitable for numerical implementation, in section 2.4.

Throughout this thesis we will use natural units such that the speed of light c Planck's quantum \hbar and the vacuum permittivity ϵ_0 are unity.

2.1. Calculating spectra: Fermi's golden rule vs Kubo's formula

As described in the introduction, electron capture experiments are measuring the differential electron capture nuclear decay rate $\frac{d\Gamma}{d\omega}(\omega)$. It is defined as the number of decays per time $d\Gamma(\omega)$ within a window $[\omega, \omega + d\omega]$ of deposited energy in the micro-calorimeter divided by window size $d\omega$. Thus, ω is the excitation energy of the daughter atom after electron capture, or to put it differently, the difference between the totally released energy Q and the neutrino's energy E_ν .

Electron capture is governed by weak interaction H_W . Treating it as perturbation, there are two common ways to calculate the differential decay rate. The first uses Fermi's golden rule [19] where the asymptotic decay rate for a transition from the Ho ground-state Ψ_{H_0} to a final state Ψ_f is given by

$$R_{\Psi_{H_0} \rightarrow \Psi_f} \propto \delta(E_f - E_0) |\langle \Psi_{H_0} | H_W | \Psi_f(E_f) \rangle|^2 . \quad (2.1)$$

The Dirac $\delta(E_f - E_0)$ ensures that initial ground-state energy E_0 and final state energy E_f are conserved. The final state Ψ_f contains a neutrino, the nuclear wave-function of the daughter atom and its many-body electronic wave-function. To obtain the

2. Theory of electron capture spectroscopy

experimentally measured spectrum, we have to sum over all final states, where the excitation energy of the daughter atom lies within a window $[\omega, \omega + d\omega]$ of deposited energy in the micro-calorimeter

$$\frac{d\Gamma}{d\omega} \propto \sum_{\Psi_f} \delta(\omega - E_{\text{Dy}^*}) R_{\Psi_{\text{Ho}} \rightarrow \Psi_f} \quad (2.2)$$

where $E_{\text{Dy}^*} = E_f - E_\nu$ denotes the excitation energy of the daughter atom. Final states can be expressed as direct products $\Psi_f = \Psi_{\text{Dy}^*} \otimes \Psi_\nu$, since the neutrino interacts via weak force only and is consequently to very good approximation a free particle in the final state. Hence, we separate the sum over final states in neutrino states and atomic states

$$\frac{d\Gamma}{d\omega} \propto \sum_{\Psi_\nu} \delta(Q - w - E_\nu) \sum_{\Psi_{\text{Dy}^*}} \delta(\omega - E_{\text{Dy}^*}) |\langle \Psi_{\text{Ho}} | H_W | \Psi_f(E_f) \rangle|^2 \quad (2.3)$$

The sum over the neutrino final states \sum_{Ψ_ν} involves an integral over the neutrino's momentum, or equivalently its energy E_ν . Performing this integral and using a lorentzian representation of the second δ -function directly results in (1.1). As mentioned earlier, we can choose a second way to calculate the differential decay rate, namely via Kubo's formula. To show that these approaches are equivalent, we now recast the above expression until we arrive at the latter.

Considering that the second sum runs over a complete basis of eigenfunctions of the Hamiltonian H which governs the dynamics of the Dy daughter atom, we can express it as

$$\sum_{\Psi_{\text{Dy}^*}} \langle \Psi_{\text{Ho}} | H_W | \Psi_f(E_f) \rangle \delta(\omega - E_{\text{Dy}^*}) \langle \Psi_f(E_f) | H_W | \Psi_{\text{Ho}} \rangle = \langle \Psi_{\text{Ho}} | (H'_W)^\dagger \delta(\omega - H) H'_W | \Psi_{\text{Ho}} \rangle \quad (2.4)$$

Here we used a representation of unity $\mathbb{1} = \sum_{\Psi_{\text{Dy}^*}} |\Psi_{\text{Dy}^*}\rangle \langle \Psi_{\text{Dy}^*}|$ and that $\Psi_f = \Psi_{\text{Dy}^*} \otimes \Psi_\nu$. Hence, we introduced the shorthand notation $H'_W = (\mathbb{1} \otimes |\Psi_\nu\rangle \langle \Psi_\nu|) H_W$. We can further exploit

$$\frac{1}{\omega + i0} \equiv \lim_{\eta \rightarrow 0^+} \frac{1}{\omega + i\eta} = \mathcal{P} \frac{1}{\omega} - i\pi \delta(\omega) \quad (2.5)$$

where \mathcal{P} denotes Cauchy-Principal value. Therefore, the differential decay rate reads

$$\frac{d\Gamma}{d\omega} \propto -\text{Im} \sum_{\Psi_\nu} \delta(Q - w - E_\nu) \langle \Psi_{\text{Ho}} | (H'_W)^\dagger \frac{1}{\omega + i0 - H} H'_W | \Psi_{\text{Ho}} \rangle \quad (2.6)$$

The above equation (2.6) contains the Fourier transform of a transition rate and from Quantum Field Theory we know that these violate causality [71]. To cure this

problem one subtracts a second propagator

$$\begin{aligned} \frac{d\Gamma}{d\omega} \propto & -\text{Im} \sum_{\Psi_\nu} \delta(Q - \omega - E_\nu) \\ & \times \left(\langle \Psi_{\text{Ho}} | (H'_W)^\dagger \frac{1}{\omega + i0 - H} H'_W | \Psi_{\text{Ho}} \rangle - \langle \Psi_{\text{Ho}} | H'_W \frac{1}{\omega + i0 + H} (H'_W)^\dagger | \Psi_{\text{Ho}} \rangle \right) . \end{aligned} \quad (2.7)$$

The term in brackets is precisely the Fourier-transformed causal response function obtained in linear response theory from Kubo's formula [74] for an instantaneous decay via electron capture

$$G^R(t) = -i\Theta(t) \langle \Psi_{\text{Ho}} | \left[(H'_W)^\dagger(t), H'_W(0) \right] | \Psi_{\text{Ho}} \rangle . \quad (2.8)$$

This shows that, as mentioned in the beginning of this section, there are actually two equivalent ways of calculating the differential decay rate, i.e. the electron capture spectrum. Approach (2.7) using the causal response function has another advantage besides not violating causality as compared to Fermi's golden rule (2.3). The latter involves the evaluation of an infinite sum $\sum_{\Psi_{\text{Dy}^*}}$ over excited final states of the daughter atom. These involve a countably infinite number of electronic configurations in bound states as well as an un-countably infinite number of configurations involving unbound states each of which carry an infinitesimal spectral weight contributing to the differential decay rate. This difficulty has now been reduced to evaluating the Hamiltonian's resolvent $(z - H)^{-1}$ slightly above the real axis, which can be done with numerical methods described in chapter 3.

Hence, we will use (2.7) for our calculations. In the next section we will study the Hamiltonian that governs the dynamics of electron capture and subsequent relaxation of the daughter atom.

2.2. An effective Hamiltonian

An electrically neutral ^{163}Ho atom consists of 67 electrons and protons each as well as 96 neutrons. In order to do an ab initio calculation of the EC spectrum in Ho one has to consider all these particles and their mutual interactions. Although these interactions are well known and described by the electro-weak sector of the standard model of particle physics, the many-body-aspect and quantum mechanical nature of such systems hinder a solution. It is therefore essential to obtain an effective Hamiltonian which allows for a solution of the quantum many-body problem, but still governs all relevant dynamics such that quantitative predictions and comparisons to experimental data are possible. In this section we discuss such an effective Hamiltonian which will be used throughout this thesis. We introduce Dirac's Hamiltonian H_D , which describes kinematics of fermions. Dynamics are included in a low-energy effective electron-electron interaction U_{eff} containing Coulomb repulsion and static, unretarded Breit interaction. Attraction between electrons and the nucleus is accounted

2. Theory of electron capture spectroscopy

for in the Coulomb potential V_C and the electron capture process is governed by an effective weak-interaction Hamiltonian H_W . See [95] for a good introduction to electro-weak interactions in the standard model from which the effective Hamiltonians in this section can be derived.

Weak interaction conserves charge but not particle number. Hence, electron capture is a process that changes the numbers of electrons, protons, neutrons and neutrinos. It is therefore natural to use second quantization to formulate the many-body problem with the help of fields, which can be expanded on creation and annihilation operators.

In this formulation the kinematics of the electrons are encoded in Dirac's Hamiltonian [71]

$$H_D = \int \psi_e^\dagger(\mathbf{x}) \left(-i\gamma^0 \gamma^k \partial_k + \gamma^0 m \right) \psi_e(\mathbf{x}) d^3x \quad . \quad (2.9)$$

$\psi_e(\mathbf{x})$ is a four component Dirac-spinor field whose excitations are electrons. The partial derivative with respect to the k -th spatial coordinate x^k is denoted ∂_k , m is the electron's mass, i the imaginary unit. Sum convention is implied and $(\gamma^\mu)_{\mu=0\dots3}$ denote a representation of Dirac's matrices, which satisfy the anti-commutation relation $\{\gamma^\mu, \gamma^\nu\} = \eta^{\mu\nu}$ with η the Minkowsky metric with signature $(+, -, -, -)$. For explicit calculations in later sections we choose Dirac's representation of the γ -matrices

$$\gamma^0 = \begin{pmatrix} \mathbb{1}_2 & 0 \\ 0 & \mathbb{1}_2 \end{pmatrix} \quad \gamma^k = \begin{pmatrix} 0 & \sigma^k \\ -\sigma^k & 0 \end{pmatrix} \quad . \quad (2.10)$$

$\mathbb{1}_2$ is the two-dimensional identity matrix and σ^k are Pauli's matrices.

Dirac's Hamiltonian (2.9) describes non-interacting, relativistic fermions with momentum \mathbf{k} and dispersion relation $E_k = \sqrt{\mathbf{k}^2 + m^2}$. However, all fermions involved in electron capture are interacting via the electro-weak force which is mediated by gauge bosons. During electron capture a charged W^\pm boson is exchanged between proton and electron, which can be expressed with a tree-level Feynman-diagram

$$----- = -i \int \frac{\eta_{\mu\nu} - q_\mu q_\nu / m_W^2}{q^2 - m_W^2 + i0} e^{-iq(x_1 - x_2)} \frac{d^4q}{(2\pi^4)} \equiv G_{\mu\nu}^W(x_1 - x_2) \quad [72].$$

(2.11)

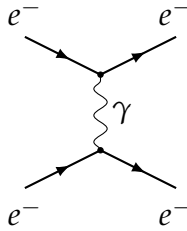
The mass of the W^\pm gauge boson is $m_W = 80.379 \pm 0.012$ GeV [90] which is much larger than the electron capture Q-value of 2.838 ± 0.014 keV [2]. Hence, for the purpose of calculating the electron capture spectrum, the low energy regime $q^2 \ll m_W^2$ is most relevant in which the propagator $G_{\mu\nu}^W(x_1 - x_2)$ becomes proportional to Dirac's δ -distribution $G_{\mu\nu}^W(x_1 - x_2) \propto \eta_{\mu\nu} \delta(x_1 - x_2)$. Thus, the effective weak interaction is

point-like and can be expressed by [93]

$$H_W = \frac{G_W}{\sqrt{2}} \int \bar{\psi}_{\nu_e}(\mathbf{x}) \gamma^\mu (1 - \gamma^5) \psi_e(\mathbf{x}) \bar{\psi}_n(\mathbf{x}) \gamma_\mu (1 - \lambda \gamma^5) \psi_p(\mathbf{x}) d^3x + \text{h.c.} \quad (2.12)$$

As the weak interaction does not couple to right-chiral (also called right-handed) leptons, the projection operator $(1 - \gamma^5)/\sqrt{2}$ enters the above expression, with $\gamma^5 = i\gamma^0\gamma^1\gamma^2\gamma^3$. This operator projects onto the sub-space of left-chiral leptons. For protons and neutrons the situation is different. There the weak interaction has different strengths of vector G_V and axial coupling G_A [93]. This is accounted for by introducing the phenomenological parameter $\lambda \equiv |G_A/G_V| = 1.250 \pm 0.009$ [94].

The weak interaction Hamiltonian H_W (2.12) is responsible for creation of an electronic hole in the Ho ground-state, creating an electron neutrino and transforming a proton of the Ho nucleus into a neutron of the Dy daughter nucleus during electron capture. The subsequent relaxation processes, that determine intensities and positions of spectral resonances, are governed by electromagnetic interaction which is mediated by photons and can also be expressed in terms of a similar tree-level Feynman diagram



$\sim = -i \int \frac{\eta_{\mu\nu}}{q^2 + i0} e^{-iq(x_1 - x_2)} \frac{d^4q}{(2\pi^4)} \equiv G_{\mu\nu}^\gamma(x_1 - x_2)$ [71].

(2.13)

Here $G_{\mu\nu}^\gamma(x_1 - x_2)$ describes the propagation of a mass-less photon, leading to a different interaction in the low-energy regime as compared to (2.12). In this regime the propagator becomes $G_{\mu\nu}^\gamma(x_1 - x_2) \propto \eta_{\mu\nu} \frac{\delta(t_1 - t_2)}{|\mathbf{x}_1 - \mathbf{x}_2|}$ [71] such that one obtains an effective interaction

$$U_{\text{eff}} = \frac{1}{2} \int \bar{\psi}_e(\mathbf{x}_1) \gamma^\mu \psi_e(\mathbf{x}_1) \frac{\alpha}{|\mathbf{x}_1 - \mathbf{x}_2|} \bar{\psi}_e(\mathbf{x}_2) \gamma_\mu \psi_e(\mathbf{x}_2) d^3x_1 d^3x_2 \quad . \quad (2.14)$$

The fine-structure constant is denoted by $\alpha = \frac{e^2}{4\pi\epsilon_0\hbar c}$. As opposed to the weak interaction, the above expression contains both interacting left- and right-chiral particles on equal footing. The effective electro-magnetic interaction includes Coulomb and unretarded Breit-interaction. The former will become especially important for satellite-features in the EC spectrum. The latter only yields minor corrections to the spectrum as discussed in [1].

Note further that (2.14) contains a non-physical self-interaction of the electrons at $\mathbf{x}_1 = \mathbf{x}_2$ where the potential diverges. To remove this divergent self-interaction, we expand (2.14) on atomic orbitals in section 2.4.3 and re-order creation and annihilation

2. Theory of electron capture spectroscopy

operators. This expansion also has the advantage that its numerical evaluation is efficient.

For the electro-magnetic interaction between bound electrons and protons in the nucleus we can use the same expression as in (2.14) and further simplify it. In ^{163}Dy nuclear excitation energies are far above the Q-value. Hence, neither the EC process nor subsequent relaxation will excite the nucleus. Thus we can treat the nucleons as being always in their Ho/Dy nuclear ground-state. Furthermore, the electronic wavelengths will largely exceed the protons' wavelengths such that we can express the effective electron-proton interaction by the well known Coulomb potential

$$V_C = -\alpha \int \psi_e^\dagger(\mathbf{x}) \frac{Z}{|\mathbf{x}|} \psi_e(\mathbf{x}) d^3x \quad (2.15)$$

where $Z = \int \psi_p^\dagger(\mathbf{x}) \psi_p(\mathbf{x}) d^3x$ is the total number of protons.

Within these approximations the effective Hamiltonian that governs electron capture and subsequent relaxation dynamics reads

$$H_{\text{eff}} = H_D + V_C + U_{\text{eff}} + H_W + H_\nu \quad (2.16)$$

It includes the kinematics of the electrons in terms of Dirac's Hamiltonian H_D (2.9), the Coulomb potential V_C (2.15) of the nucleus, an effective, inter-electronic, electro-magnetic interaction U_{eff} (2.14) and the weak-interaction H_W (2.12). The Hamiltonian H_ν for massive neutrinos cannot be deduced from the standard model of particle physics, since only left-chiral neutrinos are present. In the next section we discuss one possible extension of the standard model that includes three massive Dirac-neutrinos. However, further extensions exist that are consistent with current observations [96].

2.3. Neutrino masses and oscillations

In the standard model of particle physics there are three flavors $\{e, \mu, \tau\}$ of massless, left-chiral neutrino fields corresponding to electron-neutrino, muon-neutrino and tauon-neutrino respectively [95,96]. Due to their masslessness, the energy-eigenvalues of differently flavored, non-interacting neutrinos with common momentum are degenerate. Hence, oscillations between different flavors are impossible and one is forced to go beyond the standard model to describe experimentally observed neutrino-flavor-oscillations. The most straight-forward way to do this is to include right-chiral neutrino fields and a Yukawa-coupling to the Higgs-doublet via a flavor-non-diagonal matrix. After spontaneous symmetry-breaking this adds a mass-matrix $\mathbb{M}_{ll'}$ to the Hamiltonian of neutrinos, thereby mixing different neutrino-flavors

$$H_\nu = \sum_{l,l' \in \{e,\mu,\tau\}} \int \bar{\psi}_{\nu_l}(x) (-\delta_{ll'} i \gamma^\mu \partial_\mu + \mathbb{M}_{ll'}) \psi_{\nu_{l'}}(x) d^3x \quad (2.17)$$

Here, we assumed that \mathbb{M} is hermitian and thus we can diagonalize it by a unitary transformation $U \mathbb{M} U^\dagger = \text{diag}(m_1, m_2, m_3)$, where U is the Pontecorvo-Maki-Nakagawa-Sakata matrix [97]. Introducing the fields $\psi_{\nu_a}(x) = \sum_{l \in \{e,\mu,\tau\}} U_{al} \psi_{\nu_l}(x)$ we

obtain a mass-diagonal Hamiltonian for free neutrinos

$$H_V = \sum_{a=1}^3 \int \psi_{\nu_a}^\dagger(\mathbf{x}) \left(-i\gamma^0 \gamma^k \partial_k + \gamma^0 m_a \right) \psi_{\nu_a}(\mathbf{x}) d^3x \quad . \quad (2.18)$$

This describes three massive, fermionic fields which extremize action when obeying Dirac's equation $(i\partial - m)\psi = 0$. Thus we can expand the fields in terms of plane waves times creation and annihilation operators

$$\psi_{\nu_a}(x) = \sum_{s=-\frac{1}{2}}^{\frac{1}{2}} \int u_a(p, s) v_a(p, s) e^{-ipx} + v_a(p, s) \bar{v}_a^\dagger(p, s) e^{ipx} d^3p \quad p^0 = \sqrt{\mathbf{p}^2 + m_a^2} \quad . \quad (2.19)$$

The operator $v_a(p, s)$ is an operator that annihilates a neutrino in mass-eigenstate a with four momentum p and spin s . $\bar{v}_a^\dagger(p, s)$ creates an anti-neutrino respectively. The four-component spinors $u_a(p, s)$ and $v_a(p, s)$ obey $(\gamma_\mu p^\mu - m_a)u = 0 = (\gamma_\mu p^\mu + m_a)v$ [71].

From the above expression we can directly read off the time evolution of a non-interacting flavor eigen-state

$$|v_e, \mathbf{p}, t = 0\rangle = \sum_{a=1}^3 U_{ae} v_a^\dagger(p) |0\rangle \Rightarrow |v_e, \mathbf{p}, t\rangle = \sum_{a=1}^3 U_{ae} e^{i\sqrt{\mathbf{p}^2 + m_a^2} t} |v_a, \mathbf{p}\rangle \quad . \quad (2.20)$$

As the flavor eigenstates are not eigenstates of the non-interacting neutrino Hamiltonian (2.18), one observes oscillations between neutrino flavors.

Let's assume during the CNO cycle of the sun an electron neutrino is created at $t = 0$ in a flavor eigenstate. We can ask how probable it is to detect such neutrinos at $t > 0$ via the channel $\nu_e + n \rightarrow p^+ + e^-$. Of course, this depends on the neutrino capture probability of the detector material, but more importantly it also depends on the probability that the neutrino can be found to be in the electron-flavor eigenstate

$$\begin{aligned} |\langle v_e, \mathbf{p}, t = 0 | v_e, \mathbf{p}, t \rangle|^2 &= \left| \sum_{a=1}^3 |U_{ae}|^2 e^{-i\sqrt{\mathbf{p}^2 + m_a^2} t} \right|^2 \\ &= \sum_{a,b=1}^3 |U_{ae}|^2 |U_{be}|^2 e^{-i(\sqrt{\mathbf{p}^2 + m_a^2} - \sqrt{\mathbf{p}^2 + m_b^2}) t} \quad . \end{aligned} \quad (2.21)$$

Expanding the exponent for small neutrino masses

$$\sqrt{\mathbf{p}^2 + m_a^2} - \sqrt{\mathbf{p}^2 + m_b^2} \approx \frac{m_a^2 - m_b^2}{2|\mathbf{p}|} \equiv \frac{\Delta m_{ab}^2}{2|\mathbf{p}|} \quad (2.22)$$

reveals an oscillation of the probability with frequency $\frac{\Delta m_{ab}^2}{2|\mathbf{p}|}$ [98]. Hence, the detection probability of a neutrino in an electron-flavor eigenstate depends on the time difference between creation and detection or equivalently the distance between source and

2. Theory of electron capture spectroscopy

detector. Thus, in the example of solar neutrinos from the CNO cycle the electron-neutrino flux detected on earth is reduced compared to the predicted flux close to its origin. The total neutrino-flux however is conserved due to unitarity of the PMNS matrix which reflects that the neutrino oscillates between different flavors. These two observations were made by SNO [28] as mentioned in the introduction and they verified neutrino oscillations. The frequency of these oscillations would vanish if all neutrino mass-eigenvalues were degenerate. Hence, from observations one concludes that at least two neutrino masses are different from zero [92].

Note that (2.20) only approximately describes the state of the created neutrino at $t = 0$ [73]. The reason for this can be found in the weak Hamiltonian (2.12) which in our example governs the creation of the electron neutrino. On the basis of massive neutrino fields expression (2.12) reads

$$H_W = \frac{G_W}{\sqrt{2}} \sum_{a=1}^3 U_{ae} \int \bar{\psi}_{\nu_a}(\mathbf{x}) \gamma^\mu (1 - \gamma^5) \psi_e(\mathbf{x}) \bar{\psi}_n(\mathbf{x}) \gamma_\mu (1 - \lambda \gamma^5) \psi_p(\mathbf{x}) d^3x + \text{h.c.} \quad (2.23)$$

where $\sum_{a=1}^3 U_{ae} \psi_{\nu_a}^\dagger$ creates the electron neutrino. In terms of creation and annihilation operators it can be expressed as

$$\begin{aligned} \sum_{a=1}^3 U_{ae} \psi_{\nu_a}^\dagger(\mathbf{x}) &= \sum_{a,s} \int u_a^\dagger(p,s) U_{ae} v_a^\dagger(p,s) e^{-i\mathbf{p}\mathbf{x}} + v_a^\dagger(p,s) U_{ae} \bar{v}_a(p,s) e^{i\mathbf{p}\mathbf{x}} d^3p \\ &\neq \sum_s \int u^\dagger(p,s) \left(\sum_a U_{ae} v_a^\dagger(p,s) \right) e^{-i\mathbf{p}\mathbf{x}} + v^\dagger(p,s) \left(\sum_a U_{ae} \bar{v}_a(p,s) \right) e^{i\mathbf{p}\mathbf{x}} d^3p . \end{aligned} \quad (2.24)$$

The last inequality demonstrates that this process does not simply involve the creation operator $v_e^\dagger \equiv \sum_a U_{ae} v_a^\dagger$ as assumed in (2.20). However, if $|\mathbf{p}| \gg m_a \forall a$ the spinor $u_a(p,s)$ becomes independent of m_a and the above inequality turns into an approximate equality. As the neutrino masses are tiny, this approximation will be valid in many cases. However, this subtlety can be circumvented by directly working with the massive fields and (2.23), which we will do in this work.

This completes the derivation of the effective Hamiltonian represented by fields. In the next section we discuss how to represent the Hamiltonian on a Fock-space basis, which is more suited for numerical implementation.

2.4. From fields to bound atomic orbitals

In the previous sections all operators have been expressed in terms of fields. These are suitable for analytic calculations, for computation of scattering amplitudes and cross-sections involving asymptotically free particles. However, the resonances of the electron capture spectrum correspond to locally bound states and are calculated numerically. Therefore, expanding these fields on a basis of bound atomic orbitals

$$\psi_e(\mathbf{x}) = \sum_\tau \phi_\tau(\mathbf{x}) e_\tau \quad \psi_e^\dagger(\mathbf{x}) = \sum_\tau \phi_\tau^\dagger(\mathbf{x}) e_\tau^\dagger. \quad (2.25)$$

is practical and allows for a more efficient numerical implementation. τ denotes quantum numbers that characterize the atomic orbitals $\phi_\tau(\mathbf{x})$ from which e_τ^\dagger and e_τ create/annihilate an electron. As the fields are four-component spinors, the atomic orbitals have to be the same.

When calculating the electron capture spectrum, we need to truncate the formally infinite sum over quantum numbers τ in the above expansion. Hence, we need to find a basis of atomic orbitals which allows for a truncation that introduces only a small error in the spectrum and alongside contains manage-ably few terms. One way of finding such a basis is density functional theory (DFT) which we briefly describe in the following.

2.4.1. Kohn-Sham orbitals as single particle basis

Density functional theory is based on two theorems found by Pierre Hohenberg and Walter Kohn [76]. For a system of interacting electrons moving in a potential $V(\mathbf{x})$ the first theorem states that this potential is uniquely determined by the density $\rho_{\text{GS}} \equiv \langle \varphi_{\text{GS}} | \psi_e^\dagger(\mathbf{x}) \psi_e(\mathbf{x}) | \varphi_{\text{GS}} \rangle$ of the system's ground-state φ_{GS} . Thus, knowledge of ρ_{GS} implies knowledge of the system's Schrödinger equation and hence of the full system itself - at least in principle.

The second theorem states that for such systems there exists a functional defined on the space of v-representable densities ρ

$$E[\rho] \equiv T[\rho] + \int V(\mathbf{x})\rho(\mathbf{x})d^3x + F[\rho] \quad (2.26)$$

which has a global minimum at $\rho = \rho_{\text{GS}}$ and its value equals the system's ground-state energy. A density ρ is called v-representable if and only if there is a potential $V(\mathbf{x})$ such that ρ is the ground-state density of the system of interacting electrons moving in $V(\mathbf{x})$. Mel Levy [77] showed that such a functional can be extended to the space of N-representable densities which are those densities that can be obtained from anti-symmetric wavefunctions of a fixed number of electrons. With this extension one could in principle minimize (2.26) if $T[\rho]$ and $F[\rho]$ were known. The former denotes the kinetic energy as a functional of density and the latter represents the interaction energy of the electrons. However, so far the latter is unknown and hence one has to rely on approximations to $F[\rho]$. In this work we choose the approximation developed by Perdew and Wang [78]. For an introduction and overview of further approximations see [79].

To find the minimum of the energy functional (2.26), we set its variation to zero

$$\delta E[\rho] = \int \left(\frac{\delta T[\rho]}{\delta \rho(\mathbf{x})} + V(\mathbf{x}) + \frac{\delta F[\rho]}{\delta \rho(\mathbf{x})} \right) \delta \rho(\mathbf{x}) d^3x \stackrel{!}{=} 0 \quad \forall \delta \rho(\mathbf{x}) \quad . \quad (2.27)$$

Kohn and Sham [80] argued that this expression is similar for a system of non-interacting particles moving in the effective potential $V_{\text{eff}}(\mathbf{x}) \equiv V(\mathbf{x}) + \frac{\delta F[\rho]}{\delta \rho(\mathbf{x})}$. Instead of

2. Theory of electron capture spectroscopy

solving (2.27) directly, one solves a one particle Schrödinger equation

$$\left(-\frac{\nabla^2}{2m} + V_{\text{eff}}(\mathbf{x}) \right) \phi_\tau(\mathbf{x}) = \epsilon_\tau \phi_\tau(\mathbf{x}), \quad (2.28)$$

which is called Kohn-Sham equation, and obtains the density as

$$\rho(\mathbf{x}) = \sum_\tau n_\tau |\phi_\tau(\mathbf{x})|^2 \quad \sum_\tau n_\tau = N \quad (2.29)$$

where the occupation numbers $n_\tau \in \{0, 1\}$ sum to the total number of electrons N . As V_{eff} depends on the density, this scheme has to be self-consistent, i.e. one starts with an estimated density, calculates V_{eff} for this density and solves (2.28) to obtain a new density. This procedure is repeated until some convergency criterion is reached. Possible criteria are to stop when the change in density (2.29) or ground-state energy (2.26) is below a given accuracy threshold. When this is reached, one does not only have a good estimate on ground-state energy and density, but has also obtained a set of Kohn-Sham orbitals $\{\phi_\tau\}$ which spans the one-particle Hilbert-space.

In a relativistic calculation the kinetic energy term in (2.28) is of course replaced by Dirac's Hamiltonian

$$H_{\text{KS}} \phi_\tau(\mathbf{x}) \equiv \left(-i\gamma^0 \gamma^k \partial_k + \gamma^0 m + V_{\text{eff}}(\mathbf{x}) \right) \phi_\tau(\mathbf{x}) = \epsilon_\tau \phi_\tau(\mathbf{x}) \quad . \quad (2.30)$$

If $V_{\text{eff}}(\mathbf{x})$ has spherical symmetry, the Kohn-Sham Hamiltonian H_{KS} commutes with total angular momentum operator $\mathbf{J} = \mathbf{L} + \mathbf{S}$ such that solutions of the Kohn-Sham equation (2.30) can be labeled by quantum numbers $\tau = (n, j, l, m)$. n denotes principal quantum-number, j total angular momentum, l orbital angular momentum and m is the projection of total angular momentum on the z-axis. The solutions are of the form [75]

$$\phi_\tau(\mathbf{x}) = \begin{pmatrix} G_\tau(r) \mathcal{Y}_{jl}^m \\ iF_\tau(r) \mathcal{Y}_{j\bar{l}}^m \end{pmatrix} \quad \text{where} \quad \mathcal{Y}_{jl}^m = \sum_{m_s=-1/2}^{1/2} \langle l, 1/2, m - m_s, m_s | j, m \rangle Y_l^{m-m_s} \xi_{m_s} \quad . \quad (2.31)$$

$G(r)$ and $F(r)$ are radial wave-functions. They are multiplied by eigenstates of \mathbf{J}^2 and J_z which are spin-weighted spherical harmonics \mathcal{Y}_{jl}^m where $\langle l, 1/2, m - m_s, m_s | j, m \rangle$ denote Clebsh-Gordan Coefficients, $Y_l^{m-m_s}$ normalized spherical harmonics and ξ_{m_s} are two-component spinors.

Dirac's Hamiltonian does not commute with the orbital angular momentum operator \mathbf{L} [75]. Instead it relates the angular momentum \bar{l} of the spinor's lower part to the upper part's l via $\bar{l} = l \pm 1$ iff $j = l \pm 1/2$. This allows us to label orbitals with l of the upper component, as the angular momentum of the lower component is then uniquely defined for a given j . Therefore, relativistic particles do not have definite orbital angular momentum, but in the non-relativistic limit the upper component of the Dirac-spinor dominates [75]. Hence, an interpretation of particles with definite l becomes possible for electrons bound in an atom. However, in section 2.4.4 we will see

that the mixing of different l within one spinor has drastic effects on electron capture probabilities.

For relativistic particles like the electron neutrino it is more natural to introduce the quantum-number $\kappa = -l - 1$ iff $j = l + 1/2$ and $\kappa = l$ iff $j = l - 1/2$. This quantum number is conserved under Dirac's Hamiltonian and one can infer both j and upper component's l of any state from it, since this information is encoded in its absolute value and sign [75]

$$j = \frac{2|\kappa| - 1}{2} \quad l = \begin{cases} j - 1/2 & \kappa < 0 \\ j + 1/2 & \kappa > 0 \end{cases} . \quad (2.32)$$

Thus, states are uniquely determined by specifying $\tau = (n, \kappa, m)$ and fields can be expanded according to (2.25) using the Kohn-Sham orbitals ϕ_τ (2.31).

In this work we are using the full-potential local-orbital minimum-basis code FPLO [81–83] to construct a basis of atomic Kohn-Sham orbitals. The many-body Hamiltonian is expressed in this basis as shown in the following sections.

2.4.2. Dirac Hamiltonian on a Kohn-Sham basis

The effective Hamiltonian (2.16) contains two operators H_D and V_C that are quadratic in the electronic fields

$$H_D + V_C = \int \psi_e^\dagger(\mathbf{x}) \mathcal{H}(\mathbf{x}) \psi_e(\mathbf{x}) d^3x \quad \text{where} \quad \mathcal{H}(\mathbf{x}) = -i\gamma^0 \gamma^k \partial_k + \gamma^0 m - \alpha \frac{Z}{|\mathbf{x}|} . \quad (2.33)$$

If the fields are expanded in atomic Kohn-Sham orbitals according to (2.25), we obtain

$$H_D + V_C = \sum_{\tau\tau'} \mathcal{H}_{\tau\tau'} e_\tau^\dagger e_{\tau'} \quad \text{where} \quad \mathcal{H}_{\tau\tau'} = \int \phi_\tau^\dagger(\mathbf{x}) \mathcal{H}(\mathbf{x}) \phi_{\tau'}(\mathbf{x}) d^3x . \quad (2.34)$$

In spherical coordinates, the angular integral in the above equation can be performed analytically, reducing the task of computing the Hamiltonian's matrix element to evaluating numerically [75]

$$\mathcal{H}_{\tau\tau'} = \delta_{\kappa\kappa'} \delta_{mm'} \int (g_\tau^*(r), f_\tau^*(r)) \begin{pmatrix} m - \alpha \frac{Z}{r} & (\frac{\kappa}{r} - \partial_r) \\ (\frac{\kappa}{r} + \partial_r) & -m - \alpha \frac{Z}{r} \end{pmatrix} \begin{pmatrix} g_{\tau'}(r) \\ f_{\tau'}(r) \end{pmatrix} dr . \quad (2.35)$$

We introduced Kronecker's $\delta_{\kappa\kappa'}$ as well as $g(r) = rG(r)$ and $f(r) = rF(r)$ which are zero at the origin allowing for a numerically stable implementation of the radial integral.

2.4.3. Mutual electronic interactions on a Kohn-Sham basis

The effective electro-magnetic interaction (2.14) can be expressed as

$$U_{\text{eff}} = \frac{1}{2} \int J^\mu(\mathbf{x}_1) \frac{1}{|\mathbf{x}_1 - \mathbf{x}_2|} J_\mu(\mathbf{x}_2) d^3x_1 d^3x_2 \equiv U_C + U_B \quad (2.36)$$

2. Theory of electron capture spectroscopy

where the four-current

$$J^\mu(\mathbf{x}) = \frac{e}{\sqrt{4\pi}} \psi_e^\dagger(\mathbf{x}) \gamma^0 \gamma^\mu \psi_e(\mathbf{x}) \quad (2.37)$$

has been introduced. The zeroth component $J^0 \sim e\rho(\mathbf{x})$ corresponds to charge density and the spatial components $J^k \sim ev^k$ resemble a charged current with velocity \mathbf{v} . Hence, the effective interaction splits into a density-density interaction U_C of order $e^2\rho^2$ and a current-current interaction U_B of order $e^2\mathbf{v}^2$ [84]. While the former resembles Coulomb interaction

$$U_C = \frac{1}{2} \int \psi_e^\dagger(\mathbf{x}_1) \psi_e(\mathbf{x}_1) \frac{\alpha}{|\mathbf{x}_1 - \mathbf{x}_2|} \psi_e^\dagger(\mathbf{x}_2) \psi_e(\mathbf{x}_2) d^3x_1 d^3x_2 \quad , \quad (2.38)$$

the latter is known to be the un-retarded part of Breit interaction [84]

$$U_B = \frac{1}{2} \int \psi_e^\dagger(\mathbf{x}_1) \alpha^k \psi_e(\mathbf{x}_1) \frac{\alpha}{|\mathbf{x}_1 - \mathbf{x}_2|} \psi_e^\dagger(\mathbf{x}_2) \alpha_k \psi_e(\mathbf{x}_2) d^3x_1 d^3x_2 \quad (2.39)$$

where $\alpha_\mu = \gamma^0 \gamma_\mu$. In a non-relativistic regime $(\mathbf{v}/c)^2 \ll 1$. Hence, the contribution from Coulomb interaction $U_C \gg U_B$ will dominate Breit interaction. From numerical calculations for Ho, we also see that the latter only shifts atomic excitation energies by ~ 0.5 eV which is an order of magnitude below the accuracy we can currently reach with the methods detailed in chapter 3. This confirms the assumption that Breit interaction is negligible for the moment and hence we will focus on Coulomb interaction in the remainder of this section.

As the Coulomb potential is singular at the origin, the above integral is best evaluated in a spherically symmetric basis. Hence, we follow the same route as in the previous section and expand the fields in atomic Kohn-Sham orbitals.

$$U_C = \frac{1}{2} \sum_{\tau'_1 \tau'_2 \tau_1 \tau_2} \mathcal{U}_{\tau'_1 \tau'_2 \tau_1 \tau_2} e_{\tau'_1}^\dagger e_{\tau'_2}^\dagger e_{\tau_2} e_{\tau_1} \quad (2.40)$$

$$\mathcal{U}_{\tau'_1 \tau'_2 \tau_1 \tau_2} = \int \phi_{\tau'_1}^\dagger(\mathbf{x}_1) \phi_{\tau_1}(\mathbf{x}_1) \frac{\alpha}{|\mathbf{x}_1 - \mathbf{x}_2|} \phi_{\tau'_2}^\dagger(\mathbf{x}_2) \phi_{\tau_2}(\mathbf{x}_2) d^3x_1 d^3x_2 \quad . \quad (2.41)$$

Here we removed the aforementioned un-physical self-interaction by bringing creation and annihilation operators into normal order. The two-particle matrix-elements $\mathcal{U}_{\tau'_1 \tau'_2 \tau_1 \tau_2}$ contain two radial and two angular integrals. The angular integrals can be calculated analytically with the help of Wigner-Eckart's theorem [85]

$$\begin{aligned} \mathcal{U}_{\tau'_1 \tau'_2 \tau_1 \tau_2} = & \sum_{K=0}^{\infty} \sum_{M=-K}^K (-1)^{M+j'_1+j'_2-m'_1-m'_2} \begin{pmatrix} j'_1 & K & j_1 \\ -m'_1 & -M & m_1 \end{pmatrix} \begin{pmatrix} j'_2 & K & j_2 \\ -m'_2 & M & m_2 \end{pmatrix} \\ & \times \langle \kappa'_1 || Y_K || \kappa_1 \rangle \langle \kappa'_2 || Y_K || \kappa_2 \rangle F_K(\tau'_1, \tau'_1, \tau_1, \tau_2) \quad . \end{aligned} \quad (2.42)$$

The expressions in large brackets denote Wigner-Three-J symbols [86] and $\langle \kappa'_1 || Y_K || \kappa_1 \rangle$ denotes a reduced matrix-element that only depends on κ'_1 , K and κ_1 . It vanishes if $l'_1 + l_1 + K$ is odd and otherwise yields [85]

$$\langle \kappa'_1 || Y_K || \kappa_1 \rangle = (-1)^{j'_1+1/2} \sqrt{(2j'_1+1)(2j_1+1)} \begin{pmatrix} j'_1 & j_1 & K \\ -1/2 & 1/2 & 0 \end{pmatrix} \quad . \quad (2.43)$$

The coefficient $F_K(\tau'_1, \tau'_1, \tau_1, \tau_2)$ is called relativistic Slater-integral and has the form [85]

$$F_K(\tau'_1, \tau'_1, \tau_1, \tau_2) = \int \frac{\min(r_1, r_2)^K}{\max(r_1, r_2)^{K+1}} \left(g_{\tau'_1}^*(r_1) g_{\tau_1}(r_1) + f_{\tau'_1}^*(r_1) f_{\tau_1}(r_1) \right) \quad (2.44)$$

$$\times \left(g_{\tau'_2}^*(r_2) g_{\tau_2}(r_2) + f_{\tau'_2}^*(r_2) f_{\tau_2}(r_2) \right) dr_1 dr_2 .$$

To evaluate these integrals numerically, two quadrature schemes have been implemented. The first uses midpoint-rule [88] which allows for fast evaluation of multiple integrals. The second scheme has been developed by Yanghui Qiu and Charlotte Froese Fischer [89]. It achieves much higher accuracy than the midpoint-rule.

2.4.4. Weak Hamiltonian

So far we constructed the Hamiltonian describing the mutual electronic interactions between relativistic electrons moving in a Coulomb potential determined by the nuclear charge of an atom. To describe the electron capture spectrum, the final missing ingredient is the part of the Hamiltonian that governs the electron capture process itself. In the case of ^{163}Ho the energy released during this decay is about $Q = 2.838$ keV [2]. Hence, to very good approximation we can use the effective, low-energy Hamiltonian for weak interactions (2.23) derived in section 2.2

$$H_W = \frac{G_W}{\sqrt{2}} \sum_{a=1}^3 U_{ae} \int \bar{\psi}_{\nu_a}(\mathbf{x}) \gamma^\mu (1 - \gamma^5) \psi_e(\mathbf{x}) \bar{\psi}_n(\mathbf{x}) \gamma_\mu (1 - \lambda \gamma^5) \psi_p(\mathbf{x}) d^3x + \text{h.c.} \quad (2.45)$$

Similar to the previous sections we expand the fields according to (2.25). However, while the electrons are expanded on bound atomic orbitals, the created neutrino is in an unbound state. Hence we employ an expansion of the neutrino's radial wavefunction on spherical Bessel functions

$$g_{q,\kappa,a}(r) = \mathcal{N}_a r j_l(qr) \quad (2.46)$$

$$f_{q,\kappa,a}(r) = \mathcal{N}_a \text{sign}(\kappa) \frac{q}{E_q + m_a} r j_{\bar{l}}(qr) \quad (2.47)$$

$$\mathcal{N}_a = \frac{\sqrt{2}q}{\sqrt{\pi \left[1 + \left(\frac{q}{E_q + m_a} \right)^2 \right]}} \quad E_q = \sqrt{q^2 + m_a^2} \quad (2.48)$$

$j_l(qr)$ denotes the l -th spherical Bessel function as function of neutrino absolute momentum q and distance from the origin r . E_q is the energy dispersion for a relativistic particle of mass m_a and the normalization \mathcal{N}_a is chosen such that

$$\int g_{q,\kappa,a}(r) g_{p,\kappa,a}(r) + f_{q,\kappa,a}(r) f_{p,\kappa,a}(r) dr = \delta(q - p) . \quad (2.49)$$

2. Theory of electron capture spectroscopy

Therefore, we can describe a single-particle neutrino mass-eigenstate by quantum numbers $\tau_\nu \equiv (q, \kappa_\nu, m_\nu, a)$, where the index a specifies the neutrino's mass-eigenstate. The sum over neutrino quantum numbers reads $\sum_{\tau_\nu} \equiv \sum_{a=1}^3 \sum_{\kappa_\nu, m_\nu} \int_0^\infty q^2 dq$. In this basis the Hamiltonian is

$$\mathcal{H}_W = \frac{G_W}{\sqrt{2}} \sum_{\tau_n \tau_p \tau_e} U_{ae} n_{\tau_n}^\dagger v_{\tau_\nu}^\dagger e_{\tau_e} p_{\tau_p} \int \phi_n^\dagger \gamma^0 \gamma^\mu (1 - \lambda \gamma^5) \phi_p \phi_\nu^\dagger \gamma^0 \gamma_\mu (1 - \gamma^5) \phi_e d^3x + \text{h.c.} \quad (2.50)$$

The creation operators $n_{\tau_n}^\dagger$ and $v_{\tau_\nu}^\dagger$ create a neutron and neutrino in a state with quantum numbers τ . The annihilation operators p_{τ_p} and e_{τ_e} annihilate a proton and electron respectively. Thus, the Fock-space on which these operators act can be divided into four disjoint sectors corresponding to the different particle species.

We want to span the sectors of the nucleons by a set of nuclear many-body states $|\psi_{\text{nuc}}^i, I_i, M_i\rangle$, where I_i denotes total nuclear angular momentum and M_i the corresponding projection on the z-axis. Therefore, we multiply the weak Hamiltonian by unity $\mathbb{1} = \mathbb{1}_{\text{lep}} \otimes \sum_{\text{nuc}} |\psi_{\text{nuc}}, I, M\rangle \langle \psi_{\text{nuc}}, I, M|$ from left and right. $\sum_{\text{nuc}} \equiv \sum_{\psi_{\text{nuc}}, I, M}$ abbreviates the sum over all quantum numbers characterizing the nuclear many-body state. Finally, we apply the Wigner-Eckhart theorem [154] to separate angular and radial dependencies, such that the Hamiltonian reads

$$\begin{aligned} \mathcal{H}_W &= \sum_{\tau_\nu, \tau_e} U_{ae} \sum_{\text{nuc}_i} \sum_{\text{nuc}_f} \sum_{JM} (-1)^{j_\nu - m_\nu + I_f - M_{I_f} + M} \\ &\times p_J^{I_i I_f}(\tau_\nu, \tau_e) \begin{pmatrix} I_f & J & I_i \\ -M_{I_f} & -M & M_{I_i} \end{pmatrix} \begin{pmatrix} j_\nu & J & j_e \\ -m_\nu & M & m_e \end{pmatrix} \\ &\times v_{\tau_\nu}^\dagger e_{\tau_e} \otimes |\psi_{\text{nuc}}^f, I_f, M_f\rangle \langle \psi_{\text{nuc}}^i, I_i, M_i| . \end{aligned} \quad (2.51)$$

The terms in brackets denote Wigner-3j symbols [86] and assure that total angular momentum is conserved in the electron capture process. A detailed derivation of this expression can be found in appendix A, where the precise form of the electron capture probability $p_J^{I_i I_f}(\tau_\nu, \tau_e)$ is also given. While its structure is quite complex in general, we can make some approximations for low energy processes as in the case of electron capture in Ho.

The ^{163}Ho nucleus has an average charge radius $r_{\text{nuc}} = 5.1907 \pm 0.0313$ fm [91]. Typical wavelengths of electrons bound in an atom are a few Ångström. Hence, relative capture probabilities, i.e. $p_J^{I_i I_f}(\tau_\nu, \tau_e) / p_J^{I_i I_f}(\tau_\nu, 1s_{1/2}) \equiv p_J(\tau_\nu, \tau_e)$, are rather insensitive to the actual nuclear wavefunction. Therefore, we approximate these as

$$\begin{aligned} p_J(\tau_\nu, \tau_e) &\approx \\ &\int_0^{r_{\text{nuc}}} (g_{\tau_\nu} g_{\tau_e} + f_{\tau_\nu} f_{\tau_e}) \langle \mathcal{Y}_{j_\nu l_\nu} || Y_J || \mathcal{Y}_{j_e l_e} \rangle - i (g_{\tau_\nu} f_{\tau_e} - f_{\tau_\nu} g_{\tau_e}) \langle \mathcal{Y}_{j_\nu l_\nu} || Y_J || \mathcal{Y}_{j_e \bar{l}_e} \rangle dr . \end{aligned} \quad (2.52)$$

The terms in brackets denote reduced matrix elements and are described in appendix A. When calculating the spectral function in the next section, we will make use of

this approximation. However, we can already infer which electrons are most likely captured. Since radial wavefunctions with s-orbital character have a larger amplitude within the nuclear charge radius as compared to other orbitals, the capture probabilities of the former will be most dominant. These include the large parts $g(r)$ of $s_{1/2}$ and the small parts $f(r)$ of $p_{1/2}$ orbitals. Here it becomes important to treat electrons fully relativistically and incorporate the mixture of different orbital angular momenta l in the components of a Dirac-spinor. In a classical or semi-relativistic frame-work, where the small part $f(r)$ is neglected, capture from p shells would be heavily suppressed as they have little overlap with the nucleus.

The orbital wave-functions of electrons with $j > \frac{1}{2}$ do not have components with s-orbital character and consequently a small relative capture-probability. This is the reason why in this work and in the work of others, described in section 1.3, electron capture is restricted to $s_{1/2}$ and $p_{1/2}$ orbitals only.

2.5. Spectral function

We derived the general form of the differential decay rate (2.7) in section 2.1 and obtained expressions of the Hamiltonian governing the full Ho system in a form suitable for numerical implementation in section 2.4. Now we are putting these pieces together and present the final form of the spectral function as used in this work.

To simplify notation we introduce the propagators

$$G^-(\omega) \equiv \langle \Psi_{\text{Ho}} | (H'_W)^\dagger \frac{1}{\omega + i0 - H} H'_W | \Psi_{\text{Ho}} \rangle \quad (2.53)$$

$$G^+(\omega) \equiv \langle \Psi_{\text{Ho}} | H'_W \frac{1}{\omega + i0 + H} (H'_W)^\dagger | \Psi_{\text{Ho}} \rangle \quad (2.54)$$

such that the differential decay rate reads

$$\frac{d\Gamma}{d\omega} \propto -\text{Im} \sum_{\tau_\nu} \delta(Q - w - E_\nu) (G^-(\omega) - G^+(\omega)) \quad (2.55)$$

where the sum $\sum_{\tau_\nu} \equiv \sum_{a=1}^3 \sum_{\kappa_\nu, m_\nu} \int_0^\infty q^2 dq$ runs over the neutrino's mass-eigenstate a , κ_ν , angular momentum in z-direction m_ν and absolute momentum q . The Hamiltonian $H \equiv H_D + V_C + U_C$ is given by Dirac's Hamiltonian (2.34) and the Coulomb operator (2.40). From the derivation in section 2.1 we infer that $H'_W = (\mathbb{1} \otimes |\tau_\nu\rangle\langle\tau_\nu|) H_W$ is given by a projection onto the subspace with a single neutrino with quantum numbers τ_ν applied to the weak interaction Hamiltonian (2.51).

H'_W acts on the Ho ground-state $|\Psi_{\text{Ho}}\rangle$ thereby creating an electronic hole in the inner shells and reducing the nuclear charge by one, as a proton is transformed into a neutron. Therefore, $|\Psi_{\text{Ho}}\rangle$ needs to describe 67 electrons, 67 protons and 96 neutrons. From rotational invariance of the Hamiltonian H_{eff} (2.16) we know that the total angular momentum F and its projection onto the z-Axis M_F of all these particles have to be conserved. If we assume that also the total angular momenta of the electrons

2. Theory of electron capture spectroscopy

J_e and of the nucleons I_i are conserved, we conclude that the full Ho ground-state can be expressed with the help of angular momentum coupling and Clebsch-Gordan coefficients $\langle J_e M_e, I_i M_i | F, M_F \rangle$

$$|\Psi_{\text{Ho}}\rangle \equiv |^{163}\text{Ho}, F, M_F\rangle = \sum_{M_e, M_i} \langle J_e M_e, I_i M_i | F, M_F \rangle |\psi_e, J_e, M_e\rangle \otimes |\psi_{\text{nuc}}^i I_i M_i\rangle . \quad (2.56)$$

$|\psi_e, J_e, M_e\rangle$ denotes the $2J_e + 1$ -fold degenerate, lowest energy-eigenstates of H including 67 electrons and $|\psi_{\text{nuc}}^i I_i M_i\rangle$ represents the degenerate, initial nuclear ground-states with 163 nucleons before the electron capture event has occurred.

To calculate the propagators $G^-(\omega)$ and $G^+(\omega)$, we multiply the groundstate with the weak Hamiltonian (2.51) and project onto the subspace that includes one neutrino with quantum numbers $\tau_\nu \equiv (q, \kappa_\nu, m_\nu, a)$

$$\begin{aligned} \mathcal{H}'_W |\Psi_{\text{Ho}}\rangle &= U_{ae} \sum_{\tau_e} \sum_{\psi_{\text{nuc}}^f} \sum_{JM} \sum_{M_e, M_i} (-1)^{j_\nu - m_\nu + I_f - M_{I_f} + M} \langle J_e M_e, I_i M_i | F, M_F \rangle \\ &\times p_J^{I_i I_f}(\tau_\nu, \tau_e) \begin{pmatrix} I_f & J & I_i \\ -M_{I_f} & -M & M_i \end{pmatrix} \begin{pmatrix} j_\nu & J & j_e \\ -m_\nu & M & m_e \end{pmatrix} \\ &\times e_{\tau_e} |\psi_e, J_e, M_e\rangle_{\text{elec}} \otimes |\psi_{\text{nuc}}^f, I_f, M_f\rangle \otimes |\tau_\nu\rangle_\nu . \end{aligned} \quad (2.57)$$

From this we obtain for the propagator

$$\begin{aligned} G^-(\omega) &= |U_{ae}|^2 \sum_{\psi_{\text{nuc}}^f} \sum_{\tau_e^1, \tau_e^2} \sum_{J_1 M_1} \sum_{J_2 M_2} \sum_{M_e^1, M_e^2} \sum_{M_i^1, M_i^2} (-1)^{M_1 + M_2} \\ &\times \left[p_{J_1}^{I_i I_f}(\tau_\nu, \tau_e^1) \right]^* \begin{pmatrix} I_f & J_1 & I_i \\ -M_{I_f} & -M_1 & M_i^1 \end{pmatrix} \begin{pmatrix} j_\nu & J_1 & j_e^1 \\ -m_\nu & M_1 & m_e^1 \end{pmatrix} \\ &\times p_{J_2}^{I_i I_f}(\tau_\nu, \tau_e^2) \begin{pmatrix} I_f & J_2 & I_i \\ -M_{I_f} & -M_2 & M_i^2 \end{pmatrix} \begin{pmatrix} j_\nu & J_2 & j_e^2 \\ -m_\nu & M_2 & m_e^2 \end{pmatrix} \\ &\times \langle J_e M_e^1, I_i M_i^1 | F, M_F \rangle \langle J_e M_e^2, I_i M_i^2 | F, M_F \rangle \\ &\times \langle \psi_e, J_e, M_e^1 | e_{\tau_e^1}^\dagger (\omega + i0 - H)^{-1} e_{\tau_e^2} | \psi_e, J_e, M_e^2 \rangle \end{aligned} \quad (2.58)$$

and a similar expression for $G^+(\omega)$. The Wigner-3j symbols and Clebsch Gordan coefficients can be calculated using the Racah formula [87]. Numerically challenging is the electronic Green's function

$$G_e^-(\omega) \equiv \langle \psi_e, J_e, M_e^1 | e_{\tau_e^1}^\dagger (\omega + i0 - H)^{-1} e_{\tau_e^2} | \psi_e, J_e, M_e^2 \rangle . \quad (2.59)$$

Here we have to first determine the Ho groundstate $|\psi_e, J_e, M_e\rangle$ including 67 electrons and then invert the Hamiltonian H on the space with 66 electrons, since one has been annihilated by electron capture. The corresponding numerical procedures are described in the next chapter.

Even more challenging is the calculation of the exact electron capture probabilities $p_{J_1}^{I_i I_f}(\tau_\nu, \tau_e^1)$, since this involves knowledge of nuclear wave-functions as outlined in section 2.4.4. There we already introduced relative capture probabilities $p_J(\tau_\nu, \tau_e)$ (2.52) in which one has approximately removed dependencies on the nuclear wave-function. Now we need to apply further simplifications to the propagator $G^-(\omega)$ (2.58) until we can replace the exact capture probabilities with the relative ones.

From our previous discussion in section 2.4.4 and (2.52) it is reasonable to consider electronic orbitals with s and $p_{1/2}$ character only, as these have largest overlap with the nucleus. The same reasoning applies to the created neutrinos such that we can restrict the sums in the propagator to include terms with $j_e = \frac{1}{2} = j_\nu$ (or equivalently $\kappa_e = \pm 1 = \kappa_\nu$) only. Hence, J_1 and J_2 can assume the values zero or one. Processes with angular momentum exchange larger than one are called "higher order forbidden" [93] and are much more unlikely than processes with $J \in \{0, 1\}$ because of the aforementioned argument about wavefunction-overlap with the nucleus.

Next we assume that only a single final nuclear state ψ_{nuc}^f – namely the nuclear ^{163}Dy ground-state – contributes to the propagator. This assumption is reasonable, since the energies of nuclear excitations typically exceed the Q-value of 2.8 keV by a few MeV. Thus $I_f = \frac{5}{2}$ and $I_i = \frac{7}{2}$ are fixed by the total nuclear spin of the ^{163}Dy and ^{163}Ho ground-states respectively. Due to conservation of angular momentum it holds that $J_1 \geq 1$ and equally for J_2 . Hence, we include terms with $J_1 = 1 = J_2$ only and neglect all others.

Furthermore, the maximal energy of the neutrino is restricted between zero and the Q-value. In this energy range the exact capture probability $p_{J_1}^{I_i I_f}(\tau_\nu, \tau_e)$ is approximately independent of the neutrino's energy. Because of this independence and the fact that we could set J_1, J_2, I_i, I_f and j_ν to fixed values, a replacement of the exact capture probability with the relative capture probability (2.52) alters the spectrum by a constant scaling factor only. This factor can be eliminated by normalizing the spectrum with respect to its integral.

Furthermore, we neglect the coupling between angular momenta of nucleus I_i and electrons J_e to total angular momentum F . Instead we evaluate $G_e^\pm(\omega)$ (2.59) for a fixed value of $M_e^1 = M_e^2$. Then the spectrum is independent of M_e and we choose $M_e = J_e$, as this is numerically most efficient due to the smaller number of Slater determinants as compared to states with lower $|M_e|$. However, we discuss angular momentum coupling between electrons and nucleus in section 4.3 as an outlook, where we will see that it introduces temperature dependence to the spectrum.

To summarize, the final form of the differential decay rate is given by

$$\frac{d\Gamma}{d\omega} \propto -\text{Im} \sum_{a=1}^3 |U_{ae}|^2 (Q - \omega) \sqrt{(Q - \omega)^2 - m_a^2} \sum_{\tau_e^1 \tau_e^2} p_1^*(\tau_e^1) p_1(\tau_e^2) (G_e^-(\omega) - G_e^+(\omega)) \quad (2.60)$$

where we omitted τ_ν in $p_1(\tau_e, \tau_\nu)$ to indicate the aforementioned approximate independence of the relative capture probabilities on neutrino quantum numbers for fixed

2. Theory of electron capture spectroscopy

$\kappa_\nu = \pm 1$. The normalization is chosen such that the integral over the full spectrum equals $\frac{1}{2}$, which implies that the dimension of the differential decay rate is "counts per half-life per atom per energy". This choice allows for an easy comparison to experimental data.

Note that (2.59) has poles at the eigenvalues of H . Thus the imaginary part of $G_e^-(\omega)$ contributes with a Dirac- δ peak for each pole to the electron capture spectrum. If we replace the infinitesimally small imaginary part by a finite line-broadening $\gamma/2$, the δ peaks turn into Lorentzians and can be computed numerically. In section 1.3 we discussed that other authors also used lorentzian line-shapes and up to chapter 4 we will follow this procedure. However, in chapter 5 we will show that this approximation has to be refined. Since H is unbounded from above, $G_e^-(\omega)$ does not have isolated poles only, but also involves branch cuts along the real axis. These will determine the actual line-shape.

Even without explicitly calculating the electronic propagator, we can already infer qualitatively what the endpoint region will look like. Therefore, we assume that the endpoint region is dominated by a single, lorentzian resonance, i.e. the M_1 (3s) resonance. Hence we can describe the spectrum (2.60) close to the endpoint approximately as

$$\left. \frac{d\Gamma}{d\omega} \right|_{\omega \approx Q} \propto \sum_{a=1}^3 |U_{ea}|^2 (Q - \omega) \sqrt{(Q - \omega)^2 - m_{\nu_a}^2} \frac{\gamma_{3s}}{(\omega - E_{3s})^2 + \gamma_{3s}^2/4} . \quad (2.61)$$

Figure 2.1 shows a plot of the spectral endpoint, where we divided by the phase-space factor of massless neutrinos to make the effect of three neutrino masses more apparent. For vanishing neutrino masses, this is almost constant over a small energy window. However, for non-vanishing masses, one obtains the sum of three spectra with endpoints at $\omega = Q - m_{\nu_a} c^2$ respectively. The relative strengths of these spectra are determined by $|U_{ae}|^2$. Therefore, we obtain three kinks with different heights according to the PMNS matrix elements $|U_{ae}|^2$.

In practice we need to calculate the full spectrum – not the endpoint region only – in order to assure that calculations are reliable and no feature is missing which may affect the end-point. Therefore, efficient numerical methods are necessary to calculate ground-state and resolvent of Hamiltonian H . This implies solution of the eigenvalue problem in a large Hilbert-space. In the next chapter we describe how this can be achieved by combining Lanczos' algorithm and configuration interaction.

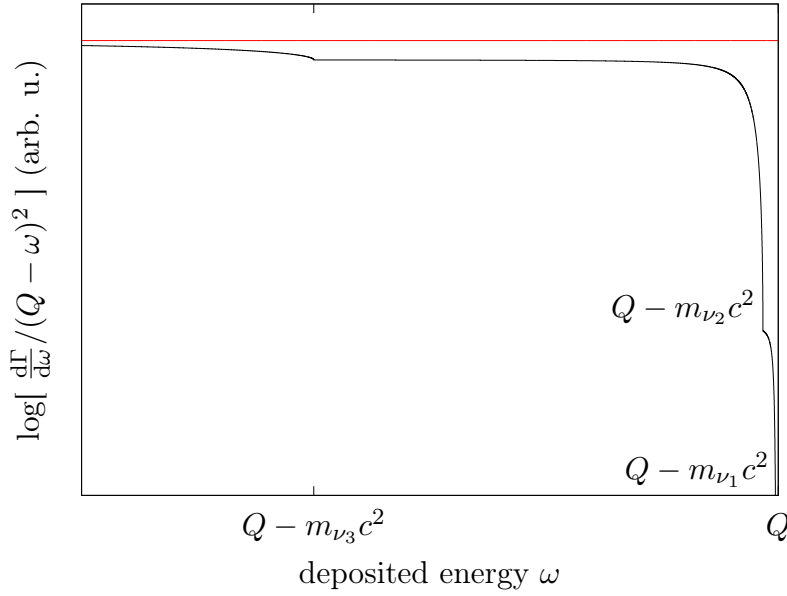


Figure 2.1.: Differential decay rate (2.61) divided by the phase-space factor of massless neutrinos. The spectrum is shown in its endpoint region for massive (black) and massless (red) neutrinos. The PMNS matrix elements and squared differences of the three neutrino masses have been taken from [92]. Normal mass hierarchy and $m_1 = 10^{-5} \text{ eV}/c^2$ have been assumed. The labels inside mark the kinks at $\omega = Q - m_{\nu_a}c^2$ above which not enough energy is available to create a neutrino in an eigen-state of mass m_{ν_a} .

3. Numerical Methods

The aim of this chapter is to describe numerical methods that allow for a solution of the eigenvalue-problem given by the Hamiltonian $H \equiv H_D + V_C + U_C$ and a fixed number of n_e electrons. This Hamiltonian consists of Dirac's Hamiltonian plus Coulomb's potential (2.34) and inter-electronic Coulomb repulsion U_C (2.40). The latter is the reason why an eigen-state cannot be expressed as a single Slater-determinant in general.

This leads to a major numerical problem in quantum many-body systems which is the size of the associated Hilbert-space. There are infinitely many one-particle states a single electron can occupy and infinitely many possible Slater-determinants that can be formed from combinations of these one-particle states. To reduce size, it is common practice to treat electrons as independent particles moving in an effective mean-field potential thereby reducing the many-body problem of n_e electrons to n_e identical single-particle problems in the form of a partial differential eigen-value problem. While this does not alter the size of the one-particle space which is still infinite, ground and excited states are now approximated by one Slater-determinant each. To solve the single-particle problem numerically – with a method as described in section 2.4.1 for instance – it is necessary to discretize the one-particle Hilbert-space by either choosing a finite set of functions serving as basis for a properly chosen, finite dimensional sub-space, or by using finite-elements methods. An overview of different techniques can be found in [101].

After such a discretization we are in a place with a finite set of N_{1P} one-particle states and a finite number of n_e electrons, where eigen-states are described by single Slater-determinants. We pointed out in section 1.3 that this is insufficient to calculate the electron capture spectrum with all its features. Electrons in an open shell can be aligned in different ways to form states with different total angular momentum J^2 . Coulomb repulsion between electrons conserves total angular momentum and splits the energies of these states which are linear combinations of Slater-determinants and are not unitarily equivalent to a single-determinant state in general. Consequently, this so called multiplet-splitting of energies cannot be found in a spectrum which is calculated with single-determinant states only. Furthermore, if there are multiple open shells – for instance due to holes in core orbitals – different configurations can hybridize to form states which are energetically favorable as compared to single-determinant states and are also a much better approximation to the true eigen-states.

Hence, we have to consider linear combinations of Slater-determinant states, which results in an effective Hilbert-space of dimension equal to the binomial coefficient of N_{1P} over n_e . In practice this can be very large, thereby challenging even modern computers as the following example shows.

3. Numerical Methods

In (2.59) we have seen that one needs to determine the many-electron groundstate of Ho and the resolvent of the Hamiltonian H in order to obtain the electron capture spectrum. Therefore, we restrict the one-particle basis to orbitals which are fully or partially occupied according to the Aufbau-principle. As the 4f shell is the Ho valence shell, we have $N_{1P} = 70$ one-particle states, which are populated by $n_{e,\text{Ho}} = 67$ indistinguishable electrons obeying Fermi-Dirac statistics. The resolvent is projected onto the subspace with $n_{e,\text{Dy}} = 66$ electrons. Hence, the dimensions of these two sub-spaces are

$$\binom{N_{1P}}{n_{e,\text{Ho}}} = 54\,740 \quad \text{and} \quad \binom{N_{1P}}{n_{e,\text{Dy}}} = 916\,895 \quad . \quad (3.1)$$

Thus, the resolvent in (2.59) is a matrix with $8 \cdot 10^{11}$ entries which require 6.4 TB of RAM when stored in double precision. This is far too large for practical purposes, even with the restriction on the fully and partially occupied orbitals. One could think of further reducing the Hilbert-space by only considering the partially occupied 4f orbitals, but the electron capture spectrum involves excitations with holes in the fully occupied orbitals and furthermore, configurations with holes in 4d orbitals contribute to the Ho groundstate due to Coulomb interaction. Hence, further restrictions on the one-particle basis are no option and methods have to be used that reduce computational cost. In section 3.1 we describe how the configuration interaction (CI) method handles the large number of states by ordering them in a hierarchy that can be systematically shortened or extended. Lanczos' algorithm that is employed for the solution of the still large eigen-value problem is detailed in section 3.2 and how we actually combine algorithm and CI in this work can be found in section 3.3.

3.1. Configuration interaction

The method of configuration interaction (CI) starts from a single Slater-determinant reference-state

$$|\Omega\rangle = \prod_{\tau \in \Omega} e_{\tau}^{\dagger} |0\rangle \quad (3.2)$$

that is described by a set Ω of one-particle quantum numbers and creation operators e_{τ}^{\dagger} acting on the vacuum $|0\rangle$. Typically this state is ground- or excited state of a Hartree-Fock or density functional theory approximation [103, 104] as pointed out in the beginning of this chapter. Additional Slater-determinants can be constructed from Ω by replacing the occupied quantum numbers with others that are not occupied in $|\Omega\rangle$. This yields new configurations which we label Ω_{τ}^{μ} if $\tau \in \Omega$ is replaced by $\mu \notin \Omega$, $\Omega_{\tau_1 \tau_2}^{\mu_1 \mu_2}$ if τ_1, τ_2 are replaced by μ_1, μ_2 respectively, and so on. Thus every state $|\psi\rangle$ can be expressed as linear combination of these configurations [104]

$$|\psi\rangle = C|\Omega\rangle + \sum_{\tau \mu} C_{\tau}^{\mu} |\Omega_{\tau}^{\mu}\rangle + \sum_{\tau_1 \mu_1 \tau_2 \mu_2} C_{\tau_1 \tau_2}^{\mu_1 \mu_2} |\Omega_{\tau_1 \tau_2}^{\mu_1 \mu_2}\rangle + \dots + \sum_{\tau_1 \dots \tau_{n_e}, \mu_1 \dots \mu_{n_e}} C_{\tau_1 \dots \tau_{n_e}}^{\mu_1 \dots \mu_{n_e}} |\Omega_{\tau_1 \dots \tau_{n_e}}^{\mu_1 \dots \mu_{n_e}}\rangle \quad (3.3)$$

This enables us to define a hierarchy of states according to the amount of changed quantum numbers [104]. The zeroth order is the reference state itself, at first order are all states with a single hole in the occupied orbitals of the reference state, on second order all states with two holes and so on.

While expansion (3.3) of an eigen-state is exact on the Hilbert-space of n_e electrons and N_{1P} single-particle orbitals, any truncation at some order of the CI hierarchy introduces an error, but still obeys the variational principle in the sense that the lowest, approximate eigen-value is an upper bound on the true ground-state energy [102]. This bound can be improved by going to higher orders in CI hierarchy. Hence, already at first order – which is called CIS where "S" stands for single hole – one obtains improvements as compared to mean-field theory. In the introduction 1.3 we noted that two-hole states are important for the electron capture spectrum, hence at least we need to include both single- and double-hole configurations which is referred to as CISD in literature.

When choosing any truncation – any order of the CI hierarchy – there is always a contest between reducing computational cost and increasing accuracy. While the former prefers truncation at lower orders, the latter needs inclusion of higher orders. However, having fixed the accuracy goal, one can reduce computational cost by further means – other than going to lower orders – which do not affect accuracy. It is possible to optimize the single-particle basis in such a way that the Hamiltonian decouples odd and even orders. Then one can use states of even order only, which in case of double-hole states is called CID. Furthermore, symmetries can be utilized to include only states that belong to a certain irreducible representation (irrep) of the corresponding symmetry-group. This can be achieved by application of projection operators, which project states not belonging to the irrep onto zero and keep the others [102].

Instead of choosing a single reference state, one can choose multiple from which the CI hierarchy is constructed. This method is called multi-reference configuration interaction (MRCI). In this work we are doing something similar, because multiple references allow for a reduction of numerical uncertainties due to number-losses as is pointed out in the next section. There we describe an efficient eigen-problem solver that is used often in CI calculations [102], since the reduced Hilbert-space is still large even after application of all the mentioned methods.

3.2. Lanczos' algorithm

From the previous discussion in this chapter it became apparent that the large size of the many-body Hilbert-space leads to high computational costs when solving the eigenvalue problem for a given Hamiltonian. Storage in RAM of matrix elements may not be possible and computing a large number of eigenvalues is time-consuming. However, Lanczos' algorithm [105] allows us to calculate the Ho groundstate and the propagator (2.59) by neither storing all matrix elements of the Hamiltonian, nor exploring the full Hilbert-space to find every eigenvalue.

to non-zero singular values and V_0 contains the right singular vectors corresponding to the vanishing singular values. Define

$$\psi_i \equiv \tilde{\psi}_i V_\Sigma \Sigma^{-\frac{1}{2}} V_\Sigma^\dagger \Rightarrow \psi_i^\dagger \psi_i = V_\Sigma V_\Sigma^\dagger . \quad (3.8)$$

If $r = n_b$, i. e. all singular values are non-zero, V_Σ is unitary and hence the vectors contained in ψ_i are orthonormal. In this case we can show that the off-diagonal blocks of T are hermitian

$$B_i = \psi_i^\dagger A \psi_{i-1} \stackrel{(3.5)}{=} \psi_i^\dagger \left(\tilde{\psi}_i + \psi_{i-1} A_{i-1} + \psi_{i-2} B_{i-1}^\dagger \right) = \psi_i^\dagger \tilde{\psi}_i = V_\Sigma \Sigma^{\frac{1}{2}} V_\Sigma^\dagger . \quad (3.9)$$

Hermiticity directly follows from $\Sigma^\dagger = \Sigma$. If however the $\tilde{\psi}_i$ are not linearly independent, one has to remove some vectors until linear independence is restored before continuing with the next iteration step. In this case V_Σ is an $n_b \times r$ matrix containing orthonormal vectors and $V_\Sigma V_\Sigma^\dagger$ thus is the projection onto the sub-space spanned by the columns of V_Σ . We remove the $n_b - r$ vectors of ψ_i that have the smallest norm. These are then orthonormalized with the same procedure until one arrives at a set of linearly independent Krylov vectors.

If in some step $i = N$ all singular values are zero, one has found a sub-space which is invariant under A and spanned by $\Psi = \cup_{i=0}^{N-1} \psi_i$. In this case the eigenvalues of T are exact eigenvalues of A and so are the eigenvectors. However, in practice the dimension of \mathcal{H} is too large to fully explore an invariant sub-space. Hence, the iteration is aborted after n_k steps. Then eigenvalues and eigenvectors of T are approximations to the eigenvalues and eigenvectors of A . Furthermore, the n -th eigenvalue of T is an upper bound for the n -th eigenvalue of A , since the approximate eigenstates obey the variational principle [111].

These approximations are especially good for eigenvalues a_j with large magnitude and their corresponding eigenvectors ϕ_j , since in every iteration we apply A to the previously constructed states. After n_k iterations the newly created states have contributions of $\sim a_j^{n_k} \phi_j$ thereby implying the larger the magnitude of an eigenvalue, the larger the contribution of the corresponding eigenvector.

However, we are interested in finding the ground-state of the Hamiltonian and therefore apply Lanczos' algorithm multiple times. To find the n_b lowest eigenstates one picks n_b linearly independent starting vectors and constructs a Krylov basis according to the procedure described above. The iteration stops after n_k steps, where n_k should be chosen to be not too large in order to avoid numerical loss of orthogonality of the Krylov vectors [111]. In this basis one determines the n_b lowest eigenvalues of T together with their eigenvectors and uses the latter as new starting vectors for a further application of Lanczos' routine. This is repeated until some convergency criterion is fulfilled. Then the n_b lowest eigenvalues and corresponding eigenvectors from the last iteration can be used to approximate the true eigenvalues and eigenvectors of the Hamiltonian. As convergency criterion we choose the variances of the Hamiltonian with respect to the approximate eigenvectors to be below a given accuracy threshold. This reflects that the variance vanishes if, and only if calculated with respect to a true eigenvector.

3. Numerical Methods

With this procedure we obtain a good approximation to the Ho ground-state. To calculate the spectral function (2.59), we need to evaluate the resolvent projected on the sub-space spanned by $\{e_\tau|\psi_e\rangle \mid \tau \in \Omega_{\text{EC}}\}$ only, where $\Omega_{\text{EC}} = \{1s, \dots, 6s, 2p_{1/2}, \dots, 5p_{1/2}\}$. Therefore, we pick these states as starting vectors for Lanczos' algorithm and calculate

$$G_e^-(\omega) \approx \left[(\omega + i0 - T)^{-1} \right]_{00} \quad (3.10)$$

where the subscript reminds us that the electronic Green's function (2.59) is by construction encoded in the first block on the diagonal of the resolvent. The rows and columns of this block are labeled by τ_e^1 and τ_e^2 in (2.59), but we dropped these indices here for the sake of cleaner notation. Since T is block-tri-diagonal, the above expression can be evaluated by a continued fraction [111]. However, a spectral decomposition of T leads to a much more efficient numerical implementation than using continued fractions. As T is block-tri-diagonal, the decomposition is fast.

To judge the accuracy of approximation (3.10), we can look at the moments of the spectral function

$$-\frac{1}{\pi} \int_{-\infty}^{\infty} \text{Im} [G_e^-(\omega)] \omega^m d\omega = \int_{-\infty}^{\infty} \langle \psi_e | e_{\tau_e^1}^\dagger \delta(\omega - H) e_{\tau_e^2} | \psi_e \rangle \omega^m d\omega = \langle \psi_e | e_{\tau_e^1}^\dagger H^m e_{\tau_e^2} | \psi_e \rangle \quad (3.11)$$

If $m = 2n + 1$ this is the projection of H on $\text{span}(\{H^n e_\tau | \psi_e\rangle \mid \tau \in \Omega_{\text{EC}}\})$. Thus, if $m \leq 2n_k + 1$, this projection of H is fully determined by T and

$$-\frac{1}{\pi} \int_{-\infty}^{\infty} \text{Im} [G_e^-(\omega)] \omega^m d\omega = [T^m]_{00} \quad . \quad (3.12)$$

Consequently, after n_k iteration steps, the first $2n_k + 1$ moments of the spectral function are exact [111]. This property is not present in approaches using Fermi's golden rule as described in section 1.3.

A further advantage of the above choice of starting vectors and using the block-variant of Lanczos' routine is a separation of energy scales. Each starting vector has a hole in a different core orbital. These states have average energies which are the diagonal entries of the first block T_{00} and range from 60 keV for the 1s hole down to a few eV for the 6s hole. If on the other hand one would use a single starting vector, the first entry of the tri-diagonal matrix would be an average over these energies and hence numerical accuracy would be reduced due to number-loss. The same reasoning applies for further diagonal blocks/entries. Hence, the block-variant separates energy scales and reduces number-loss as compared to the standard, non-block-variant.

3.3. Lanczos and CI

If a CI reference state is chosen as starting vector of Lanczos' algorithm and the Hamiltonian acts on it to create the next Krylov vector, the latter becomes a linear combination of states with single and double holes with respect to the reference state.

While Dirac's Hamiltonian creates single holes, Coulomb interaction is responsible for double holes. However, this also implies that not every single or double hole configuration is included. Only those are present in the first step, which can be reached from the starting configuration by one- and two-body scattering processes encoded in the Hamiltonian. These processes respect all symmetries of the Hamiltonian, which becomes important in a moment. In the next iteration step further single and double hole configurations are added, but also three and four hole states. If the iteration was continued until the Krylov basis either spans the whole Hilbert-space or an invariant sub-space, all configurations are included and the eigen-states are given by the CI expansion (3.3).

If the Hamiltonian is invariant under certain symmetries, only those terms in the expansion have non-vanishing coefficients if they belong to the same irreducible representation of the symmetry-group as the reference state. One great advantage of Lanczos' algorithm is that all terms with vanishing coefficient should not appear in the calculation as long as the starting vector belongs to the same irreducible representation as the desired eigen-vectors. As pointed out in section 3.1, application of projection operators to a mean-field single-determinant state achieves this condition and consequently reduces the number of configurations included in the calculation [102]. However, in practice these configurations, that should vanish, can obtain small but non-zero coefficients due to numerical instabilities. Hence, modifications of the algorithm would be necessary to avoid this.

For many systems – as in the case of the Ho electron capture spectrum – even an invariant sub-space is too large to be spanned completely by a Krylov basis. Similarly the full CI expansion (3.3) isn't feasible either. If it is truncated at a certain order, it may be possible to use Lanczos' algorithm to explore the full sub-space spanned by all configurations up to this order. The results will be different from directly applying the algorithm without restriction to a certain CI order and then stopping the iteration after a fixed number of steps n_k before the whole space is explored. The latter case involves terms of higher CI order as compared to the former case, if n_k is large enough. On the other hand, the latter case does not necessarily include all terms of a given CI order. Hence, both approaches have many similarities, but may differ in their final results.

Often there are configurations with small coefficients and hence small impact on the approximated eigenvalues. The Lanczos' routine, as implemented in Quanta [109] and used in this work, directly removes such configurations from the calculation as soon as they are encountered in an iteration step and have a coefficient smaller than a predetermined threshold. This reduces computational cost with only small accuracy losses and is another difference as compared to usual CI calculations. However, terms with small coefficients can have an impact on the approximated eigenvalues if there are many of them. Hence, it is necessary to verify that the removed terms do not alter the eigenvalues within the desired accuracy. Therefore, one monitors how eigenvalues change when lowering the threshold.

To summarize, in this work we are using a Block-Lanczos' routine where multiple starting vectors are chosen. This is comparable to a multi reference configuration

3. Numerical Methods

interaction calculation, but with the differences that the starting vectors may differ from the mean-field states, configurations with small coefficients are neglected and not every configuration belonging to the iteratively included CI orders may appear during construction of the Krylov basis.

4. Bound state resonances in the electron capture spectrum

Within the framework described in the previous chapters, we are now in a position to do an ab initio calculation of the calorimetric electron capture spectrum of ^{163}Ho . Section 4.1 reviews results and computational details of publication [1]. We describe how to apply the methods from chapter 2 and 3 to calculate the electron capture spectrum. Our calculation is compared to experimental data and spectral features are explained on the level of atomic relaxation involving bound states. In section 4.2 we describe how to determine the Q-value using calculations from 4.1 together with experimental data and summarize the results of publication [2].

4.1. How to calculate the electron capture spectrum

We derived the form of the electron capture spectrum in (2.60), where we have to evaluate $G_e^\pm(\omega)$ from (2.59). Therefore, we start a DFT calculation using FPLO as described in section 2.4.1 to obtain the Kohn-Sham orbitals for a Ho atom. These are used in Quanta [109] to construct the Hamiltonian $H = H_D + V_C + U_C$ which is given by Dirac's Hamiltonian (2.34) and Coulomb interaction (2.40). The nuclear potential V_C is constructed for $Z = 66$ (Dy) to calculate the resolvent in $G_e^\pm(\omega)$ and for $Z = 67$ (Ho) to determine the Ho ground-state. To achieve the latter, we define a set of random starting vectors that belong to the configuration $[\text{Xe}]6s^24f^{11}$ and apply the Block-Lanczos' algorithm described in section 3.2.

Since the Hamiltonian commutes with the total angular momentum operator \mathbf{J}_e , the ground-state has a definite $J_e = \frac{15}{2}$. Total orbital angular momentum \mathbf{L}^2 and total spin \mathbf{S}^2 are not conserved quantum numbers due to spin-orbit coupling. Hence, an L-S coupling scheme is not applicable. Furthermore, the ground-state does not only involve the $[\text{Xe}]6s^24f^{11}$ configuration. Instead it also contains small contributions from configurations with holes in core orbitals and additional electrons in the 4f valence shell. These influence the relative intensities between different resonances in the spectrum.

With the Ho ground-state $|\psi_e\rangle$ at hand, we apply the electron annihilation operator to obtain a new set of starting vectors $\{e_\tau|\psi_e\rangle \mid \tau \in \Omega_{\text{EC}}\}$, where $\Omega_{\text{EC}} = \{1s, \dots, 6s, 2p_{1/2}, \dots, 5p_{1/2}\}$ denotes the orbitals from which electrons can be most likely captured by the nucleus. The starting vectors can be understood as possible states of the system at that very instant when an electron has been captured. They are used in the Block-Lanczos' routine to calculate the spectral function $G_e^\pm(\omega)$ (2.59)

4. Bound state resonances in the electron capture spectrum

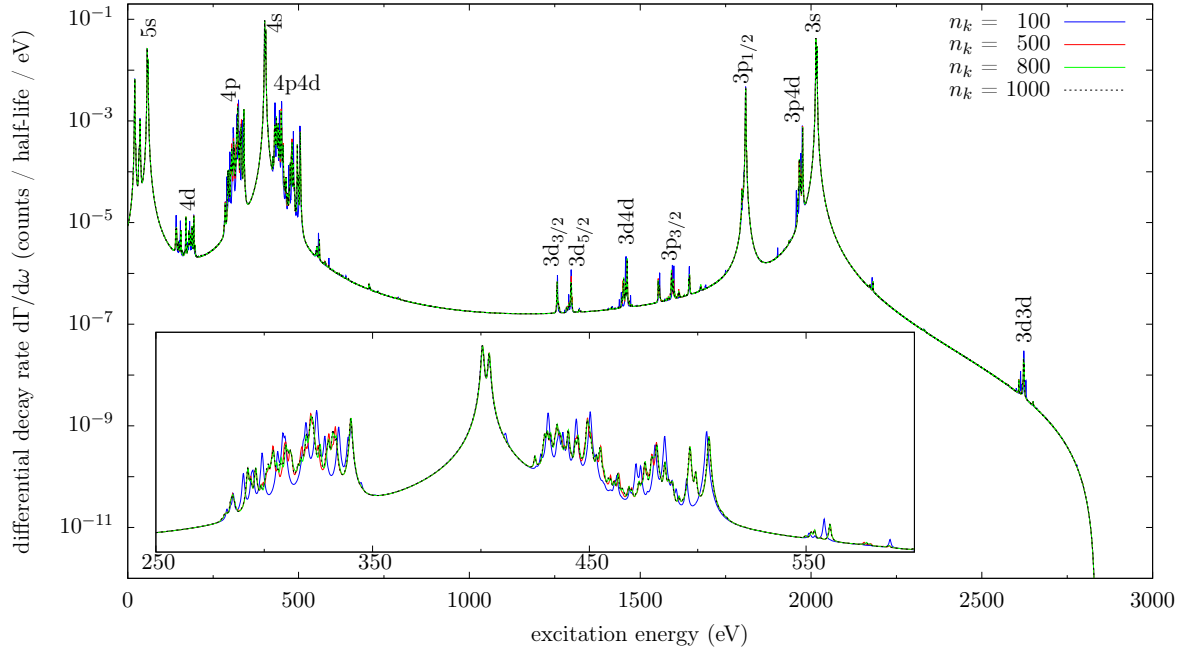


Figure 4.1.: Calculated electron capture spectrum (2.60) involving bound electronic orbitals only. Resonances emerge from excitations of the Dy daughter atom where holes have been created in the inner shells (labels). To test convergence of Lanczos' algorithm the number of iteration steps n_k has been successively increased. Multiplets and satellite structures are most sensitive to the size of the Krylov basis as can be seen in the inset. To resolve these small features, we calculated the spectrum with an overall lorentzian broadening of 1 eV.

where the Hamiltonian H contains the nuclear potential of the Dy daughter atom with $Z = 66$. We run the Block-Lanczos algorithm separately for captured electrons with $j_z = -\frac{1}{2}$ and $j_z = +\frac{1}{2}$, which is possible since the corresponding starting vectors have different total angular momentum J_z and are hence in different subspaces that are invariant under action of the Hamiltonian. Convergency is tested by increasing the maximum number of Krylov-states step-wise until the spectral shape does no longer change.

This results in the spectrum shown in figure 4.1. It includes multiple excitations due to different relaxation mechanisms. The major resonances correspond to direct excitation by electron capture from the s and $p_{1/2}$ orbitals. In subsequent relaxation processes, electrons can fill these orbitals and leave holes in d and $p_{3/2}$ shells, or can additionally scatter a further electron to the valence shell. Such processes create excited states with valence configuration $4f^{12}$ and two holes in the inner shells as labeled in figure 4.1.

Since the above processes are all encoded in the Hamiltonian H , Lanczos' algo-

4.1. How to calculate the electron capture spectrum

rithm automatically introduces the configurations emerging from relaxation in the calculation. This happens when building the Krylov basis by acting with the Hamiltonian on the Krylov vectors from the previous iteration step. Thereby each configuration is mapped onto the superposition of all possible configurations that are reachable from this one by either scattering a single electron from its orbital into a previously unoccupied orbital, or by scattering two electrons due to Coulomb interaction from their orbitals into two previously unoccupied orbitals. The coefficients of the so created configurations in the new Krylov vector depend on the matrix elements of the Hamiltonian. In this way Lanczos' algorithm selectively introduces the most dominant configurations to the calculation. The resulting approximate eigenstates are multi-configuration, Multi-Slater-determinant states, which are truly not representable by a single Slater-determinant.

While the number of determinants (22) is relatively modest for the Ho ground-state, the excited states of the Dy daughter involve up to 10^4 determinants. However, if compared to the dimension of the Hilbert-space (9×10^5), estimated in the beginning of chapter 3, this is still smaller. Therefore, Lanczos' algorithm is so efficient in this application due to the automatic, selective inclusion of dominant determinants.

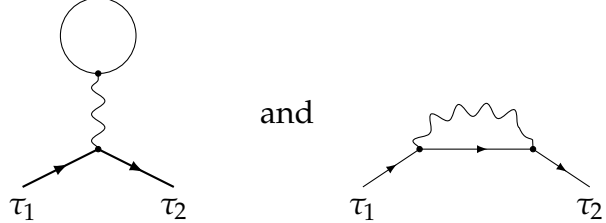
In order to monitor convergence of Lanczos' algorithm, we plotted the spectrum for multiple values of the number of iteration steps n_k in figure 4.1. In every spectrum $n_b \cdot n_k$ Krylov-vectors contribute, where $n_b = 20$ is the number of starting vectors. This determines the accuracy of the resolvent. From the inset we infer that satellite structures and multiplets require a much larger Krylov basis than major resonances in order to be converged. While the M_1 (4s) resonance does not change visibly when increasing n_k from 100 to 500, the satellites do change until we reach $n_k = 800$. Then the spectrum involves $1.6 \cdot 10^4$ Krylov vectors, but much less resonances below the Q-value. Here enters the problem that large eigenvalues of the Hamiltonian converge more quickly than small ones as mentioned before, which explains the need for many iteration steps to get an accurate spectrum in the range $[0, Q]$.

Now we want to identify the different resonances and the relaxation processes that create them. In a first step we analyze the first block T_{00} of the tri-diagonal representation (3.4) of the Hamiltonian. This block contains the matrix elements of states with a single core hole created by electron capture from the Ho ground-state. If we calculate the spectrum from this block only, we obtain the major resonances ns and $np_{1/2}$ in figure 4.1. From these matrix elements we can deduce that there is mixing between the different orbitals in which holes have been created, as the first block itself has non-vanishing off-diagonal entries. This reflects that the Ho one-particle orbitals, from which an electron has been captured, now hybridize in the presence of the Dy nucleus. This is the reason we also included the K and L shell (1s, 2s, 2p) in the calculation although electron capture from those orbitals is energetically above the Q-value. However, these shells are important in terms of completeness of the single-particle basis and the mentioned hybridization effects.

Since in the first block only configurations with a single core hole in the ns and $np_{1/2}$ are involved, only relaxation processes where a single particle is scattered contribute. This involves scattering off the nuclear potential or off the remaining elec-

4. Bound state resonances in the electron capture spectrum

trons without changing their quantum numbers. To put it differently, from the Hamiltonian $H = H_D + V_C + U_C$ only H_D and V_C have non-zero matrix elements in that block, as well as the Hartree- and Fock-terms contained in U_C . We denote these terms, or the corresponding relaxation processes, by



(4.1)

This shows that we can also understand the calculation of the EC spectrum with Lanczos' algorithm as a diagrammatic expansion. Hence, the step-wise construction of a Krylov basis and a block-tri-diagonal representation of the Hamiltonian is connected to more intuitive Feynman diagrams. The latter can in turn be interpreted as relaxation processes, where the quantum numbers τ_1 label the involved single-particle orbital from which an electron is scattered into orbital τ_2 . Such a connection can be best understood when explicitly writing the Krylov vectors as expansion in Slater-determinants for given configurations, i.e. sets of quantum numbers Ω that define occupied orbitals

$$|\psi_i^k\rangle = \sum_{\Omega} \alpha_i^k(\Omega) \left(\prod_{\tau \in \Omega} e_{\tau}^{\dagger} \right) |0\rangle \equiv \sum_{\Omega} \alpha_i^k(\Omega) |\Omega\rangle . \quad (4.2)$$

The block elements of the tri-diagonal representation $A_i^{k,q} = \langle \psi_i^k | H | \psi_i^q \rangle$ and $B_i^{k,q} = \langle \psi_i^k | H | \psi_{i-1}^q \rangle$ contain terms of the form

$$\langle \Omega_1 | U_C | \Omega_2 \rangle = \langle 0 | \left(\prod_{\tau \in \Omega_1} e_{\tau} \right) U_C \left(\prod_{\tau \in \Omega_2} e_{\tau}^{\dagger} \right) |0\rangle \quad U_C = \sum_{\tau_1 \tau_2 \tau_3 \tau_4} U_{\tau_1 \tau_2 \tau_3 \tau_4} e_{\tau_1}^{\dagger} e_{\tau_2}^{\dagger} e_{\tau_4} e_{\tau_3} \quad (4.3)$$

which can be calculated using Feynman rules. Since in the n -th iteration step the Krylov vector is $\psi_n \sim H^n \psi_0$, the order of included diagrams is increased in every step. In this way, the algorithm directly includes the interactions between different configurations due to electronic Coulomb repulsion and goes beyond the single-slater-determinant approximation to a configuration-interaction calculation.

Already in the second diagonal block T_{11} configurations with two holes in inner shells are involved. In a diagrammatic language this means inclusion of scattering

4.1. How to calculate the electron capture spectrum

diagrams with four external lines [1]

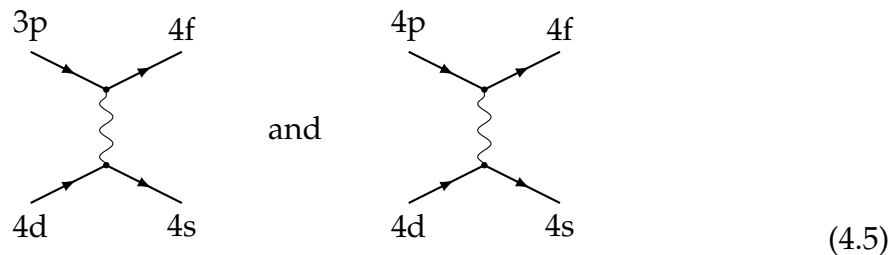


These lead to the creation of holes in previously closed shells. Either a state with a single core hole or a state with two core holes can emerge.

In the first case an electron from a closed shell fills a hole created by electron capture. Thereby it scatters with the 4f valence electrons and can transfer angular momentum. This way resonances of figure 4.1 with holes in d and $p_{3/2}$ orbitals appear.

In the second case the electron that fills the core hole transfers its energy to another core electron which is scattered into the valence shell, leading to configurations with two core holes and twelve electrons in 4f. We identify such states by restarting the calculation and imposing restrictions on the allowed configurations. If we want to see which resonances are dominated by single-hole states, we restrict the 4f orbital to have eleven electrons and observe which peaks disappear and which remain. The latter are the ones with single core holes. To identify in which shells the holes are created, we restrict the orbitals, we want to test, to be completely filled and again see which peaks disappear. For two-hole states we can do the same analogously. Thereby we observe that three-hole states, which emerge from higher powers of H in the Krylov basis, have a negligible contribution. Nonetheless, these higher powers are needed for accurate peak intensities and positions.

Especially dominant are the 3p4d and 4p4d resonances in figure 4.1. They emerge from Coster-Kronig and super Coster-Kronig transitions respectively,



which explains their high intensities compared to other resonances that are also created by secondary processes subsequent to electron capture. Since the principal quantum numbers of the electrons involved in the corresponding scatterings are (almost) all the same, cross-sections of these processes are large, leading to high intensities of the resonances.

Here, the advantage of Kubo's formula against Fermi's golden rule described in section 2.1 becomes apparent. If Kubo's response functions $G^\pm(\omega)$ are evaluated with Lanczos' algorithm, the dominant multi-determinant states and configurations

4. Bound state resonances in the electron capture spectrum

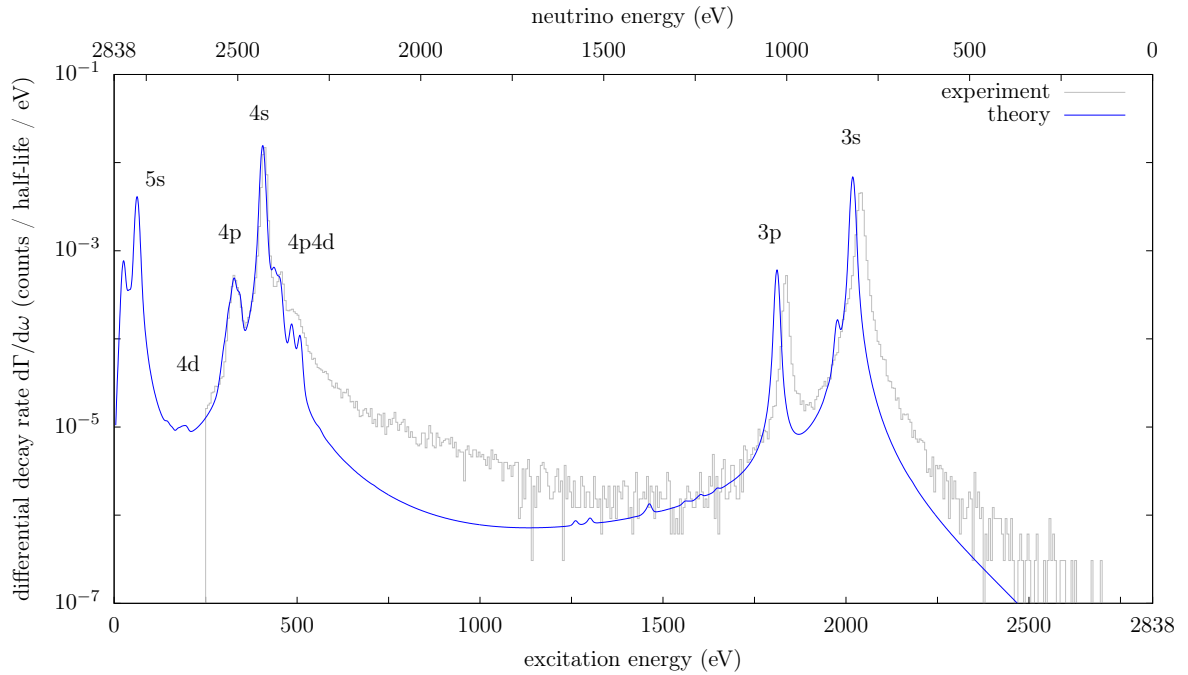


Figure 4.2.: Theoretical data [1] are the same as in figure 4.1, but with an overall lorentzian broadening of 5 eV convoluted with a Gaussian to account for detector broadening. Experimental data are taken from [2]. Comparison shows that lorentzian broadening is insufficient to describe the region between 4s and 3s resonances.

enter the calculation automatically. Using Fermi's golden rule, as done by other authors described in section 1.3, involves an infinite sum over final states leading to the problem that it might not be clear a priori which states, Slater-determinants, or configurations are dominant and have to be included in the sum. Therefore, in works of these other authors the 4s satellite structure has so far been unexplained, as the corresponding two-hole states have either been neglected, or treated as single Slater-determinants. In both cases it is impossible to obtain the observed multiplet structure of the satellites.

It is even worse if resonances are hidden due to too low experimental resolution as it is the case for the 3p4d edge or the 4p multiplets in figure 4.1. If existence of a resonance is not known a priori, it is unlikely that it will be included in the sum in Fermi's golden rule. Thus, to fully understand the shape of the electron capture spectrum and all its features, an ab-initio approach as presented in this work is important.

The results of this approach are compared to experimental data in figure 4.2. The spectrum is calculated as described in this chapter and convoluted with a Gaussian of 10 eV full width at half maximum (FWHM) to account for detector broadening. Our calculations reproduce the intensities of resonances and the 4p4d satellite structure quite well.

Although an overall constant lorentzian broadening of 5 eV has been assumed, we obtain different apparent broadenings due to multiplet splitting. This is most prominent when comparing the M_2 ($3p_{1/2}$) and the N_2 ($4p_{1/2}$) edge. The latter resonance is much broader due to an accidental degeneracy with shake-up states. Such broadenings indirectly affect the spectral shape in the wings of the resonances. If multiplets are unresolved, due to low experimental resolution, a fit to data will overestimate the natural line-broadening. This would affect the spectral shape close to the resonance only marginally, but would lead to an increased error in the resonance's wings. Hence, a careful study of the M_1 line-broadening is necessary for high sensitivities on neutrino masses, which is done as part of chapter 5. Furthermore, calculations predict a small peak at the left side of M_1 ($3s$) which is currently hidden in experimental data with the given resolution.

The most prominent discrepancies between theory and experiment are observed in the positions of the resonances and in the region between the N_1 ($4s$) and M_2 ($3p$) edges. There the lorentzian line-broadening is insufficient to describe the asymmetric high energy wing of the N_1 ($4s$) edge and satellites. Since calculations have been restricted to bound states only, it is not surprising that such continuous spectral features cannot be reproduced. Processes that couple bound states to the continuous energy spectrum of the Hamiltonian are necessary to account for such extended high energy wings. Inclusion of these processes will allow for a treatment of line-broadening from first principles. The Auger-Meitner effect, fluorescence decay and interaction with the chemical environment of Ho are probably the most important processes of this kind. The former will be studied in chapter 5 where we show that, besides being responsible for most of the spectral broadening and the extended high energy wings, it also improves the resonances' positions. The latter observation can be related to an increase in the size of the active Hilbert space when including unbound Auger-Meitner electrons. This demonstrates how any truncation of single particle basis or many-body basis leads to deviations in calculated energies as compared to measured ones. Hence, to improve agreement in the resonances' positions, a larger basis set is needed. On the other hand, an increased size of the active space drastically slows down calculations. Consequently, different methods should be incorporated in our approach as techniques from renormalization for instance.

4.2. Determination of the Q -value

The sensitivity on the neutrino masses also directly depends on the precision in the knowledge of the Q -value, the energy difference between the ^{163}Ho and ^{163}Dy ground states, since the difference between Q and the spectral endpoint is the lowest rest mass of the neutrinos. In publication [2] we used Bayesian parameter estimation to determine the Q -value from low background data in combination with the calculated spectrum described in the previous section. This yields $Q = 2.838 \pm 0.014$ keV in full agreement with the value from Penning trap mass-spectrometry [5]. At the time of publication our estimate of the Q -value has been the most precise so far. Here, we

4. Bound state resonances in the electron capture spectrum

describe the Bayesian analysis in more detail.

In the expression for the differential decay rate (2.60) we see that the dependency of the electron capture spectrum on the Q-value is encoded in the neutrino phase-space factor. We could use the calculated Green's functions $G^\pm(\omega)$ and fit (2.60) to the low background data with Q as fit-parameter. However, as outlined before the peak positions differ from the experimental results by a few eV. Furthermore, lorentzian broadening does not adequately describe the asymmetric line-shapes. These theoretical uncertainties hinder a precise determination of the Q-value.

Instead we need to define quantities which are insensitive to these uncertainties and can be obtained from both experiment and theory. The total spectral weight of resonances is such a quantity. If resonances are clearly separated, one can integrate the spectrum over an interval, containing (almost) the full spectral weight of this resonance. Since one performs an integral over energies, the position of the resonance only marginally affects this integral. Furthermore, the integrated spectral weight is to good approximation independent of the exact line-shape, as broadening only shifts weight in energy.

Let I_τ denote the interval that contains 99% of the spectral weight of resonance $\tau \in \{4s, 4p_{1/2}, 3s, 3p_{1/2}\}$. In our theoretical calculation the spectral weight Ω_τ contained in a resonance is easily computed as

$$\Omega_\tau^{\text{theo}} = \int_{I_\tau} \frac{d\Gamma(\omega)}{d\omega} d\omega \quad . \quad (4.6)$$

For the experimental data, it is difficult to resolve resonances which are close to each other. Thus in order to separate the 3s and 3p_{1/2} resonances we fit a lorentzian to the 3p_{1/2} resonance and subtract the spectral weight of this lorentzian contained in I_{3s} from Ω_{3s}^{exp} . Analogously the same can be done for $\Omega_{3p_{1/2}}^{\text{exp}}$.

The 4s/4p_{1/2} resonances are more complicated due to the satellite structure on the high energy side of 4s. Therefore, we integrate the full intensity between 252 and 1500 eV, which contains 4s, 4p_{1/2} and the satellite structure, to obtain Ω_4^{exp} which has its pendant

$$\Omega_4^{\text{theo}} = \Omega_{4s}^{\text{theo}} + \Omega_{4p_{1/2}}^{\text{theo}} + \sum_{\sigma \in \text{satellites}} \Omega_\sigma^{\text{theo}} \quad . \quad (4.7)$$

Note that in theory 4s and 4p_{1/2} consist of multiple peaks – especially the latter – which are not resolved by experimental data. This has been shown in figure 4.1 and discussed in section 4.1.

The $\Omega_\tau^{\text{theo}}(Q)$ are functions of the Q-value and hence the latter can be inferred by fitting the theoretical data to the experimental ones Ω_τ^{exp} . For the latter the uncertainties can be obtained from Poissonian statistics underlying the raw data. The theoretical uncertainties due to approximations in the calculation of the EC spectrum and due to the correction of experimental data for overlapping resonances are unknown. Hence, we introduce these as nuisance parameters with a Jeffrey's prior and marginalize them when fitting. Assuming a constant prior for Q leads to a slightly asymmetric posterior distribution with mean at 2.838 keV and a width of 14 eV.

In [2] the obtained data are also compared to the calculations described in section 4.1 not only to determine Q , but also to discuss the effect of line-broadening. Thus additionally to the Lorentzian broadening the asymmetric Mahan broadening [112] has been discussed. The findings confirm that Lorentzian broadening is insufficient to describe the spectral endpoint and that the line-shape is asymmetric with increased spectral weight in the high energy tails of the resonances. This leads to an increase in intensity in the endpoint region, which improves sensitivity to the neutrino mass determination. To understand this increase and the spectral line-shape, an ab-initio calculation of spectral broadening is desirable and we present such calculation in chapter 5.

4.3. Outlook: Hyperfine interaction

Hyperfine interaction between electrons and nucleons couples angular momenta J_e and I_i to total angular momentum F and lifts the corresponding degeneracy of the Hamiltonian without hyperfine interaction. This degeneracy is typically lifted at the order of μeV [113], which raises the question to which extent this effect becomes observable in the electron capture spectrum.

If we want to study the impact of hyperfine interaction on the spectrum, we have to use (2.58) for calculations, which is more accurate than (2.60) and directly includes coupling of angular momenta via Clebsch-Gordan coefficients. However, the simplified expression (2.60) may already serve us to estimate the order of magnitude of this impact. Therefore, we plotted the spectrum calculated according to (2.60) in figure 4.3. The black curve corresponds to capture of electrons with spin down, the red curve corresponds to capture of spin up electrons. At the major resonances differences between the two spectra are clearly visible. For spin up capture one obtains a single M_1 (3s) peak, but for spin down capture there are two peaks at the M_1 position. The same holds for N_1 (4s). Additionally the satellite structures on the right of N_1 seem to depend strongly on the spin of the captured electron.

The reason for the observed differences in the two spectra lies in the angular momenta of the states after electron capture. If we start with the Ho ground-state having $M_e = -\frac{15}{2}$ ($J_e = \frac{15}{2}$), then the state after electron capture has a core hole with either $j_z = \frac{1}{2}$ (spin up capture) or $j_z = -\frac{1}{2}$ (spin down capture). In the former case the total final angular momentum is $M_e^{\text{final}} = -8$ which implies that the excited states have $J_e^{\text{final}} = 8$. In the latter case the total final angular momentum is $M_e^{\text{final}} = -7$ which implies that the excited states have $J_e^{\text{final}} = 8$ or $J_e^{\text{final}} = 7$. Hence, in case of spin down capture, states with two different J_e^{final} can be reached instead of only one as in the case of spin up capture. Electronic Coulomb interaction is responsible for the energy splitting of the $J_e^{\text{final}} = 8$ and $J_e^{\text{final}} = 7$ states. Therefore, these splittings are of the order of a few electron Volts [114]. As a consequence the M_1 (3s) resonance is split into two peaks for spin down capture and is a single peak for spin up capture. The same reasoning applies for N_1 (4s) and its satellite structures. The satellites however, are more complicated as they involve two holes due to relaxation processes subsequent

4. Bound state resonances in the electron capture spectrum

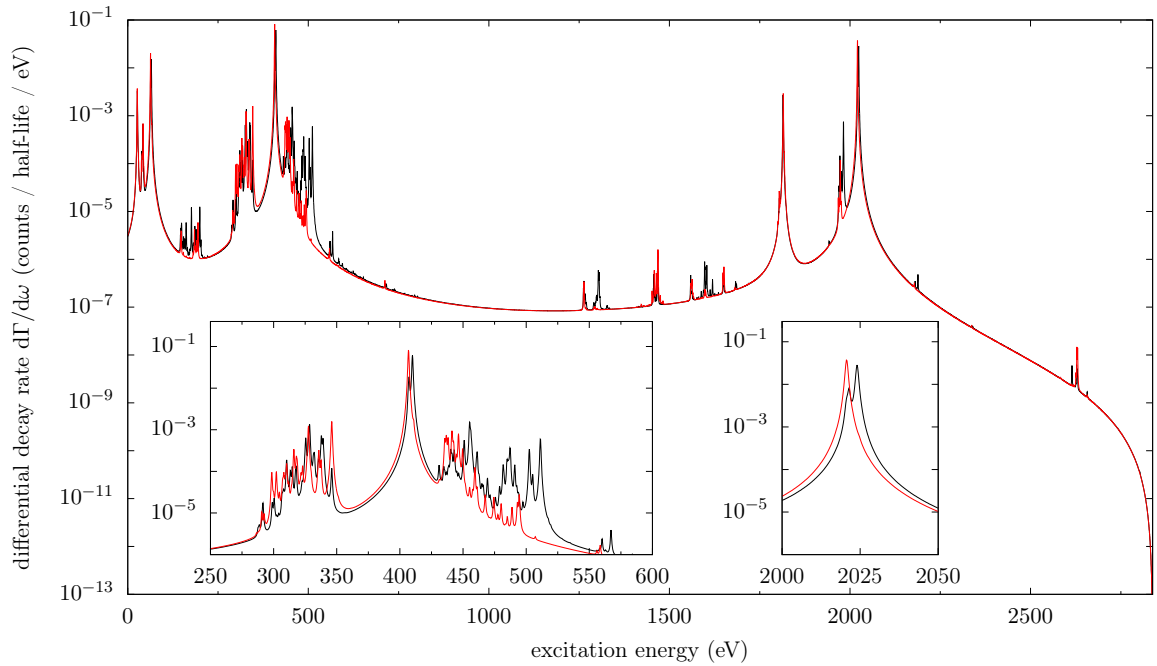


Figure 4.3.: Electron capture spectrum (2.60) where an electron has been captured with spin down (black) and spin up (red). The electronic propagator (2.59) is calculated for $M_e^1 = M_e^2 = -\frac{15}{2}$.

to electron capture.

An experimental measurement of the spectrum is insensitive to whether a spin up or spin down electron has been captured. Hence, the discussed differences cannot be observed directly, but indirectly instead, which is where hyperfine interactions become important. As outlined in section 2.5, these interactions couple angular momenta of electrons and nucleus. The coupling strengths are determined by Clebsch-Gordan coefficients in (2.58) and they will determine how spin up and spin down capture spectra contribute to the total spectrum. As Clebsch-Gordan coefficients depend on the total angular momentum F , we can expect that the full spectrum will also depend on F . In this case, the differences between spectra of different F are related to the differences in spin up and spin down capture spectra, and hence we expect them to be at the same energy scale of a few electron Volts.

It is worth noting, that energy-shifts, which are directly related to hyperfine interactions, are much smaller as compared to the aforementioned shifts related to Coulomb interaction. Therefore, at finite temperature the system is in a mixed state where the amount of admixture of a given F is determined by Boltzmann statistics. This induces a temperature dependence of the electron capture spectrum [114].

To observe this dependence in experiment, detectors must be able to resolve spectral shifts of the order of multiplet-splitting due to Coulomb interaction, which is easier to achieve than spectral resolution down to hyperfine-splitting. To calculate

4.3. Outlook: Hyperfine interaction

the temperature dependent spectrum, one has to go beyond approximation (2.60) and use (2.58) instead. However, this involves more computational resources, since the propagator $G_e^\pm(\omega)$ (2.59) has to be calculated for all possible values of M_e^1 and M_e^2 . Some of the corresponding states involve 16 times as many Slater-determinants as the $M_e = -\frac{15}{2}$ state used so far.

5. Unbound states and line-broadening

So far we assumed that the line-shapes of the resonances in the electron capture spectrum are lorentzian, but we saw in the previous chapter that this is not an appropriate description. The line-widths have been adjusted to match experimental data, however now we want to determine line-shapes from first principles. Therefore, we study the Auger-Meitner effect [115,116] and its impact on the spectrum. As the effect transfers electrons into unbound states with continuous energies, it is precisely what we need to compute broadening of resonances.

The Auger-Meitner effect is introduced in section 5.1. To include it in our calculations, we extend the single particle basis functions by eigen-differentials, which are capable of describing unbound states with continuous energy spectrum, in section 5.2. Combining this extended basis with our calculation for bound states from the previous chapter is made possible by introducing a self-energy in section 5.3. This allows for a numerically efficient handling of the Hilbert-space which has become very large after extending the single particle basis. Section 5.4 details the numerical calculations and how the electron capture spectrum is calculated including line-broadening due to the Auger-Meitner effect.

Methods and results from this chapter have been published in [3] and are reviewed here in greater detail.

5.1. The Auger-Meitner effect

To improve our understanding of the spectral shape, we need to look at those processes that are responsible for line-broadening. Broadening is encoded in the continuous spectrum of the Hamiltonian (2.16) which has so far been studied on the sub-space of bound states. There the Hamiltonian has a discrete spectrum only. Hence, we need to identify those interactions that couple the bound-state sub-space to sub-spaces with unbound electrons. The latter can assume continuous energy-eigenvalues. To put it differently, we need to identify those relaxation mechanisms that allow a bound-state-resonance to decay into a continuum of states. Such decays have life-times which are inversely proportional to the line-width of the decaying resonance.

An example of such a process is the Auger-Meitner effect, which was discovered by Lise Meitner in 1922 [115] and Paul Auger independently in 1923 [116]. The Auger-Meitner effect is depicted schematically in figure 5.1. It can occur in an excited atom if the excitation energy is higher than the atom's ionization energy. In highly excited atoms there is typically a hole in the inner shells. An electron from a higher shell can

5. Unbound states and line-broadening

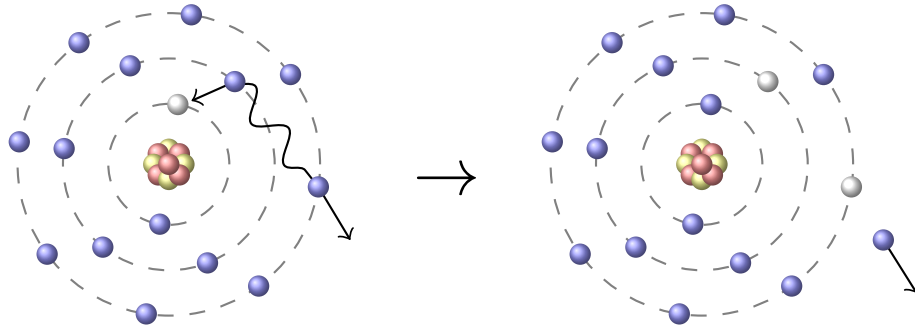


Figure 5.1.: Schematic view on the Auger-Meitner process. We see an excited atom with one hole (white) in the inner shells. The atom de-excites when an electron (blue) fills this hole by transferring its energy to another electron. The latter escapes the Coulomb potential of the nucleus (red and yellow) leaving an ionized atom behind.

fill up this hole and transfer the energy difference between those shells to another electron via Coulomb interaction. If the transferred energy is large enough, the second electron can escape the attractive potential of the nucleus and leaves the now ionized atom as a free electron with a remaining kinetic energy. The values of this kinetic energy are continuous. Hence, Auger-Meitner scattering couples bound excited states to the continuous spectrum of the Hamiltonian.

Since this effect is caused by electronic Coulomb repulsion, the relevant dynamics are already encoded in the Coulomb operator (2.40) and the kinematics in Dirac's Hamiltonian (2.34). However, as these have been expanded on bound atomic orbitals, we need to extend the single-particle basis in order to include unbound electrons in the expansion. This is done in the next section where we see that the extension drastically increases the number of single-particle states and consequently also the Hilbert-space. To handle this, we develop an approximation in section 5.3 that allows for an efficient numerical implementation.

5.2. A single-particle basis made of eigen-differentials

Different methods have been developed to deal with eigenfunctions of an operator which are not square-integrable, as they belong to the operator's continuous eigenvalues. Here we use the method of eigendifferentials invented by Herman Weyl [117] and developed further by Olga Rubtsova and coworkers [118]. We closely follow the latter reference.

While eigenfunctions $\phi_\varepsilon(\mathbf{x})$ corresponding to the continuous spectrum $\varepsilon \in [0, \infty)$ of a self-adjoint operator h are typically not square-integrable, they obey an orthogonality relation

$$\int \phi_\varepsilon^*(x) \phi_{\varepsilon'}(x) dx = \delta(\varepsilon - \varepsilon') \quad . \quad (5.1)$$

5.2. A single-particle basis made of eigen-differentials

Plane waves $e^{-i\mathbf{q}\mathbf{x}}$ which are eigen-functions of the momentum operator and describe free particles with momentum $\hbar\mathbf{q}$ are a typical example.

We want to use these eigen-functions $\phi_\varepsilon(x)$ to construct a countable, orthonormal basis, on which the single-particle Hamiltonian h has a simple form. If we divide the continuous spectrum $[0, \infty)$ into disjoint intervals $[\varepsilon_n, \varepsilon_{n+1})$ of equal length $\Delta = \varepsilon_{n+1} - \varepsilon_n$, we can define wave-packets according to [118]

$$\psi_n(x) = \frac{1}{\sqrt{\Delta}} \int_{\varepsilon_n}^{\varepsilon_{n+1}} \phi_\varepsilon(x) d\varepsilon . \quad (5.2)$$

These are orthonormal

$$\begin{aligned} \int \psi_m^*(x) \psi_n(x) dx &= \frac{1}{\Delta} \int_{\varepsilon_m}^{\varepsilon_{m+1}} \phi_\varepsilon^*(x) d\varepsilon \int_{\varepsilon_n}^{\varepsilon_{n+1}} \phi_{\varepsilon'}(x) d\varepsilon' dx \\ &= \frac{1}{\Delta} \int_{\varepsilon_m}^{\varepsilon_{m+1}} \int_{\varepsilon_n}^{\varepsilon_{n+1}} \delta(\varepsilon - \varepsilon') d\varepsilon d\varepsilon' = \begin{cases} 1 & \text{if } \varepsilon \in [\varepsilon_n, \varepsilon_{n+1}) \\ 0 & \text{otherwise} \end{cases} = \delta_{mn} \end{aligned} \quad (5.3)$$

and using $h\phi_\varepsilon(x) = \varepsilon\phi_\varepsilon(x)$ we obtain for the matrix elements

$$\begin{aligned} h_{mn} &\equiv \int \psi_m^*(x) h \psi_n(x) dx = \frac{1}{\Delta} \int_{\varepsilon_m}^{\varepsilon_{m+1}} \phi_\varepsilon^*(x) d\varepsilon \int_{\varepsilon_n}^{\varepsilon_{n+1}} \varepsilon' \phi_{\varepsilon'}(x) d\varepsilon' dx \\ &= \frac{1}{\Delta} \int_{\varepsilon_m}^{\varepsilon_{m+1}} \int_{\varepsilon_n}^{\varepsilon_{n+1}} \varepsilon' \delta(\varepsilon - \varepsilon') d\varepsilon d\varepsilon' = \delta_{mn} \frac{\varepsilon_{m+1}^2 - \varepsilon_m^2}{2\Delta} . \end{aligned} \quad (5.4)$$

If we take the limit of $\Delta \rightarrow 0$ the wave-packets approach the eigen-functions corresponding to the continuous spectrum $\psi_n(x) \rightarrow \phi_{\varepsilon_n}(x)$ and $h_{mn} \rightarrow \delta_{mn}\varepsilon_n$. Thus the $\psi_n(x)$ are called eigen-differentials and we can use them to approximate the continuous spectrum to in principle arbitrary precision.

One can obtain similar sets of eigen-differentials with the same properties as above via [118]

$$\psi_n(x) = \int_{\varepsilon_n}^{\varepsilon_{n+1}} f(\varepsilon) \phi_\varepsilon(x) d\varepsilon \quad \text{with} \quad \int_{\varepsilon_n}^{\varepsilon_{n+1}} |f(\varepsilon)|^2 d\varepsilon = 1 . \quad (5.5)$$

We directly see that this generalizes (5.2) and the matrix elements become

$$h_{mn} = \delta_{mn} \int_{\varepsilon_n}^{\varepsilon_{n+1}} \varepsilon |f(\varepsilon)|^2 d\varepsilon . \quad (5.6)$$

Since, our one-particle basis of Kohn-Sham orbitals described in section 2.4.1 is spherically symmetric, we want to retain this symmetry in our eigen-differentials. Therefore, we start from the one-particle eigen-functions $\phi_{\tau,\varepsilon}(\mathbf{x})$ of Dirac's Hamiltonian (2.9) which are determined by (2.31) with radial parts $g(r) = rG(r)$ and $f(r) =$

5. Unbound states and line-broadening

$rF(r)$ given as

$$g_{q,\kappa}(r) = \mathcal{N} r j_l(qr) \quad (5.7)$$

$$f_{q,\kappa}(r) = \mathcal{N} \text{sign}(\kappa) \frac{q}{\varepsilon_q + m} r j_{\bar{l}}(qr) \quad (5.8)$$

$$\mathcal{N} = \frac{\sqrt{2}q}{\sqrt{\pi \left[1 + \left(\frac{q}{\varepsilon_q + m} \right)^2 \right]}} \quad \varepsilon_q = \sqrt{q^2 + m^2} \quad (5.9)$$

These are the same as for the free neutrino (2.46) but with the mass m of the electron. Hence, we can analogously label the single-particle states by quantum numbers $\tau_\varepsilon = \{q, \kappa, m_{j_z}\}$ where q is the absolute value of the electron's momentum. As mentioned in (2.49) the normalization is chosen such that the radial wave-functions are orthonormal in the sense of (5.1) and we can proceed as described above to construct eigen-differentials by dividing the energy spectrum into disjoint intervals. The corresponding momenta can be obtained from the relativistic dispersion relation (5.9). However, for the calculation of the electron capture spectrum in Ho the Q-value is much smaller than an electron's rest mass and hence the non-relativistic energy-momentum relation $q = \sqrt{2\varepsilon/m}$ can be used.

Since the experimental energy resolution of the spectrum shown in [2,3] is between 5.4 and 9.2 eV, we can choose to decompose the continuous energy spectrum into intervals of length $\Delta = 2$ eV in order to be well below experimental resolution. Then we can use the eigen-functions $\phi_{\tau_\varepsilon}(\mathbf{x})$ to construct eigen-differentials ψ_{τ_ε} according to (5.2). As $Q = 2838$ eV [2] and $\Delta = 2$ eV, it is sufficient to use the first $N_\varepsilon = 2000$ eigen-differentials for each value of $\kappa \in \{\pm 1, \pm 2, \dots, \pm 5\}$ to cover the energy range of the electron capture spectrum and avoid boundary effects due to a truncated basis of eigen-differentials. The latter aspect is assured since the eigen-differentials involve eigen-functions with energies from 0 to 4 keV, thereby largely exceeding the spectral endpoint.

Now we have eigen-differentials that we can use to extend our single-particle basis of bound, atomic orbitals constructed in chapter 4. However, the former are not orthogonal to the latter. Hence, orthogonalization has to be done manually. As the bound orbitals are already mutually orthogonal and optimized to describe bound states, the orthogonalization scheme should not alter these. Thus we combine bound orbitals $\phi_{b,\tau}$ and eigen-differentials ψ_{τ_ε} in one row vector $\Phi = (\phi_{b,1}, \dots, \phi_{b,N_b}, \psi_{\tau_\varepsilon^1}, \dots, \psi_{\tau_\varepsilon^{N_\varepsilon}})$ and calculate the overlap matrix $S = \int \Phi^\dagger \Phi d^3x$ of bound orbitals and eigen-differentials. A Cholesky-decomposition [119] is applied to the overlap matrix such that $S = LU$, where L and U are lower and upper triangle matrices respectively with $L = U^\dagger$. Defining $\Psi = \Phi U^{-1}$ we obtain $\int \Psi^\dagger \Psi d^3x = L^{-1} S U^{-1} = \mathbb{1}$ implying that Ψ is a set of orthonormal vectors. Since the N_b bound orbitals have been orthonormal already, the first $N_b \times N_b$ block of U is the $N_b \times N_b$ identity matrix. Thus, the first N_b entries of Ψ are precisely the unchanged bound atomic orbitals. The remaining entries Ψ_ε have contributions from both eigen-differentials and bound or-

5.2. A single-particle basis made of eigen-differentials

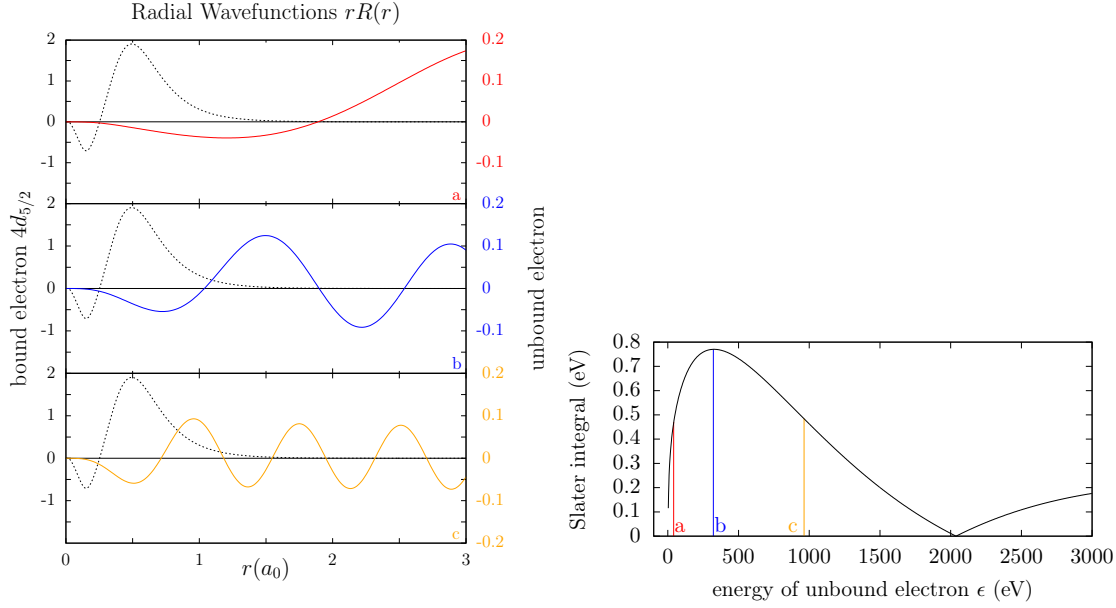


Figure 5.2.: The left panel shows a comparison between a bound 4d orbital (grey, dashed) and eigen-differentials which are single-particle wave-functions of unbound electrons (colors). The unbound electrons have different energies which are color-coded and marked in the right panel. The cross-section for the release of an Auger-Meitner electron with energy ϵ via the scattering $e_{4p}^- + e_{4d}^- \rightarrow e_{4s}^- + e_{\epsilon f}^-$ depends on the Coulomb slater integral shown in the right panel as a function of the Auger-Meitner electron's energy. The energy dependence directly corresponds to the overlap between bound and unbound wave-functions shown in the left panel. Taken from [3]

bitals. Therefore, their matrix-elements of Dirac's Hamiltonian are not simply given by (5.4). It is impossible to achieve matrix-elements in the form (5.4) and orthogonality to the bound orbitals simultaneously. As for our calculations the latter is more important, we assure exact orthonormality by the algorithm just described and try to reach the form (5.4) approximately. Thus we rotate the last N_ϵ vectors from Ψ (denoted Ψ_ϵ) such that the projection of Dirac's Hamiltonian onto the corresponding sub-space is diagonal with entries ϵ_n . This results in the final single-particle basis, which we use this chapter to calculate the line-broadening of bound resonances due to the Auger-Meitner effect. As these basis vectors are linear combinations of bound single-particle wave-functions and unbound eigen-differentials ψ_{τ_ϵ} , their energies differ from $(\epsilon_{n+1}^2 - \epsilon_n^2)/2\Delta$ (5.4) slightly. To account for this hybridization effect, the diagonal entries ϵ_n are used to represent the unbound electrons' kinetic energies (note the difference between ϵ_n , obtained by diagonalizing Dirac's Hamiltonian on the sub-space spanned by Ψ_ϵ , and ϵ_n which are the chosen energy discretizations).

5. Unbound states and line-broadening

In figure 5.2 eigen-differentials describing unbound electrons at different energies are shown. From plot a to c one observes an oscillatory behavior with decreasing wave-length for increasing energy, which is typical of unbound electrons. Electrons can be scattered into these states by the Auger-Meitner effect. For example a 4p electron can fall into the 4s hole previously created by electron capture and thereby scatter a 4d electron into an unbound f state leaving the atom as Auger-Meitner electron with remaining energy ϵ . We denote this process as $e_{4p}^- + e_{4d}^- \rightarrow e_{4s}^- + e_{\epsilon f}^-$. The cross-section for this process depends on the Coulomb Slater integral $U_{\epsilon f, 4s, 4d, 4p}$ which is shown in the right panel of figure 5.2 as a function of the Auger-Meitner electron's energy. We see that the Slater integral rises quickly until it reaches a maximum and descends slowly until hitting zero. From this point a second rise occurs which is less pronounced.

This behavior can be understood by comparing the wave-functions of the electron in its initially bound 4d orbital and in its final unbound state described by eigen-differentials as shown in figure 5.2. At small ϵ – marked red – the overlap between initial and final wave-function is small and therefore also the corresponding Slater integral. Increasing ϵ leads to the shortening of wave-length and thus a larger overlap with the bound 4d orbital. Hence, also the Slater integral increases. At the energy marked blue the overlap is maximal and a further increase in ϵ leads to stronger oscillations (orange) which in turn reduce the Slater integral of the Auger-Meitner process. Slightly above 2 keV a point is reached where the oscillations completely cancel the overlap and above this point overlap and Slater integral start to increase again. However, the now strongly oscillating eigen-differentials do not yield Slater integrals as high as the ones at larger wavelengths.

These observations explain the energy dependence of the Slater integrals. This directly influences the spectral line-broadening as we will show in the following sections. We already saw that this energy dependence is a largely asymmetric function, which will be reflected in the line-shape of the resonances.

5.3. Self-energy

The single-particle basis obtained in the previous section cannot simply be used to construct the full Hamiltonian (2.16) and repeat the calculation from chapter 4. The number of single-particle orbitals now exceeds 10^5 leading to a Hilbert-space dimension of 10^{279} in the case of 66 electrons. Furthermore, the number of involved Slater integrals is even too high to store the Hamiltonian in a sparse, second quantization representation on RAM. Hence, we need to find a good approximation that includes Auger-Meitner decay and the continuous spectrum.

If an excited state corresponding to one of the bound resonances decays via Auger-Meitner processes, it is most likely that only a single Auger-Meitner electron is created. The creation of multiple Auger-Meitner electrons is the more unlikely the more electrons are created, as this is related to higher order processes in perturbation theory. Thus, our first approximation is to restrict the Hilbert-space to states that involve

at most one Auger-Meitner electron. As a consequence we can neglect interactions between multiple Auger-Meitner electrons completely, which greatly simplifies the Hamiltonian.

Furthermore, we assume that all Hartree terms ($e_\epsilon^\dagger e_{\tau_1}^\dagger e_{\tau_1} e_{\tau_2}$) involving eigen-differentials can be absorbed into the one-particle energies ϵ_n of the eigen-differentials. Thus, the only terms which are added to the Hamiltonian of bound states (2.16) in order to include the continuous energy spectrum are kinetic energy

$$K_A = \sum_{\epsilon_n, \kappa, m_j} \epsilon_n e_{\epsilon_n, \kappa, m_j}^\dagger e_{\epsilon_n, \kappa, m_j} \equiv \sum_{\epsilon} \epsilon e_\epsilon^\dagger e_\epsilon \quad (5.10)$$

and Coulomb scattering terms which govern the Auger-Meitner process itself

$$U_A = \sum_{\epsilon} \sum_{\tau_1 \neq \tau_3} \sum_{\tau_2} U_{\epsilon \tau_1 \tau_2 \tau_3} e_\epsilon^\dagger e_{\tau_1}^\dagger e_{\tau_3} e_{\tau_2} + \text{h.c.} \equiv \sum_{\epsilon} U_\epsilon e_\epsilon^\dagger + \text{h.c.} \quad (5.11)$$

$U_{\epsilon \tau_1 \tau_2 \tau_3}$ are given by the Coulomb matrix-elements (2.42) where one single-particle wave-function is an eigen-differential. Note that $\sum_{\tau_1 \neq \tau_3}$ assures no Hartree terms are included as mentioned above. The total Hamiltonian is given by [3]

$$H_{\text{eff}} = H_D + V_C + U_{\text{eff}} + H_W + H_\nu + K_A + U_A \quad . \quad (5.12)$$

If we divide the Hilbert space into a sector without Auger-Meitner electrons and a sector where states include one Auger-Meitner electron, we see that only U_A couples these two. On the other hand, the electron capture spectrum is obtained from (2.59)

$$G_e^-(\omega) = \langle \psi_e, J_e, M_e^1 | e_{\tau_e}^\dagger (\omega + i0 - H_D - V_C - U_{\text{eff}} - K_A - U_A)^{-1} e_{\tau_e} | \psi_e, J_e, M_e^2 \rangle \quad (5.13)$$

where the expectation value is taken with respect to states that involve bound electrons only. Hence, we can insert a projection onto the corresponding subspace which we denote $P_b = \sum_b |\psi_b\rangle \langle \psi_b|$. The sum runs over all many-body bound eigen-states of $H_D + V_C + U_{\text{eff}}$ with 66 electrons after electron capture. We already obtained a good approximation of these in chapter 4 using Lanczos' algorithm. This yields

$$G_e^-(\omega) = \langle \psi_e, J_e, M_e^1 | e_{\tau_e}^\dagger (\omega + i0 - H_B - \Sigma(\omega))^{-1} e_{\tau_e} | \psi_e, J_e, M_e^2 \rangle \quad (5.14)$$

where we denoted the projection of the Hamiltonian onto bound eigen-states as

$$H_B = \sum_b |\psi_b\rangle \langle \psi_b| H_D + V_C + U_{\text{eff}} | \psi_b\rangle \langle \psi_b| \equiv E_b | \psi_b\rangle \langle \psi_b| \quad (5.15)$$

and introduced a self-energy

$$\Sigma(\omega) = \sum_{bb'} |\psi_b\rangle \langle \psi_b| U_A (\omega + i0 - H_D - V_C - U_{\text{eff}} - K_A)^{-1} U_A | \psi_{b'}\rangle \langle \psi_{b'}| \quad . \quad (5.16)$$

5. Unbound states and line-broadening

For a proof of (5.14) and (5.16) see the appendix of [3]. Inserting (5.11) and direct calculation simplify the self-energy to

$$\Sigma(\omega) = \sum_{bb'} |\psi_b\rangle \sum_{\epsilon} \langle \psi_b | U_{\epsilon}^{\dagger} (\omega + i0 - H_D - V_C - U_{\text{eff}} - \epsilon)^{-1} U_{\epsilon} | \psi_{b'} \rangle \langle \psi_{b'} | . \quad (5.17)$$

We denote the energy dependent matrix elements as

$$\Sigma_{bb'}(\omega, \epsilon) \equiv \langle \psi_b | U_{\epsilon}^{\dagger} (\omega + i0 - H_D - V_C - U_{\text{eff}} - \epsilon)^{-1} U_{\epsilon} | \psi_{b'} \rangle . \quad (5.18)$$

Thus we reduced the problem of inverting the full Hamiltonian in (5.13) to inverting a projected Hamiltonian (5.15) plus self-energy, where the projected subspace is given by those bound states we already treated in chapter 4. Hence, the remaining most difficult task is the evaluation of (5.18). In section 5.4 we put this expression into a format more suitable for numerical implementation. Here we want to discuss the meaning of this self-energy instead and gain some intuitive understanding. Therefore, we insert unity $\sum_{E_n} |n\rangle \langle n|$ in terms of eigen-states of $H_D + V_C + U_{\text{eff}}$ and use (2.5) such that

$$\Sigma_{bb'}(\omega, \epsilon) = \mathcal{P} \sum_{E_n} \frac{\langle \psi_b | U_{\epsilon}^{\dagger} | n \rangle \langle n | U_{\epsilon} | \psi_{b'} \rangle}{\omega - E_n - \epsilon} - i\pi \sum_{E_n} \delta(\omega - E_n - \epsilon) \langle \psi_b | U_{\epsilon}^{\dagger} | n \rangle \langle n | U_{\epsilon} | \psi_{b'} \rangle . \quad (5.19)$$

Thus, the negative imaginary part of the self-energy's diagonal elements is precisely the cross-section for Auger-Meitner scattering encoded in U_{ϵ} where the bound state ψ_b decays via emission of an Auger-Meitner electron with energy ϵ . To put it differently $\sum_{\epsilon} \text{Im} [-\Sigma_{bb}(E_b, \epsilon)]$ is the lorentzian line-width of the resonance in the electron capture spectrum at E_b . Its inverse is the resonance's life-time with respect to Auger-Meitner decay. Hence, the self-energy includes the canonical line-width of bound resonances, but also incorporates an energy dependent line-broadening for the full spectrum. For every value of the Auger-Meitner electron's energy ϵ the self-energy has resonances at $\omega = E_n + \epsilon$ each weighted with the matrix element $|\langle n | U_{\epsilon} | \psi_b \rangle|^2$. In the limit of infinitesimally spaced ϵ the sum turns into an integral and $\Sigma(\omega)$ becomes a continuous function of the excitation energy ω . For numerical calculations we replace the infinitesimal $i0$ in (5.18) by the energy spacing $i\Delta$, which leads to a smooth self energy even before taking the limit $\Delta \rightarrow 0$. This results in an overall, energy-dependent line-broadening of the electron capture spectrum.

To illustrate this, we continue the example from the previous section, where the 4s resonance couples to unbound states via $e_{4p}^- + e_{4d}^- \rightarrow e_{4s}^- + e_{\epsilon f}^-$. The imaginary part of the corresponding self-energy's diagonal entry is shown in figure 5.3. In this case the Auger-Meitner effect creates two holes. One in 4p and one in 4d. Hence, at the energy of this two-hole state the self-energy's imaginary part, or cross-section, rises rapidly and closely follows the shape of the corresponding Slater integrals shown in figure 5.2. Thus, the two particle scattering amplitudes influence the shape of the cross-section most dominantly. However, its shape is slightly modified by the presence of bound electrons in initial and final states, or to put it differently by many-body

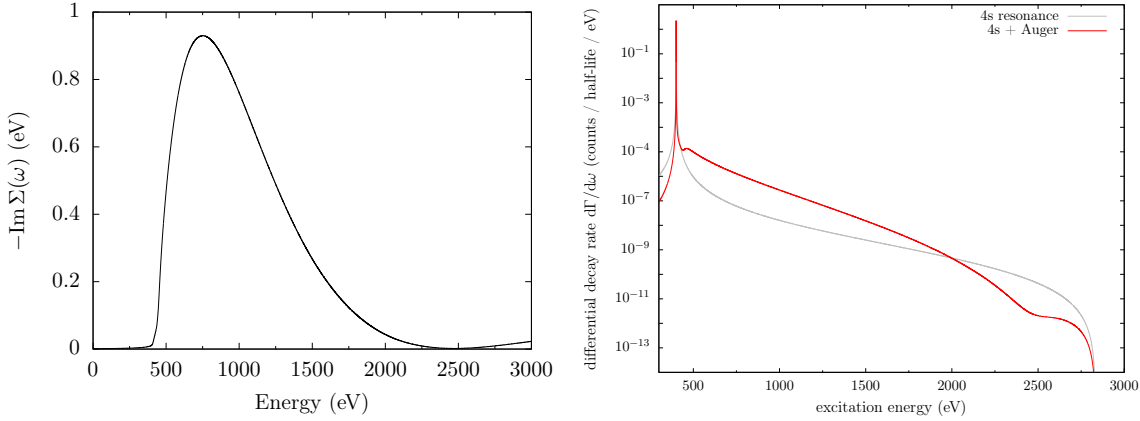


Figure 5.3.: The Auger-Meitner effect couples the 4s resonance to unbound states via scattering $e_{4p}^- + e_{4d}^- \rightarrow e_{4s}^- + e_{\epsilon_f}^-$. This can be described by a self-energy (5.18) where ψ_b is the bound-state determining the 4s resonance. The left panel shows the imaginary part of the corresponding self-energy's diagonal entry. The right panel compares the spectral shape of the 4s resonance assuming lorentzian broadening (grey) and broadening according to the self-energy from the left panel (red). Taken from [3].

effects. This suppresses the self-energy at higher energies, which is most prominent in the second rise above 2.5 keV.

The impact of the self-energy on the spectrum is shown in the right panel of figure 5.3. The resonance gets a small width and asymmetric tails. As the final states with Auger-Meitner electron have to be at energies above the 4p4d-two-hole state, the high energy wing of the resonance has much more intensity than the low energy wing. One can observe a small bump at the corresponding ionization-energy threshold needed to create the two-hole state and eject the 4d electron. A second bump can be found above 2.5 keV which corresponds to the second rise in self-energy and Slater integrals. However, it is further suppressed by the neutrino phase space factor. Comparing the spectral shape due to self-energy and a lorentzian resonance in figure 5.3, shows that the Auger-Meitner effect does not only lead to increased spectral weight on the high energy side of the resonance, but also leads to line-shapes with different curvature. Both effects become important in the endpoint regime, as the former implies more counts in the region sensitive to the neutrino mass and the latter needs to be well understood in order to extract neutrino masses from the spectrum [3]. We will discuss this in section 5.4.

So far we have discussed the imaginary part of the self-energy. Its real part takes into account that hybridization between bound states and states with Auger-Meitner electrons shifts the energies of the resonances. Since states with Auger-Meitner electron are at higher energies than the corresponding initial state with bound electrons only, the self-energy's real part will shift the bound resonances to lower absolute en-

5. Unbound states and line-broadening

ergies. However, it will also shift the ground-state energy. Thus the resonances' positions relative to the ground-state energy can be shifted to both lower and higher energies. In the following section we demonstrate that these shifts improve agreement with experiment.

The off-diagonal elements of the self-energy will mix the bound resonances and give rise to interference. There are multiple ways how different bound resonances can decay into the same final state with Auger-Meitner electron. The coupling of these resonances to the continuous spectrum comes with a phase and hence the different decay channels can interfere. In the next section we show that this interference is constructive on the high energy side of a resonance and destructive on the low energy side. This comes in addition to the energy dependent line broadening discussed above and leads to line-shapes as described by Fano [120].

5.4. How to calculate self-energy and spectrum

The most straightforward way to determine the self-energy would be to directly calculate (5.18) using the Block-Lanczos algorithm described in section 3.2. For every ϵ one can create a set $\{U_\epsilon|\psi_b\rangle\}$ of starting vectors and apply the algorithm. However, each of these calculations takes days and doing this for every ϵ is massively resource intensive. Hence, a more sophisticated approach is necessary.

Therefore, we study the matrix-elements of the self-energy (5.18), which after insertion of unity in terms of eigen-states of the bound-state Hamiltonian $H_D + V_C + U_{\text{eff}}$ read

$$\Sigma_{bb'}(\omega, \epsilon) = \sum_{E_n} \frac{\langle \psi_b | U_\epsilon^\dagger | n \rangle \langle n | U_\epsilon | \psi_{b'} \rangle}{\omega + i0 - E_n - \epsilon} . \quad (5.20)$$

To evaluate this expression we first need to determine the eigen-states $|n\rangle$, which can be done using the Block-Lanczos routine as described in section 3.2. To construct starting vectors we pick bound-state eigen-vectors $\{|\psi_b\rangle\}$ belonging to the most dominant resonances of the spectrum calculated in chapter 4 and shown in figure 4.1. These are 226 states. The starting vectors are then given as $\{U_\epsilon|\psi_b\rangle\}$ for some fixed ϵ and not for every ϵ as discussed above. This assures that every starting vector contains exactly 65 electrons, since out of the initial 67 electrons in the Ho ground-state one has been captured by the nucleus and another one escaped the atom via the Auger-Meitner effect. In this way Lanczos' algorithm provides us with an eigen-basis of $H_D + V_C + U_{\text{eff}}$ for the sub-space with 65 bound and one Auger-Meitner electron.

Now we have to evaluate $\langle n | U_\epsilon | \psi_b \rangle$ for every value of ϵ . This task can be sped up by separating the dependence on ϵ as

$$\langle n | U_\epsilon | \psi_b \rangle = \sum_{\tau_1 \neq \tau_3} \sum_{\tau_2} U_{\epsilon\tau_1\tau_2\tau_3} \langle n | e_{\tau_1}^\dagger e_{\tau_3} e_{\tau_2} | \psi_b \rangle . \quad (5.21)$$

In this expression the most time-consuming task is the evaluation of $\langle n | e_{\tau_1}^\dagger e_{\tau_3} e_{\tau_2} | \psi_b \rangle$. Hence, the separation of this expression from the energy dependent $U_{\epsilon\tau_1\tau_2\tau_3}$ allows

5.4. How to calculate self-energy and spectrum

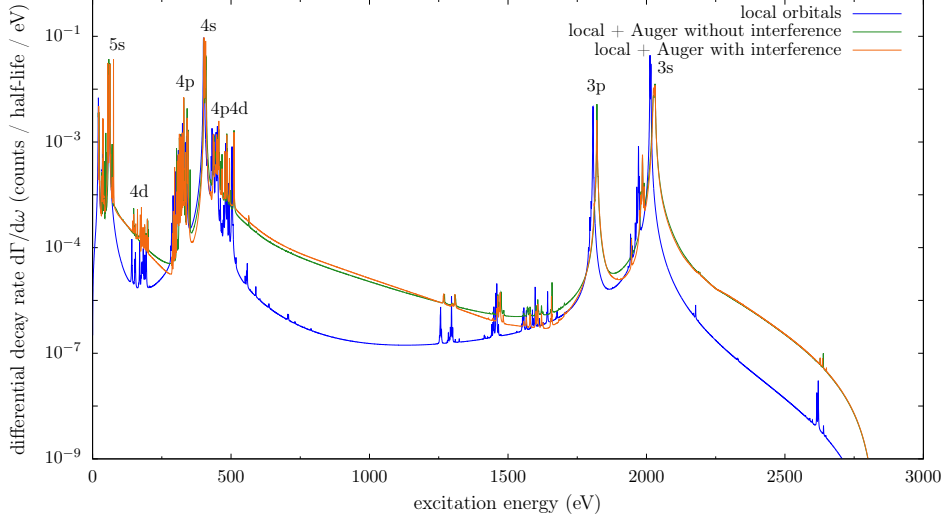


Figure 5.4.: Electron capture spectrum calculated including locally bound orbitals (blue, fig. 4.1) and additionally relaxation due to Auger-Meitner scattering (green/orange). The blue curve assumes a constant lorentzian broadening, the others obtain broadening due to the Auger-Meitner effect. While the green curve uses the diagonal entries of the self-energy only, the orange one includes the full self-energy matrix such that the bound resonances are coupled to each other, which leads to constructive/destructive interference on the high/low energy wings of resonances. Taken from [3].

to calculate $\langle n | e_{\tau_1}^\dagger e_{\tau_3} e_{\tau_2} | \psi_b \rangle$ once and reuse it for every ϵ . This gives an important performance boost when calculating the full self-energy $\Sigma_{bb'}(\omega) = \sum_{\epsilon} \Sigma_{bb'}(\omega, \epsilon)$.

Having calculated the self-energy, we can easily plot the spectrum using (5.14). The results are shown in figure 5.4. Comparison with the spectrum where lorentzian line-widths have been assumed (blue curve) shows that our ab initio approach to line-broadening predicts a different shape. Features of this shape are determined by energy dependent broadening, which becomes most apparent when observing that the resonances 3s and 4s have different widths and that their high energy tails carry more spectral weight than the respective low energy tails.

Compared to the calculation including bound local orbitals only, resonances are shifted in energy. These shifts are present due to the self-energy's real part which takes hybridization between bound and unbound states into account.

Fano's effect [120] can be observed by comparing green and orange curves. The former involves the diagonal entries of the self-energy only, while the latter also includes the off-diagonal ones which reflect that there are multiple decay channels which reach the same unbound final state starting from different bound resonances. These channels interfere destructively or constructively as a function of energy depending on the phases a final state acquires during relaxation. Thereby intensity is decreased in the low energy wings and increased in the high energy wings of resonances.

5. Unbound states and line-broadening

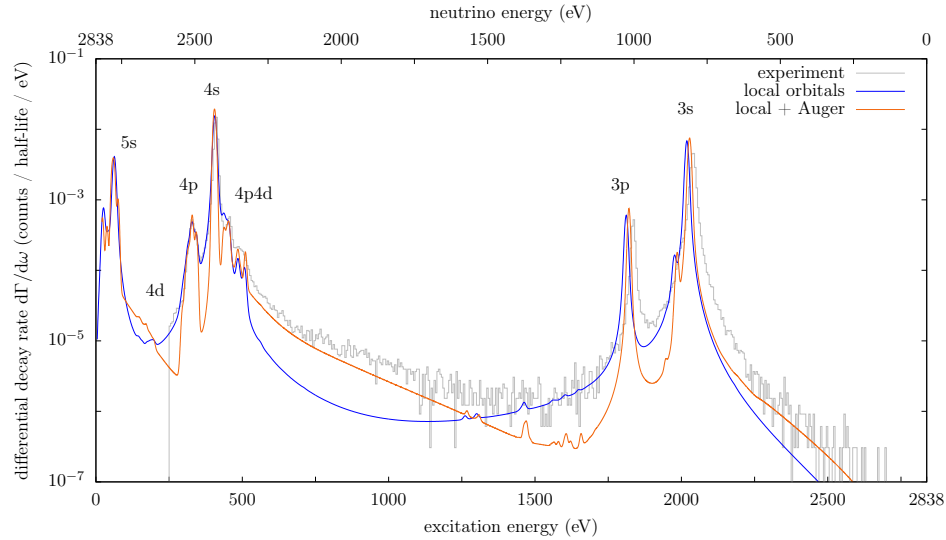


Figure 5.5.: Comparison of the electron capture spectrum obtained experimentally [2] (grey), from calculations including only bound, local states under assumption of lorentzian broadening [1] (blue) and including additionally unbound states and energy-dependent broadening due to Auger-Meitner effect [3] (orange). The orange curve improves agreement with experiment as compared to the blue one in terms of shifted peaks and increased intensity in high energy wings of resonances most notably for the 4s and 3s edges. Calculated curves are convoluted with a Gaussian to account for detector broadening.

To show that all the above spectral modifications improve agreement between theory and experiment, we plot the spectrum from chapter 4 including bound lorentzian resonances together with the one from this chapter and experimental data [2] in figure 5.5. It becomes apparent that the energy shifts, due to the self-energy's real part, improve the positions of resonances most notably for those at higher energy like 3s and $3p_{1/2}$. It is not surprising that there the shift is more pronounced compared to 4s, since at higher energies more unbound states are available for coupling to a resonance. In addition, we notice that more available unbound states lead to stronger broadening at higher than at lower energies (compare 3s and 4s), since real and imaginary part of the self-energy are connected by Kramers-Kronig relation. This was not present in the lorentzian description of resonances. It would have to be included manually for every peak. Furthermore, in the region between 4s and 3s we see that lorentzian broadening is not capable of explaining the intensity in the resonances' tails. Here the asymmetry of self-energy broadening becomes important which accounts for most of the experimentally observed spectral weight. Especially in the endpoint region the Auger-Meitner effect leads to an increase in intensity which is reproduced in our calculation, but cannot be described by a symmetric, lorentzian 3s resonance.

5.4. How to calculate self-energy and spectrum

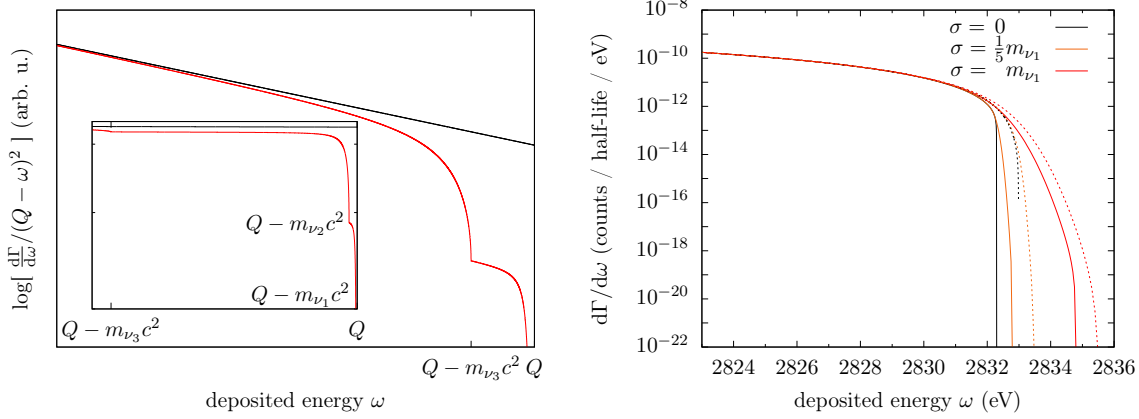


Figure 5.6.: Effect of finite neutrino masses on the endpoint region. The Auger-Meitner effect leads to an exponentially decaying line-shape far off a resonance. Left: if the spectrum is divided by $(Q - \omega)^2$, one observes a straight line for massless neutrinos (black). Finite neutrino masses modify this line-shape (red). Right: to simulate detector resolution, the endpoint regime has been convoluted with a Gaussian of width σ . Dashed lines depict the spectral line-shape for massless neutrinos, full lines correspond to massive neutrinos. The lightest neutrino mass has been assumed to be $m_{\nu_1} = 0.5$ eV and $Q = 2.833$ keV has been chosen according to [5].

However, one still observes differences compared to experimental data. Peak positions are still off, the width of 3s is too small and intensity is missing between resonances. All of this indicates that further decay channels are important and have to be included. Channels which couple bound resonances to further continua are needed besides those involved in the Auger-Meitner effect. These could include Fluorescence decay, where electrons de-excite via emission of a photon, or interaction with the chemical environment, since in the experimental setup the Ho atom is surrounded by gold. This provides a band-structure in which electrons can scatter escaping their Ho orbitals. Furthermore, the gold environment changes the valence configuration of Ho which might open additional Auger-Meitner channels not yet included in our calculation. Also double Auger-Meitner decay is in principle possible, where two electrons are ejected simultaneously, but we expect this to be much less important than the standard Auger-Meitner effect, as the Coulomb-matrix elements for emission of two electrons are smaller than those for emission of a single electron.

In the above discussion we saw that the Auger-Meitner effect and the associated line-broadening dominate the high energy wings of resonances. Now we want to study the impact of this on the spectral endpoint, which is shown in the left plot of figure 5.6. The self-energy shows exponential decay for large values of the deposited energy ω . Thus, a logarithmic plot of the spectrum divided by the phase space factor of mass-less neutrinos yields a straight line (black) far from resonances. Finite neu-

5. Unbound states and line-broadening

trino masses alter this straight line with kinks at each $\omega = Q - m_{\nu_a} c^2$ (red). This is very similar to figure 2.1. However, the difference between these plots is the functional dependence on ω . Far from a lorentzian resonance as in figure 2.1 the plot $\log \left[\frac{d\Gamma}{d\omega} / (Q - \omega)^2 \right]$ behaves as $\sim -2 \log \omega$. On the other hand for an exponentially decaying self-energy as in the left panel of figure 5.6 we have $\log \left[\frac{d\Gamma}{d\omega} / (Q - \omega)^2 \right] \sim -\omega$. The latter dependence is not only simpler but also comes from a much more accurate description of the spectral broadening. This again stresses the importance of a precise understanding of line-shapes and furthermore demonstrates that the spectral endpoint region has a simpler shape than expected. Hence, determination of neutrino masses from the electron capture spectrum appears to be very fruitful, given experimental data with sufficiently high statistics and resolution.

To demonstrate how experimental resolution affects the capability of precisely determining neutrino masses, we convolute the spectrum with Gaussians of different widths to model detector-broadening. This is shown in the right plot of figure 5.6. The separation between curves for massive (full lines) and massless (dashed lines) neutrinos increases with improved resolutions and intensity. Thus, with a better resolution less counts are needed in order to distinguish between massive and massless neutrinos.

5.5. Outlook: Fluorescence

A further relaxation mechanism leading to line-broadening is fluorescence decay. After electron capture the excited states can decay via spontaneous emission of a photon. The energy spectrum of photons is continuous similar to Auger-Meitner electrons. Hence, coupling bound states to the electro-magnetic field results in further line-broadening.

To include spontaneous photo-emission, we need to quantize the electro-magnetic field. This is done in Coulomb gauge. The Hamiltonian governing interactions between electrons and electro-magnetic field reads

$$H_{EM} = e \int \bar{\psi}_e(\mathbf{x}) \gamma^i A_i(\mathbf{x}) \psi_e(\mathbf{x}) d^3x \quad . \quad (5.22)$$

Canonically quantizing the vector potential leads to

$$\mathbf{A}(\mathbf{x}) = \frac{1}{\sqrt{2}} \sum_{\lambda=1}^2 \frac{1}{(2\pi)^{\frac{3}{2}}} \int \omega_p^{-\frac{1}{2}} \boldsymbol{\varepsilon}_\lambda(\mathbf{p}) \left(a_\lambda(\mathbf{p}) e^{-i\mathbf{p}\mathbf{x}} + a_\lambda^\dagger(\mathbf{p}) e^{i\mathbf{p}\mathbf{x}} \right) d^3p \quad (5.23)$$

where $\boldsymbol{\varepsilon}_\lambda(\mathbf{p})$ is a polarization vector fulfilling $\boldsymbol{\varepsilon}_\lambda(\mathbf{p}) \cdot \mathbf{p} = 0$ and $\omega_p = c|\mathbf{p}|$ is a photon's dispersion relation. The operators $a_\lambda^\dagger(\mathbf{p})$ and $a_\lambda(\mathbf{p})$ respectively create and annihilate a photon with momentum \mathbf{p} and polarization λ . They obey the canonical commutation relation $[a_\lambda(\mathbf{p}), a_{\lambda'}^\dagger(\mathbf{q})] = \delta_{\lambda\lambda'} \delta(\mathbf{p} - \mathbf{q})$. The photons' kinetic energy

reads

$$H_\gamma = \sum_{\lambda=1}^2 \int \omega_p a_\lambda^\dagger(\mathbf{p}) a_\lambda(\mathbf{p}) d^3p \quad . \quad (5.24)$$

Now we introduce the transition operator

$$T_\lambda(\mathbf{p}) = \int \bar{\psi}_e(\mathbf{x}) \gamma^i \varepsilon_{i,\lambda}(\mathbf{p}) e^{i\mathbf{p}\cdot\mathbf{x}} \psi_e(\mathbf{x}) d^3x \quad (5.25)$$

such that

$$H_{\text{EM}} = \frac{e}{\sqrt{2}} \sum_{\lambda=1}^2 \frac{1}{(2\pi)^{\frac{3}{2}}} \int \omega_p^{-\frac{1}{2}} \left(a_\lambda(\mathbf{p}) T_\lambda^\dagger(\mathbf{p}) + a_\lambda^\dagger(\mathbf{p}) T_\lambda(\mathbf{p}) \right) d^3p \quad . \quad (5.26)$$

In this form we directly see that H_{EM} couples the sub-space of bound electronic states without photons to the sub-space where a single photon is present. Spontaneous emission of two or more photons simultaneously is a higher order process. If we hence neglect this, we can include relaxation due to fluorescence in full analogy to the Auger-Meitner effect via a self-energy

$$\Sigma_{bb'}(\omega) = \langle \psi_b | H_{\text{EM}} \frac{1}{\omega + i0 - H - H_\gamma} H_{\text{EM}} | \psi_{b'} \rangle \quad (5.27)$$

with $H = H_D + V_C + U_{\text{eff}}$. Inserting (5.26) and simplifying yields

$$\Sigma_{bb'}(\omega) = \frac{e^2}{2(2\pi)^3} \sum_{\lambda=1}^2 \int \frac{1}{\omega_p} \langle \psi_b | T_\lambda^\dagger(\mathbf{p}) \frac{1}{\omega + i0 - H - \omega_p} T_\lambda(\mathbf{p}) | \psi_{b'} \rangle d^3p \quad . \quad (5.28)$$

Once calculated numerically this self-energy can be added to its Auger-Meitner pendant (5.18) and contributes to spectral broadening.

To get some insights into $\Sigma_{bb'}$, we split it into its real and imaginary part

$$\text{Re } \Sigma_{bb'}(\omega) = \frac{e^2}{2(2\pi)^3} \sum_{\lambda=1}^2 \mathcal{P} \int \frac{1}{\omega_p} \langle \psi_b | T_\lambda^\dagger(\mathbf{p}) \frac{1}{\omega - H - \omega_p} T_\lambda(\mathbf{p}) | \psi_{b'} \rangle d^3p \quad (5.29)$$

$$\text{Im } \Sigma_{bb'}(\omega) = -\frac{e^2\pi}{2(2\pi)^3} \sum_{\lambda=1}^2 \int \frac{1}{\omega_p} \langle \psi_b | T_\lambda^\dagger(\mathbf{p}) \delta(\omega - H - \omega_p) T_\lambda(\mathbf{p}) | \psi_{b'} \rangle d^3p \quad . \quad (5.30)$$

In dipole approximation $T_\lambda(\mathbf{p})$ does not depend on the absolute value of momentum $p \equiv |\mathbf{p}|$. Hence, performing the integral over the latter in spherical coordinates yields for the imaginary part

$$\text{Im } \Sigma_{bb'}(\omega) = -\frac{e^2\pi}{2(2\pi)^3} \sum_{\lambda=1}^2 \int \langle \psi_b | T_\lambda^\dagger(\mathbf{p}) (\omega - H) \Theta[\omega - H] T_\lambda(\mathbf{p}) | \psi_{b'} \rangle d\Omega_p \quad . \quad (5.31)$$

Here the Heaviside Θ -function has been introduced. The above expression shows that broadening due to dipole transitions becomes important for large ω . In the case

5. Unbound states and line-broadening

of ^{163}Ho the excitation energy ω is however restricted to be below the Q-value of 2.838 keV, which implies that we can expect the broadening to be small compared to its Auger-Meitner pendant.

The self-energy's real part involves a principle-value integral with integrand of Order $\mathcal{O}(p^0)$ which is divergent. This shows that the classical multipole expansion of the electro-magnetic field is not applicable if calculation of the real part is necessary to determine shifts of resonant energies. Instead one could expand $\varepsilon_\lambda(\mathbf{p})e^{i\mathbf{p}\cdot\mathbf{x}}$ in terms of vector-spherical harmonics and spherical Bessel functions. This would also simplify the calculation of the matrix elements of $T_\lambda(\mathbf{p})$, since electronic fields are given on a spherical basis.

6. Broadening due to Auger-Meitner effect in x-ray spectroscopy

An excited state can decay due to the Auger-Meitner effect regardless of how the excitation has been created as long as its energy is above the ionization threshold of the atom. X-ray spectroscopy uses photons to excite electrons in atoms, molecules or crystals. Hence, we demonstrate in this chapter that the methods developed in chapter 5 are also applicable to further spectroscopic techniques different from electron capture spectroscopy.

Shooting x-rays onto matter can lead to absorption, elastic or in-elastic scattering and emission of photo-electrons. Recording spectral information of these processes probes the electronic, chemical and geometric structure of materials under study [121,122]. However, to infer properties from recorded spectra, theoretical models and calculations are necessary that can be compared to experimental data [123]. To understand spectral line-shapes, broadening due to the Auger-Meitner effect is important as we already showed for electron capture spectroscopy and as we will show here for x-ray absorption spectroscopy (XAS) and resonant in-elastic x-ray spectroscopy (RIXS) applied to Nickel oxide (NiO).

An XAS spectrum is recorded by measuring the absorption probability of photons as a function of their energy. Different types of spectral features are observable in different energy regimes. As the principle structure of these regimes is similar for many materials, one typically classifies spectroscopic techniques according to the regime under study [122].

With highly energetic x-rays one can excite electrons from the 1s shell to the lowest unoccupied p-shell and to the continuum. This is referred to as K-edge XAS, where spectral features are dominated by a strong edge at the resonant energy of the $1s \rightarrow np$ transition [124–126].

Above the edge there are so called near edge structures (XANES) due to both bound and un-bound states [127]. The broadening of these bound state structures involves contributions from the Auger-Meitner effect, which is why our method has applications in this regime. At even higher energies the spectrum is dominated by so called extended x-ray absorption fine structures (EXAFS) which correspond to states where the 1s electron has directly been released as photo-electron. They show interference patterns due to scattering off neighboring atoms [128].

At energies below the edge, a further peak, a pre-edge, can emerge if scattering from 1s to a shell lower than the already lowest unoccupied p-shell is possible. In the case of transition metals this can be the lowest d-shell with empty orbitals as 3d in Ni for instance. However, this is a higher order transition and hence the corresponding

6. Broadening due to Auger-Meitner effect in x-ray spectroscopy

edge is much smaller as compared to the main edge which results from a dipole transition [122]. Also main edge and pre-edge are broadened due to the Auger-Meitner effect.

Using x-rays with lower energies it is possible to excite 2s or 2p electrons, which is referred to as L-edge XAS. This is more sensitive to electronic structure as compared to K-edge XAS [122]. Due to the lower energy, the contribution to the absorption spectrum from photo-electrons is reduced and hence more spectral features can be resolved. However, these features still obtain broadening due to the Auger-Meitner effect. Therefore, we focus on a $2p \rightarrow 3d$ transition in NiO to demonstrate the capabilities of our self-energy method from the previous chapter.

6.1. X-ray absorption spectroscopy

To calculate the x-ray absorption spectrum of NiO we can proceed in full analogy to electron capture spectroscopy in Ho and use Kubo's formula as in section 2.1. However, here we are interested in excitations due to coupling between electrons and the electro-magnetic field, which promotes a core electron into the valence shell. Hence, we need to apply some changes. The first change concerns the transition operator, which in the case of EC was the weak Hamiltonian and now is the electro-magnetic Hamiltonian H_{EM} (5.26), we already encountered in section 5.5. For simplicity we restrict H_{EM} to excitations between the Ni 2p and 3d shells. The second change concerns the Hamiltonian $H = H_D + V_C + U_{eff} + V_{CF}$ and takes into account that NiO is a crystal and not an isolated atom. While this is in principle also true for Ho embedded in gold, here it is much more important as we are directly probing valence excitations. Hence, we added the crystal field potential V_{CF} which takes into account that rotational symmetry is broken due to the effective potential of the oxygen atoms surrounding Ni. This potential can be expanded on spherical harmonics [129]

$$V_{CF}(\mathbf{x}) = \sum_{L=0}^{\infty} \sum_{M=-L}^L A^{LM}(r) Y_L^M(\theta, \phi) . \quad (6.1)$$

As NiO has octahedral symmetry, the crystal field potential is invariant under action of the corresponding symmetry group. Hence, this expansion contains only spherical harmonics which belong to the trivial irreducible representation a_{1g} of the octahedral group O_h . We can further simplify the above expansion by considering only those terms which couple to d-orbitals. These are the terms with $L \in \{0, 2, 4\}$, of which only $L = 0$ and $L = 4$ involve a_{1g} [130]. $L = 0$ yields a constant offset for all 3d electrons which can be absorbed in a shift of the spectrum as long as all spectral features of interest can be described by a configuration with constant occupation of 3d. More interesting is the $L = 4$ term which leads to a splitting of the ten-fold degenerate d-orbital into a six-fold degenerate orbital belonging to the t_{2g} irreducible representation of O_h and a four-fold degenerate orbital belonging to the e_g irreducible representation. As a_{1g} is one dimensional, there is a dependence between the $(A^{4M})_{M=-4\dots4}$

such that only one parameter D_q has to be determined. With this in mind, the single-particle crystal field potential can be expressed in the basis of the 5 standard d-orbitals as [129]

$$\langle 3d, m_1 | V_{CF} | 3d, m_2 \rangle = D_q \begin{pmatrix} 1 & 0 & 0 & 0 & 5 \\ 0 & -4 & 0 & 0 & 0 \\ 0 & 0 & 6 & 0 & 0 \\ 0 & 0 & 0 & -4 & 0 \\ 5 & 0 & 0 & 0 & 1 \end{pmatrix}_{m_1, m_2} \quad (6.2)$$

From photoemission data one can infer $D_q = 0.11$ eV [131]. We transform the above matrix from its spherical harmonics basis into the basis of spin-weighted spherical harmonics such that we can express V_{CF} in second quantization consistently with the rest of the Hamiltonian $H = H_D + V_C + U_{\text{eff}} + V_{CF}$, which is constructed from a set of Kohn-Sham orbitals obtained from FPLO [81–83] in complete analogy to chapter 2. We include all Ni orbitals up to 3d.

Now we use Lanczos' algorithm to determine the ground state ψ_0 of H and all bound eigenstates ψ_b which couple to the ground state via T_x , T_y , or T_z which are the dipole approximations of the transition operator (5.25) for linearly polarized light in x-, y- and z-direction respectively. As we did not include empty orbitals and the valence shell contains at most two holes in the ground state configuration, the active Hilbert space is small and hence we can determine all these eigenstates exactly. A similar reasoning applies for all the un-bound states including one Auger-Meitner electron.

Within the formalism of chapter 5 the XAS spectrum of NiO now reads

$$\frac{d\Gamma}{d\omega}(\omega) \propto -\text{Im} \sum_{j \in \{x, y, z\}} \langle \psi_0 | T_j (\omega + i0 - H_B - \Sigma(\omega))^{-1} T_j^\dagger | \psi_0 \rangle . \quad (6.3)$$

The sum over linear polarizations in all three dimensions yields an isotropic spectrum. H_B and $\Sigma(\omega)$ have the following matrix-elements

$$(H_B)_{bb'} = \langle \psi_b | H | \psi_{b'} \rangle \quad (6.4)$$

$$\Sigma_{bb'}(\omega) = \sum_{\epsilon} \langle \psi_b | U_{\epsilon}^\dagger (\omega + i0 - H - \epsilon)^{-1} U_{\epsilon} | \psi_{b'} \rangle . \quad (6.5)$$

The continuous energy spectrum ϵ of the eigendifferentials is discretized with 1 eV spacing and cut off at 2 keV to avoid artifacts due to a too small single-particle basis. Auger-Meitner electrons with all possible angular momenta up to $\kappa = \pm 5$ are included.

A plot of the XAS spectrum (6.3) is shown in figure 6.1. Since we focused on an excitation where a 2p electron absorbs a photon and is transferred to a 3d orbital, we observe two major edges L_3 and L_2 . Due to the crystal-field the latter is split into two peaks corresponding to the irreducible representations t_{2g} and e_g of the octahedral symmetry group. In literature [130] the observation that the t_{2g} peak is at lower energies compared to e_g is often explained intuitively by the shape of the involved d

6. Broadening due to Auger-Meitner effect in x-ray spectroscopy

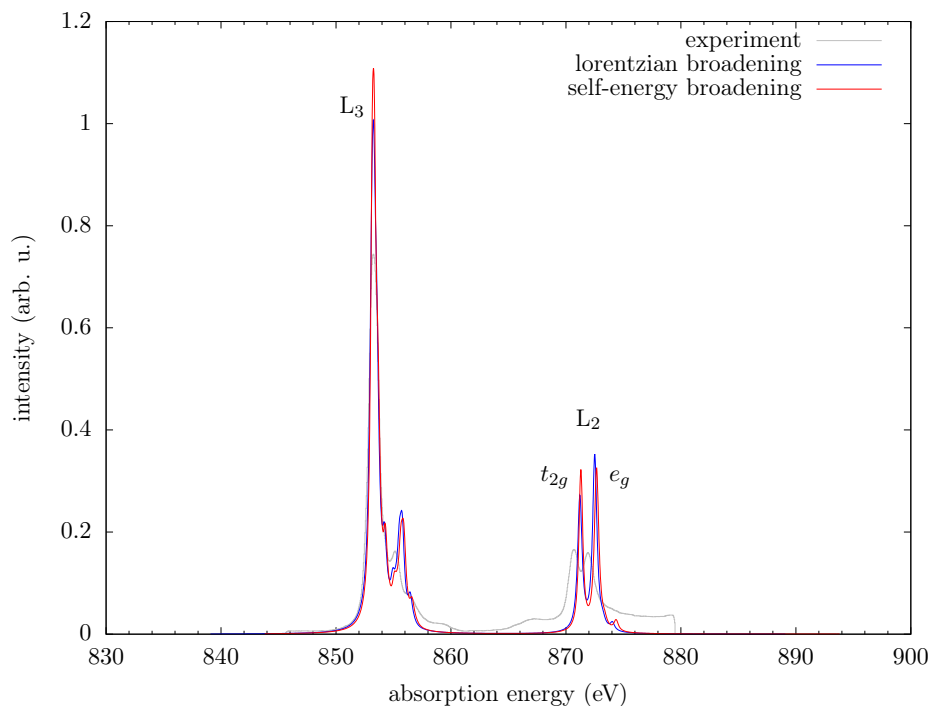


Figure 6.1.: Isotropic XAS spectrum of NiO for an excitation $2p^63d^8 \rightarrow 2p^53d^9$. The lorentzian broadening (blue) has been chosen to match the self-energy broadening. Comparison with experiment [132] shows that further relaxation channels aside from the Auger-Meitner effect have a strong impact on line-broadening. The spectra are shifted in energy to match experimental data. Normalizations are determined such that the L_3 edge (energy range [845.65, 854.6]) has an integral equal to 1.

orbitals. While the lobes of the e_g orbitals d_{z^2} and $d_{x^2-y^2}$ point towards the surrounding, negatively charged oxygen sites, the lobes of the t_{2g} orbitals d_{xy} , d_{xz} and d_{yz} point between the oxygen sites. Hence, the latter orbitals are influenced less strongly by the repulsive oxygen potential than the former and consequently are lower in energy. We will point out in chapter 8 that this reasoning based on orbital shapes is problematic if it is not supplemented by group theoretic calculations. A rigorous treatment of crystal field splitting can also be found in [130].

More interesting are the relative heights of t_{2g} and e_g peaks. If one compares the calculation where an overall constant lorentzian broadening has been assumed (blue) to the calculation where energy dependent self-energy broadening has been used (red), one observes that the e_g peak is much higher than the t_{2g} peak for the blue curve, but peaks have almost equal height for the red curve. This shows that the self-energy broadens t_{2g} less than e_g and hence also improves the relative amplitudes of resonances compared to experiment. The observation that the e_g peak obtains more broadening as compared to t_{2g} can be explained by the fact that the e_g resonance is

at a higher energy and hence the space of available Auger-Meitner states is larger as for t_{2g} , which directly leads to a larger Auger-Meitner cross-section and consequently more broadening.

Clearly, there are discrepancies between theory and experiment. The L_2 and L_3 edges are broader in experiment than in theory. The continuous background underlying the L_2 edge indicates the reason for this. This background is related to broadening due to coupling to the chemical environment, or to put it differently to the band structure of NiO which has not been considered in our calculation so far. This coupling is also responsible for L_2 being broadened more strongly than L_3 . As broadening is related to energy shifts via Kramers-Kronig relation between real and imaginary part of the self-energy, we can expect that additional coupling to the chemical environment will also shift L_2 relative to L_3 and thereby does not only correct for missing line-width but also for the observed discrepancy in peak positions. Currently the difference in positions of L_2 and L_3 is related to spin-orbit coupling for electrons in an atomic potential. Once the chemical environment is included, this difference will be related to spin-orbit coupling for electrons in the effective potential of NiO and thus will yield more accurate results. It would be possible to directly include the correct spin-orbit coupling from a DFT calculation, but then care has to be taken when calculating the self-energy due to the chemical environment. In this case one has to assure consistency between all onsite energies of the Ni atom as well as of the chemical environment in order not to obtain the correction on spin orbit coupling twice (once from DFT and once from the self-energy's real part). We give a brief outlook on inclusion of the chemical environment in section 6.3 and continue with another spectroscopic method in the next section.

6.2. Resonant inelastic x-ray spectroscopy

Resonant inelastic x-ray spectroscopy (RIXS) is a technique capable of probing low energy excitations in solids. By measuring energy, momentum, or polarization of an x-ray photon before and after it has been scattered inelastically off a material probe it is possible to infer the dispersion relation of phonons [133], magnons [134] and further properties of the material due to d-d excitations [135], charge transfer [136] and plasmons [137]. The change in the photons momentum, polarization and energy can be related to different properties of excitations via theoretical calculations and models. Hence, one can either test the precision of *ab initio* calculations, or extract phenomenological model parameters. This way it is possible to study complex materials and their properties which are important for photosynthesis [138], batteries [139] and superconductivity [140] to name only a few. A detailed discussion of the above and further aspects can be found in the review [141].

In this section we demonstrate how to apply our self-energy method from chapter 5 to calculate line-broadening due to the Auger-Meitner effect in a RIXS spectrum of NiO. Such a spectrum involves two-photon processes. An incoming photon is absorbed and resonantly excites a transition. In our example the photon is linearly

6. Broadening due to Auger-Meitner effect in x-ray spectroscopy

polarized in x-direction and excites a $2p^63d^8 \rightarrow 2p^53d^9$ transition at a Ni site. This excited state decays via emission of another photon, where we measure polarization in y-direction as well as its energy loss due to the inelastic scattering. Hence, the system does not necessarily return to its ground-state, but to an excited state with small excitation energy. This way it is possible to study the low excitation energies at the order of a few eV with photons at hundreds of eV or even keV. The spectrum can be calculated according to the Kramers-Heisenberg formula [141, 142]

$$\frac{d^2\Gamma}{d\omega_{\text{in}}d\omega_{\text{out}}} \propto \frac{\omega_{\text{out}}}{\omega_{\text{in}}} \sum_{\psi_f} \left| \sum_{\psi_n} \frac{\langle \psi_f | T_y | \psi_n \rangle \langle \psi_n | T_x | \psi_0 \rangle}{E_0 - E_n + \omega_{\text{in}} + i0} \right|^2 \delta(E_f + \omega_{\text{out}} - E_0 - \omega_{\text{in}}) \quad (6.6)$$

Here $\omega_{\text{in/out}}$ denote the energies of the in- and out-coming photon. For $2p \rightarrow 3d$ excitations in NiO their quotient is to good approximation equal to one, because the photon's energy loss is below 1% of its energy. ψ_f and ψ_n are final and intermediate eigenstates of H with electronic energies E_f and E_n respectively. E_0 is the electronic energy of the ground state ψ_0 .

The Kramers-Heisenberg formula is similar to Fermi's golden rule [19], but describes processes at higher order perturbation theory. We can proceed in full analogy to section 2.1 where we showed equivalence between Fermi's golden rule and Kubo's formula by replacing Dirac's δ -distribution by the imaginary part of a propagator

$$\frac{d^2\Gamma}{d\omega_{\text{in}}d\omega_{\text{out}}} \propto -\text{Im} \langle \psi_0 | T_x \frac{1}{\omega_{\text{in}} - H + i0} T_y \frac{1}{\omega - H + i0} T_y^\dagger \frac{1}{\omega_{\text{in}} - H + i0} T_x^\dagger | \psi_0 \rangle \quad (6.7)$$

We introduced the energy loss of the photon $\omega \equiv \omega_{\text{in}} - \omega_{\text{out}}$ and absorbed the ground state energy E_0 in the Hamiltonian H to clean up notation.

We proceed analogously to the XAS spectrum from the previous section and calculate the self-energy for the excited states. This results in the final expression for the RIXS spectrum

$$\frac{d^2\Gamma}{d\omega_{\text{in}}d\omega_{\text{out}}} \propto -\text{Im} \langle \psi_0 | T_x \frac{1}{\omega_{\text{in}} - H_B - \Sigma(\omega_{\text{in}}) + i0} T_y \frac{1}{\omega - H_B + i0} T_y^\dagger \frac{1}{\omega_{\text{in}} - H_B - \Sigma(\omega_{\text{in}}) + i0} T_x^\dagger | \psi_0 \rangle \quad (6.8)$$

Note that there is no self-energy in the propagator in the middle as these low lying excitations are below the ionization threshold. In this regime broadening is probably dominated by coupling to the chemical environment. For numerical purposes we replace the infinitesimal $i0$ by a small but finite value of $i25$ meV.

The RIXS spectrum for a $2p^63d^8 \rightarrow 2p^53d^9$ excitation is shown in figure 6.2. Similar to the XAS spectrum we observe an L_2 and L_3 resonance. The former shows crystal field splitting and the intensity ratio of t_{2g} and e_g peaks depends on the energy loss of the photon. Since relative intensities are also influenced by energy dependent

6.3. Outlook: Including the chemical environment

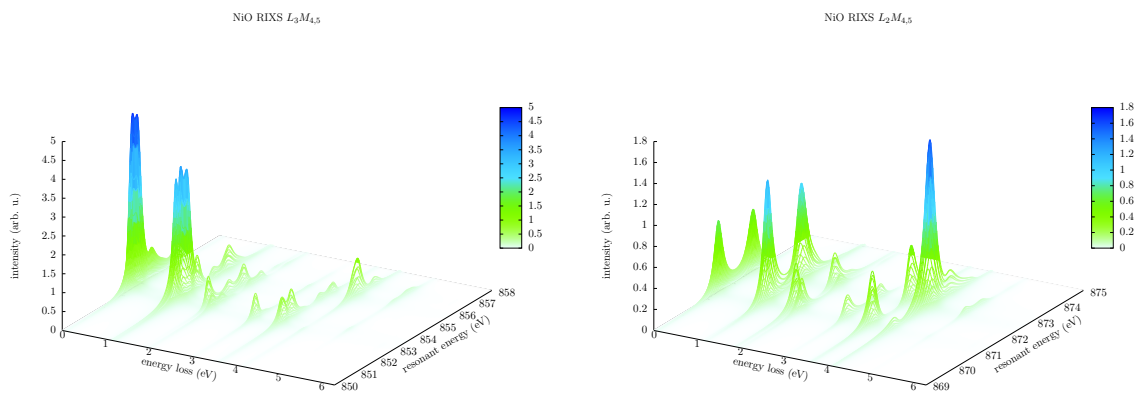


Figure 6.2.: RIXS spectrum of NiO for an excitation $2p^63d^8 \rightarrow 2p^53d^9$. The incoming photon is linearly polarized in x-direction, the outgoing photon is linearly polarized in y-direction. The "resonant energy" axis refers to the energy of the incoming photon at which it can excite a 2p electron into a 3d orbital. The outgoing photon has lost energy as denoted on the other axis. An important feature of including the self-energy due to the Auger-Meitner effect is that the t_{2g} peak of the L_2 resonance is broadened less than the e_g peak.

broadening as we saw in the XAS spectrum, taking the self-energy due to the Auger-Meitner effect into account was important in the calculation of this RIXS spectrum. That t_{2g} and e_g broaden differently can be best seen at an energy loss of 1 eV.

By looking at the L_3 edge, we notice a lot of smaller satellite structures, especially when the photon loses 2 eV of energy or more. These structures strongly depend on the valence electrons. In order to calculate them correctly, it would be necessary to at least include the oxygen ligand orbitals in the computation, or even better the band structure of the NiO crystal. However, this drastically increases the required computational resources and poses further difficulties as we describe in the outlook of the next section.

6.3. Outlook: Including the chemical environment

In order to correctly calculate satellite features due to valence excitations the chemical environment of the excited atom or molecule plays an important role. The presence of ligands allows electrons to hop to other sites and thus modifies ground state configuration and excitation energies. The geometry of the compound under study determines which excitations are possible due to selection rules. The band structure of a crystal represents a continuous energy spectrum into which an electron can be directly excited via a photon leading to continuous spectral features, or indirectly via

6. Broadening due to Auger-Meitner effect in x-ray spectroscopy

relaxation processes subsequent to an initial excitation. This leads to line broadening analogous to the Auger-Meitner effect.

The difficulty in combining the atomic calculations of the spectroscopic techniques as presented in this work with band structure calculations lies in the necessity of an accurate description of the Auger-Meitner self-energy, which involves core-level excitations in multiple shells and electronic correlations, alongside the accurate description of valence and conduction bands. To combine these aspects efficiently, one has to extend the approach of starting from a DFT calculation and including configuration interaction as we did in the previous chapters. Dynamical mean field theory (DMFT) [143, 144] is a proper method to achieve this. It includes correlations locally at one site of a lattice and treats the remaining sites as bath which couples to the correlated site via electronic hopping. This is known as an Anderson impurity model [145].

In this section we describe a simplified approach based on such an Anderson impurity model. This approach is currently under investigation and if it is successful, an extension to a full DMFT calculation is in principle possible and should improve accuracy of calculated spectra.

As before, we start with a DFT calculation for the crystal we want to study with some spectroscopic technique (for example electron capture of Ho embedded in Gold, or XAS/RIXS in NiO). However, besides the atomic Kohn-Sham orbitals for the atom which we want to probe, we also obtain the Kohn-Sham Hamiltonian H_{KS} for the whole crystal. Then we can construct the fully interacting Hamiltonian H_{atom} for the correlated atomic site (e.g. Ho or Ni) according to chapter 2 using the atomic Kohn-Sham orbitals only. The kinematics and dynamics of the bath are encoded in the Kohn-Sham Hamiltonian.

To combine both, we transform the Kohn-Sham Hamiltonian to a tight-binding Hamiltonian H_{tb} with maximally localized Wannier-orbitals. This allows us to single out one site of the crystal lattice at which we replace the onsite terms of the tight binding Hamiltonian with H_{atom} . This gives a Hamiltonian H_{full} with inter-electronic Coulomb interactions at a single site and hopping between all sites. In order to have an accurate band structure, the number of sites has to be large, which prevents us from directly diagonalizing H_{full} or calculating the spectrum. However, a transformation to natural orbitals allows us to simplify the problem [146].

Therefore, we determine the mean-field ground state ψ_{mf} of H_{full} which is given by a single Slater-determinant with N_{el} energetically lowest Kohn-Sham eigen-states (i.e. Bloch functions) occupied and calculate the corresponding single-particle density-matrix $\rho_{mn} = \langle \psi_{\text{mf}} | e_m^\dagger e_n | \psi_{\text{mf}} \rangle$. N_{el} is the number of electrons in the crystal. The indices $m = (\tau, R)$ denote the atomic quantum numbers τ characterizing the Wannier-orbitals and the site R at which the Wannier-orbital is centered, where $R = 0$ denotes the correlated site. As the Wannier-orbitals are not eigenfunctions of the Kohn-Sham Hamiltonian, ρ is not diagonal. If we diagonalize ρ on the sub-space which does not involve the correlated site (i.e. $R \neq 0$) we obtain a transformed density matrix with four different blocks. One block is unchanged and corresponds to the orbitals at $R = 0$. It couples to another block of same dimension which corresponds to a transformed site R' . The two remaining blocks are decoupled. One is the zero matrix,

the other the identity matrix. The former corresponds to sites with natural orbitals which are unoccupied on the mean-field level, the latter corresponds to sites with occupied natural orbitals. (Note that in this context "site" refers to an abstract site in the transformed single-particle space and not in real space.) In this single-particle basis the hopping terms of H_{full} between the fully occupied and fully empty orbitals vanish, but this does not hold for the other hopping terms. However, it is always possible to transform the single-particle basis such that the orbitals at $R = 0$ remain unchanged and there is hopping from $R = 0$ to a single occupied site, a single unoccupied site and to the site R' [146]. The same is true for site R' . In this transformed basis the hopping between occupied sites themselves connects one site to at most two others. The same is true for the unoccupied sites. Figure 1 in [146] nicely illustrates this transformation.

The important features of this transformation are first that the orbitals at the correlated site $R = 0$ are not changed, which allows us to interpret this site as an atom in a bath. Second, the occupations of the bath sites are mostly either completely filled, or completely empty for the mean-field ground-state. This allows us to impose harsh restrictions on the active Hilbert space when calculating the spectrum without introducing large errors. A first restriction would be to include only configurations with a single hole in the previously fully occupied sites and a single electron in the previously empty sites. Accuracy can be increased step-wise by allowing for more holes and excited electrons. With these restrictions and the transformed Hamiltonian we should be able to apply the methods from chapters 3 to 5 to determine an electron capture spectrum of Ho in Gold, an XAS/RIXS spectrum of NiO, or any other x-ray spectrum of further transition metal compounds. The spectrum would include core-level excitations, broadening due to the Auger-Meitner effect and excitations within valence and conduction bands. Thereby the large number of sites results in an almost continuous energy spectrum corresponding to the band structure and yields additional broadening and spectral features. The spacing between these energies can be decreased by increasing the number of sites, thereby approaching the spectrum of an infinitely extended lattice.

The feasibility of this approach is under investigation. The major difficulties to overcome will be first to assure consistency between the atomic energies encoded in H_{atom} and the onsite energies encoded in the tight-binding Hamiltonian. If consistency is not given, artifacts in the self-energy can be seen due to artificial excitations as tests show. Second, an efficient numerical implementation will be necessary. Thus the impact of truncation of the single-particle basis, or the number of sites, restrictions on the many-body Hilbert-space and possibly further approximations needs to be studied carefully.

7. Highly charged ions

In section 4.2 we already tackled the importance of precise knowledge of the Q -value to determine neutrino masses from the electron capture spectrum of ^{163}Ho . There we described how to infer Q from the spectrum itself. However, an independent determination with different systematic errors is desirable when aiming for sensitivities to neutrino masses in the sub-electron-volt regime.

Mass spectroscopy of highly charged ions in Penning traps yields very accurate estimates on the ^{163}Ho Q -value [5]. Since atoms have to be ionized in order to be stored in Penning traps, measurements of Q have to be corrected for the binding energies of the electrons removed from the neutral atoms to reach the ionized state. The binding energies can be calculated from first principles as we will describe in this chapter.

Besides determination of Q , Penning trap mass spectrometry is capable of detecting meta-stable states in highly charged ions [4]. These are of special importance for construction of high precision clocks to set frequency standards [149]. Due to their large life-times, they have narrow line-widths, which is a prerequisite for accurately determining the excitation energy. To identify such states and precisely calculate their excitation energies, computational methods as described in this work are necessary.

With the experimental setup of PENTATRAN [147, 148], measurements of the mass difference between ionized Rhenium $^{187}\text{Re}^{29+}$ and Osmium $^{187}\text{Os}^{29+}$ have been performed, which led to an interesting discovery of a meta-stable excited state in Re^{29+} [4]. Two different cyclotron frequencies of Re^{29+} ions have been detected in the trap. Thus these two ions are in different states. One in the system's ground-state, the other in an excited state, which is meta-stable, since it could be observed for many days. The energy difference between ground and meta-stable state was measured to be 202.2 ± 1.7 eV [4].

In section 7.1 we review the ab initio calculations we performed in [4] for this excitation energy in more detail. Further application of our methods to calculate binding energies can be found in section 7.2.

7.1. Determination of a meta-stable state's excitation energy

To determine the excitation energy of the meta-stable state in Re^{29+} and confirm the experimental observations, we need to calculate the eigen-energies of the Hamiltonian $H = H_D + V_C + U_C$, which governs the dynamics of the 46 remaining elec-

7. Highly charged ions

trons of ionized Rhenium. It is given by Dirac's Hamiltonian (2.34) and the Coulomb operator (2.40). Similar to section 2.4 we obtain a single-particle basis from relativistic Kohn-Sham orbitals out of a DFT calculation using FPLO [81–83]. These are the atomic orbitals of the ionized Re^{29+} atom. Due to the high ionization the Aufbau-principle is no longer valid. Instead one-particle energy levels are the lower, the smaller their principle quantum number is. Hence, on a mean-field level the ground-state configuration is $[\text{Kr}]4d^{10}$ and the first excited states have configuration $[\text{Kr}]4d^9 4f^1$. Using states from these configurations as starting vectors we apply Lanczos' algorithm to determine ground-state and excited state energies as described in section 3.2.

In a first step we use single-particle orbitals 1s to 4f only. From Hund's rules we expect the ground-state to be $[\text{Kr}]4d^{10} \ ^1S_0$, but for the excited state configuration $[\text{Kr}]4d^9 4f^1$ Hund's rules are no longer applicable, since the highly charged Re ion is in a regime where the L-S coupling scheme is not valid. This becomes apparent when observing the excited states as shown in table 7.1. While \mathbf{J} commutes with the Hamiltonian, \mathbf{L}^2 and \mathbf{S}^2 do not. Therefore, their expectation values corresponding to the excited-states are not integers as one would expect in an L-S coupling scheme. Additionally, the table shows that excitation energies do not follow Hund's rules.

However, since the total angular momentum J is a conserved quantum number, we can use it to infer which states are stable against decay into the ground-state by spontaneous emission of photons. The created photon has to carry away the angular momentum difference between ground-state and decaying excited state. The higher this difference, the more unlikely is the decay process. In table 7.1 the highest occurring angular momentum is six ($\langle J^2 \rangle = 42$). However, this state is just above another state that differs in angular momentum by only one ($\langle J^2 \rangle = 30$). Thus the former state can decay into the latter easily by a dipole transition. The latter state however is five quanta of angular momentum above the ground-state. Thus an electric tri-

E (eV)	$\langle J^2 \rangle$	$\langle L^2 \rangle$	$\langle S^2 \rangle$	E	$\langle J^2 \rangle$	$\langle L^2 \rangle$	$\langle S^2 \rangle$
0	0	0	0	211.08	20	15.763	1.4253
196.42	0	2	2	212.97	30	22.385	1.5802
198.79	2	2.5141	1.9996	213.89	12	10.85	1.2554
203.24	6	4.2382	1.9872	214.69	2	5.431	1.9656
203.95	30	29.731	1.2768	220.77	20	27.025	1.5693
206.13	42	30	2	221.74	6	5.981	0.9778
207.06	12	11.068	1.9531	224.22	6	8.2776	1.9605
207.62	6	7.5033	1.0746	226.33	30	27.884	1.143
207.95	20	20.605	1.6604	227.39	12	17.354	1.8904

Table 7.1.: Eigen-energies and angular momenta expectation values of Re^{29+} states. The first entry corresponds to the $[\text{Kr}]4d^{10} \ ^1S_0$ ground-state, the others to excited states with configuration $[\text{Kr}]4d^9 4f^1$.

7.1. Determination of a meta-stable state's excitation energy

acontadipole (E5) transition would be needed for decay into the ground-state, or a hexadecapole (E4) transition to the state at 198.79 eV and a subsequent dipole transition to the ground-state. Both decays are highly unlikely leading to long life-times.

This identifies the meta-stable state observed in experiment. We infer from table 7.1 that this state is dominated by a 3H_5 multiplet, but further states with same J but different L and S also contribute. To accurately determine its excitation energy with respect to the ground-state, we need to include further configurations in our calculation.

Therefore, we increase the one-particle basis step-wise until it includes all orbitals with principle quantum numbers up to six and orbital angular momentum $l = 0 \dots 3$. Also step-wise we include configurations $[Kr]4d^84f^2$, $[Kr]4d^74f^3$ and $[Kr]4d^64f^4$. In this way we can monitor how the excitation energy evolves when going to higher accuracy. The increase of the one-particle basis leads to a monotonic decrease in ground-state and excited state energy. The difference between both also decreases monotonically. On the other hand, the inclusion of further configurations does not show monotonic behavior. This is caused by different strengths in the coupling of the additional configurations to the ground-state and meta-stable state. Since Coulomb interaction involves scattering of two electrons at a time, the ground-state couples more strongly to configurations with even numbers of holes in 4d and even numbers of electrons in 4f. Conversely the meta-stable state obtains larger contributions from configurations with odd numbers of holes in 4d and odd numbers of electrons in 4f. Thus, if one observes the energy difference as a function of included configuration, one finds oscillations. These emerge since consecutive steps add further configurations that alternately improve either ground- or excited state more strongly. One can avoid this peculiarity by calculating the energy differences as $\Delta E_n = E_{\text{meta}}(4d^{10-(n+1)}4f^{n+1}) - E_{\text{ground}}(4d^{10-n}4f^n)$ for $n \in \{0, 2, \dots\}$. $E_{\text{ground/meta}}(4d^{10-n}4f^n)$ denotes the ground-state's (meta-stable-state's) energy where configurations up to $4d^{10-n}4f^n$ are included. This effectively treats both states on the same level of approximation and therefore leads to error cancellation. Furthermore, it results in a monotonically decreasing energy difference.

Now we include all configurations that involve up to two holes in 4d for the ground-state, as well as all configurations that involve up to three holes in 4d for the meta-stable state and monitor the excitation energy's correction obtained from increasing the one-particle basis as described above. If we assume that the correction on the excitation energy follows a power law decay, we can extrapolate the trend by fitting $\Delta E_k = \Delta E_\infty + \frac{a}{k^p}$ to the data for the energy difference ΔE_k where k denotes the k -th step in the increase of the one-particle basis. We have two fit-parameters a and ΔE_∞ , where the latter is the extrapolated value of the excitation energy. By varying p between one and three, ΔE_∞ assumes values between 202.41 eV and 203.26 eV which agrees well with experiment $\Delta E = 202.2 \pm 1.7$ eV and calculations from different methods [4].

7.2. Binding energies

As mentioned in the beginning of this chapter, Penning trap mass spectroscopy is suited to precisely determine mass differences of atoms, which in the case of neutral ^{163}Ho and ^{163}Dy would be the Q-value, i.e the total energy released by electron capture. However, the atoms in a Penning trap have to be ionized and hence the measured mass difference has to be corrected for the binding energies of the removed electrons of both ions, in order to determine the mass difference of the neutral atoms.

Binding energies can be calculated with the methods described in the previous sections. Here it is demonstrated for the binding energies of $^{187}\text{Re}^{29+}$ and $^{187}\text{Os}^{29+}$, since the mass difference between neutral ^{187}Re and ^{187}Os can be used to benchmark the precision of the experimental apparatus and theoretical methods.

When we determined the excitation energy of meta-stable Re^{29+} , we employed an extrapolation scheme and made use of error cancellation by calculating energy differences. For the binding energies this will be difficult, since dissimilar configurations and different one-particle orbitals are involved in neutral and ionized atoms. However, in the end only the difference in binding energies of Re and Os matters. Here one can make use of error cancellation. The ground-state configurations of neutral Re and Os differ by one electron in 5d. Their one-particle orbitals are very similar. Therefore, one can expect error cancellation in the energy difference ΔE_0 between the ground-states of the two neutral atoms [150]. For ionized Re^{29+} and Os^{29+} the situation is similar. The Os^{29+} ground-state configuration is $[\text{Re}^{29+}]4f^1$ and the single-particle orbitals are similar, too. Thus the calculation of the energy difference ΔE_{29+} of the ionized ground-states likewise benefits from error cancellation. The difference in binding energies is then given as $\Delta B = \Delta E_0 - \Delta E_{29+}$.

In table 7.2 we present the calculated ground-state energies of ionized and neutral atoms as well as the corresponding differences. For these calculations the Block-Lanczos algorithm described in section 3.2 has been used in full analogy to the calculation of the excitation energies in the previous section. Here we restricted the active Hilbert-spaces to configurations that involve at most two holes created on top

highest orbital	$E_{\text{Re}^{29+}}$	$E_{\text{Os}^{29+}}$	ΔE_{29+}
4f	-443.813961	-459.094295	15.280334
5f	-443.830998	-459.115234	15.284236
6f	-443.834915	-459.119847	15.284932
highest orbital	$E_{\text{Re}^{0+}}$	$E_{\text{Os}^{0+}}$	ΔE_0
6d	-454.718824	-459.115234	15.339716
7d	-454.719073	-459.119847	15.339677

Table 7.2.: Ground-state energies of ionized (neutral) Re and Os in keV. Successively higher orbitals have been added to the single particle basis, thereby improving the estimates on the energies.

of the mean-field ground-state configurations. Successively the single particle basis has been increased to include higher orbitals, which are restricted to be populated by at most two electrons. This increase improves the estimate on ground-state energies by shifting them to lower values. These shifts are one order of magnitude larger than the accompanied change in the ground-state-energy-differences ΔE , hence confirming the expected error cancellation discussed above.

The successive corrections to the ground-state energies of the ionized atoms is of the order of 10^0 to 10^1 eV and for ΔE_{29+} of order 10^{-1} to 10^0 eV. For the neutral atoms these are even smaller with a correction on ΔE_0 of $\sim 4 \cdot 10^{-2}$ eV. Thus the binding energy $\Delta B = \Delta E_0 - \Delta E_{29+}$ obtains its largest uncertainty from ΔE_{29+} . To estimate this uncertainty we extrapolate the values of ΔE_{29+} from table 7.2 analogously to the excitation energy from the previous section and subtract them from our best estimate on ΔE_0 given in the last row of the table. This yields binding energies in the range $52.166 \text{ eV} \leq \Delta B \leq 54.709 \text{ eV}$.

We also included static Breit interaction (2.39) to estimate its impact. While it changes the absolute energies significantly, the energy differences are affected to an amount much smaller than the accuracy we could reach with the above procedure. Hence, neglecting Breit interaction is justified a posteriori. It will become important only if errors due to truncations of single-particle basis and restrictions on the many-body configuration space are reduced below 1 eV. However, exact diagonalization using Lanczos' algorithm becomes impractical for that, due to the exponential growth of the Hilbert-space when weakening truncations and restrictions. Other methods like renormalization schemes might be more appropriate.

8. Rotated spherical harmonics

In many textbooks the shape of atomic orbitals is frequently used as argument to explain splitting of degenerate energy levels due to the presence of ligands surrounding a central atom. As Richard E. Powell [151] pointed out, some of those textbooks falsely state that only the sub-space of the three p-orbitals can be spanned by orthonormal basis vectors which have the same shape, but differ in orientation solely. Powell proofed that also the sub-space of the five d-orbitals has this property. In this chapter we present a general proof for sub-spaces of arbitrary orbital angular momentum.

Canonically atomic orbitals are introduced as eigen-functions of angular momentum operator \mathbf{L} which can be expressed as spherical harmonics $\{Y_m^{(l)}\}_{m=-l\dots l}$ for given angular momentum quantum number $l \in \mathbb{N}_0$. These span the irreducible representations of the group of rotations $\text{SO}(3)$ on the Hilbert-space $\mathcal{L}^2(S^2)$ of square integrable functions defined on the sphere. If a Hamiltonian commutes with \mathbf{L} , its eigenvalues are at least $2l + 1$ -fold degenerate and the spherical harmonics $Y_m^{(l)}$ span $2l + 1$ -dimensional invariant sub-spaces for each l . Thus, we have the freedom to choose other basis sets different from $\{Y_m^{(l)}\}_{m=-l\dots l}$.

One possible choice is to linearly combine the complex valued spherical harmonics such that the resulting basis set consists of real valued functions which are called tesseral harmonics and are more suitable for numerical implementations. In figure 8.1 we show these tesseral harmonics in the case of p-orbitals. They already fulfill the desired property of having the same shape and differ in orientation only. Unfortunately this is not the case for the tesseral d-orbitals.

The tesseral p-orbitals in figure 8.1 have been aligned to the diagonals of a cube to show that we can map them onto each other by three-fold rotations around the z-axis. This constitutes the major idea behind the proof in this chapter. If we can construct our $2l + 1$ basis functions in such a way that they are mapped onto each other by $2l + 1$ -fold rotations, we found a basis which fulfills the desired property of having the same shape and differs in orientation only. Therefore, we first construct an abstract representation for the group of $2l + 1$ -fold rotations, also called cyclic group C_{2l+1} , which already fulfills this property, and then we show that this representation is unitarily equivalent to the canonical representation of C_{2l+1} on the basis of spherical harmonics. This will conclude the proof of existence of a set of basis functions of similar shape and we will finish this chapter by giving an algorithm to explicitly calculate the orbitals.

8. Rotated spherical harmonics

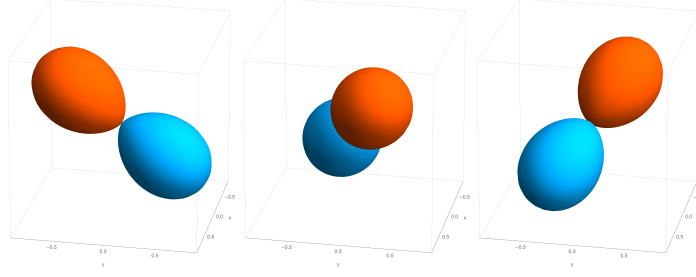


Figure 8.1.: Tesseral harmonics for p-orbitals all have the same shape, but differ in orientation. Colors depict the sign of the orbital. To demonstrate that these tesseral harmonics can be mapped onto each other by three-fold rotations, they have been aligned to the diagonals.

8.1. Proof of existence

We start by constructing an abstract representation of the cyclic group C_{2l+1} where the group acts on the basis vectors by mapping them onto each other.

Definition. Let \mathcal{V} be a vector space of dimension $2l + 1$, where $l \in \mathbb{N}_0$, and $\{e_k^{(l)} \in \mathcal{V} \mid k = 0 \dots 2l\}$ an orthonormal basis. ρ is defined as the linear map $\rho : \mathcal{V} \rightarrow \mathcal{V}$ that permutes the basis vectors as

$$\rho : e_k^{(l)} \mapsto \rho e_k^{(l)} = e_{k+1}^{(l)} \quad \text{where} \quad e_{2l+1}^{(l)} \equiv e_0^{(l)}. \quad (8.1)$$

The n -fold concatenation of ρ is denoted ρ^n and $\rho^0 \equiv \mathbb{1}$ is the identity on \mathcal{V} . As concatenation is associative we can state the following lemma

Lemma 1. $(\{\rho^n\}_{n=0 \dots 2l}, \mathcal{V})$ is a representation of the cyclic group C_{2l+1} .

Proof. It follows by definition that ρ is injective and surjective, hence invertible. Since $\rho^{2l+1} = \mathbb{1} \Rightarrow (\rho^n)^{-1} = \rho^{2l+1-n} \forall n = 0 \dots 2l$, it follows that $\{\rho^n\}_{n=0 \dots 2l}$ forms a group under the operation of concatenation. As this group has the same Cayley table as C_{2l+1} , we conclude that $(\{\rho^n\}_{n=0 \dots 2l}, \mathcal{V})$ is a representation of the cyclic group. \square

Having constructed the above representation of C_{2l+1} it remains to show unitary equivalence to the canonical representation of C_{2l+1} on the space spanned by spherical harmonics $\{Y_m^{(l)}\}_{m=-l \dots l}$. Thus, we will use methods from group theory, namely the calculus with characters [152].

Lemma 2. The characters of $(\{\rho^n\}_{n=0 \dots 2l}, \mathcal{V})$ are

$$\chi_{\mathcal{V}}^{(l)}(\rho^n) = \begin{cases} 0 & n = 1 \dots 2l \\ 2l + 1 & n = 0 \end{cases}. \quad (8.2)$$

Proof.

$$\chi_{\mathcal{V}}^{(l)}(\rho^n) = \sum_{k=0}^{2l} \langle e_k^{(l)} | \rho^n e_k^{(l)} \rangle = \sum_{k=0}^{2l} \langle e_k^{(l)} | e_{k+n}^{(l)} \rangle = (2l + 1) \delta_{n,0} \quad (8.3)$$

□

This leads us to the final theorem

Theorem. Let $\{Y_m^{(l)}\}_{m=-l\dots l}$ denote the irreducible representations of $SO(3)$ on the Hilbert-space of square integrable functions defined on the sphere $\mathcal{L}^2(S^2)$ and $R_z(\frac{2\pi}{2l+1}) \equiv R_z \in SO(3)$ a rotation about the z-axis by $\frac{2\pi}{2l+1}$.

The canonical representation of C_{2l+1} given by $(\{R_z^n\}_{n=0\dots 2l}, \text{span}(Y_m^{(l)}))$ is group-isomorphic to $(\{\rho^n\}_{n=0\dots 2l}, \mathcal{V})$.

Proof.

$$\chi_{\mathcal{L}^2(S^2)}^{(l)}(R_z^n) = \sum_{m=-l}^l \langle Y_m^{(l)} | R_z^n Y_m^{(l)} \rangle = \sum_{m=-l}^l e^{-\frac{2\pi i}{2l+1} n \cdot m} \langle Y_m^{(l)} | Y_m^{(l)} \rangle = (2l+1) \delta_{n,0} \quad (8.4)$$

Comparing this with Lemma 2, we see that both representations have equal characters $\chi_{\mathcal{L}^2(S^2)}^{(l)}(R_z^n) = \chi_{\mathcal{V}}^{(l)}(\rho^n) \forall n$ and hence are group-isomorphic $(\{\rho^n\}_{n=0\dots 2l}, \mathcal{V}) \cong (\{R_z^n\}_{n=0\dots 2l}, \text{span}(Y_m^{(l)}))$. □

As C_{2l+1} is a finite group, every representation is unitary [153]. Hence, the group isomorphic representations from the above theorem are unitarily equivalent.

Corollary. There is a vector $e_0^{(l)} \in \text{span}(Y_m^{(l)})$ such that $e_n^{(l)} \equiv R_z^n e_0^{(l)}$ $n = 0\dots 2l$ is an orthonormal basis of $\text{span}(Y_m^{(l)})$.

This shows that every irreducible representation of $SO(3)$ can be spanned by functions that are similar in shape and differ in orientation only. Since they can be mapped onto each other by rotations around the z-axis, we call them rotated spherical harmonics.

8.2. Construction of rotated spherical harmonics

From the proof of the previous section we can infer an algorithm to directly construct the rotated spherical harmonics for arbitrary l . The basic idea is to find the unitary transformation, which maps the matrix-form of ρ in the basis of $\{e_n^{(l)}\}_{n=0\dots 2l}$ onto the matrix-form of $R_z(\frac{2\pi}{2l+1})$ in the basis of spherical harmonics. As R_z is diagonal in this basis, the unitary transformation can be found by an eigenvalue-decomposition of ρ . Hence, we perform three steps:

1. calculate the matrix representation of ρ (8.1) in the basis of $\{e_n^{(l)}\}_{n=0\dots 2l}$

$$\rho_{nk} = \begin{cases} \delta_{k,2l} & n = 0 \\ \delta_{k+1,n} & \text{otherwise} \end{cases} \quad (8.5)$$

8. Rotated spherical harmonics

2. calculate eigenvalues $\exp\left(-\frac{2\pi i \cdot m}{2l+1}\right)$ of ρ_{nk} and store the corresponding eigenvectors in the columns of matrix U such that

$$\rho_{nk} = \sum_{m=-l}^l U_{nm} \exp\left(-\frac{2\pi i \cdot m}{2l+1}\right) U_{mk}^\dagger \quad (8.6)$$

3. calculate rotated spherical harmonics $\mathcal{R}_n^{(l)}(\theta, \phi)$ via

$$\mathcal{R}_n^{(l)}(\theta, \phi) = \sum_{m=-l}^l U_{nm} Y_m^{(l)}(\theta, \phi) \quad (8.7)$$

This yields complex valued basis functions which are similar in shape, but differ in orientation. To obtain real valued functions with the same property, we define

$$\tilde{U}_{nm} \equiv \begin{cases} \frac{1}{\sqrt{2}} (U_{n,m} + U_{n,-m}) & n = 0, \dots, l \\ \frac{1}{\sqrt{2}} (U_{n,m} - U_{n,-m}) & n = l+1, \dots, 2l \end{cases} \quad (8.8)$$

and use tesseral harmonics $\mathcal{T}_m^{(l)}$ instead of spherical harmonics to construct real valued rotated spherical harmonics

$$\tilde{\mathcal{R}}_n^{(l)}(\theta, \phi) = \sum_{m=-l}^l \tilde{U}_{nm} \mathcal{T}_m^{(l)}(\theta, \phi) \quad (8.9)$$

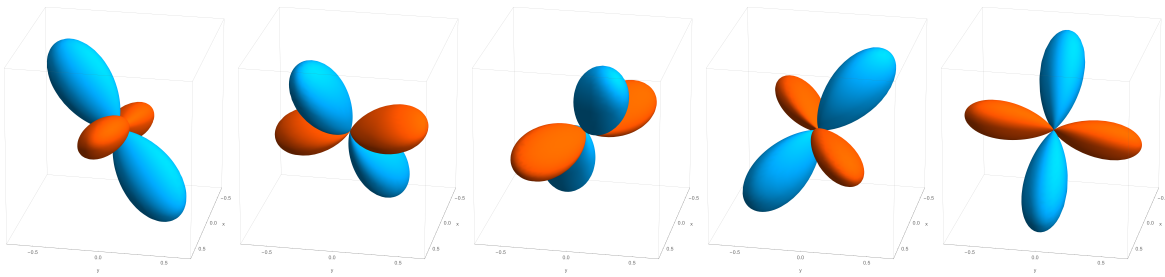
This can be done, since \tilde{U} maps the matrix-form of $R_z\left(\frac{2\pi}{2l+1}\right)$ in the basis of $\mathcal{T}_m^{(l)}$ onto ρ in matrix-form (8.5) via $\tilde{U} \cdot R_z \cdot \tilde{U}^\dagger$. The proof of this directly follows from the definitions of \tilde{U} (8.8) and the tesseral harmonics.

To demonstrate how these real valued rotated spherical harmonics look like, we plotted them for d-, f- and g-orbitals in figure 8.2. For the d-orbitals it is best visible that each of them has the same shape and that each can be mapped onto its right neighbor by a counter-clockwise rotation around the z-axis with angle $\frac{2\pi}{5}$. For f- and g-orbitals perspective distortions make it harder to see that the orbitals actually have the same shape. It is worth noting that applying the above algorithm for p-orbitals, directly results into the p-orbital tesseral harmonics aligned along the diagonals of a cube as shown in figure 8.1.

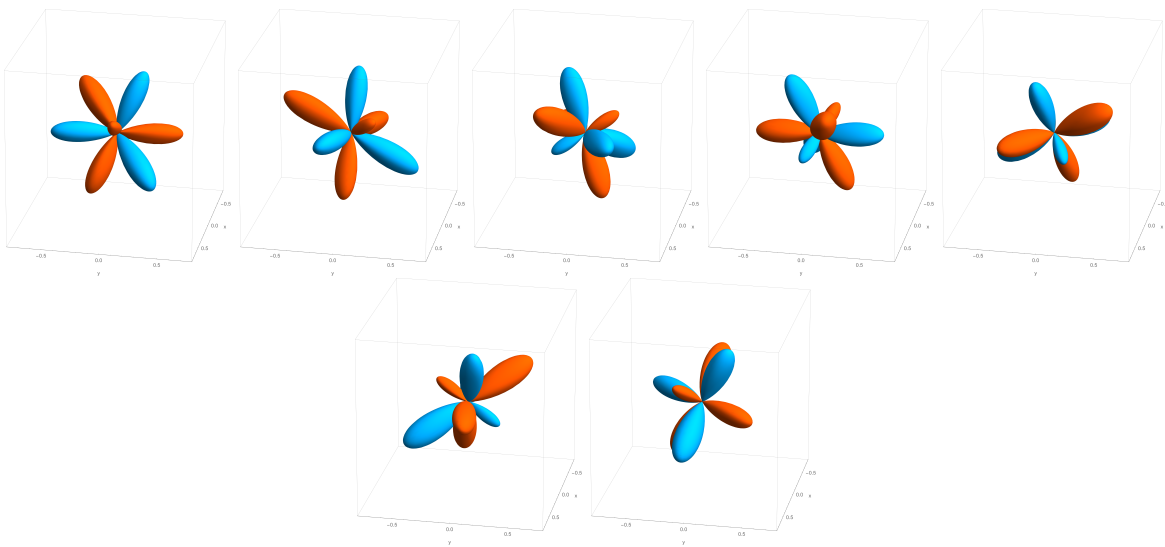
As pointed out in section 6.1, crystal-field splitting of d-orbitals into e_g and t_{2g} irreducible representations of the octahedral symmetry group is often explained by the different shapes of the e_g and t_{2g} orbitals. The shown fact, that all orbitals for a given l can be chosen to have the same shape weakens this explanation. Such an argumentation has to be supplemented by a demonstration that e_g and t_{2g} orbitals cannot have the same shapes as opposed to d-orbitals.

8.2. Construction of rotated spherical harmonics

d-orbitals



f-orbitals



g-orbitals

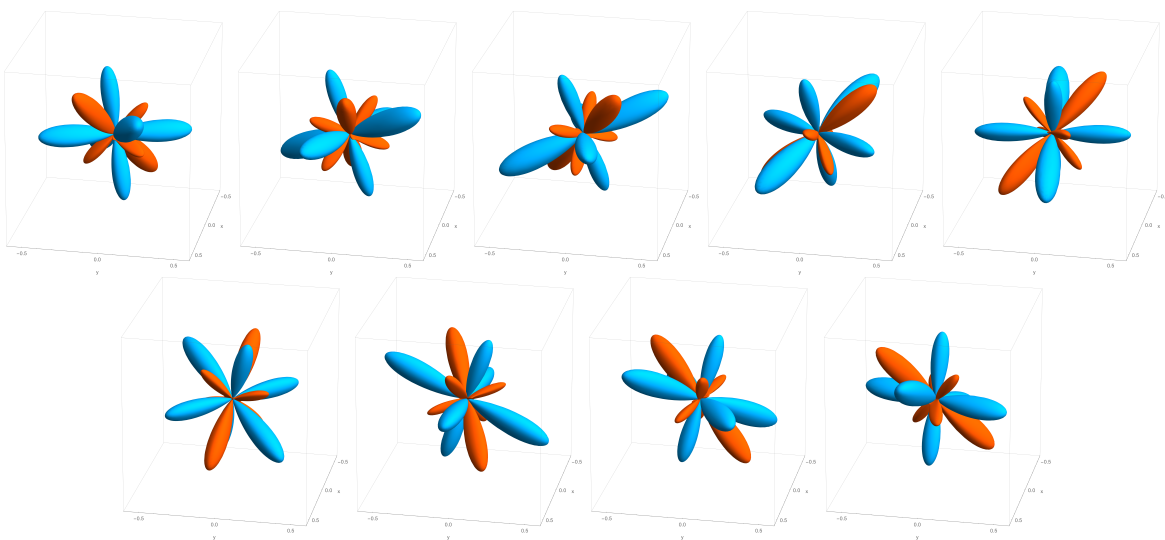


Figure 8.2.: Real valued rotated spherical harmonics for d-, f- and g-orbitals all have the same shape, but differ in orientation.

9. Summary

Our analysis of the electron capture spectrum of ^{163}Ho has shown that the methods described in this work, as well as in our publications [1] and [3], are capable of quantitatively explaining the spectral features observed so far. These include bound-state resonances and energy-dependent line broadening. The former have earlier been studied by different authors with different techniques [62–69], non of which considered multi-configuration states and configuration interaction. With the inclusion of these effects, we were able to determine observed – but so far unexplained – resonances. Starting from first principles, our *ab initio* framework allowed us to identify these resonances as multiplet structures and two-hole states, which result in apparent broadening of one-hole resonances or additional satellite structures. These spectral features emerge from relaxation processes subsequent to the initial electron capture event. Such processes are governed by Coulomb scattering. Coster-Kronig and Super-Coster-Kronig transitions lead to enhanced peaks with two electronic holes in core orbitals. Here the multi-configuration structure of ground- and excited states plays an important role in the determination of peaks' positions and intensities.

These bound-state resonances have first been treated as Lorentzians, which leads to observable deviations from experiment. We concluded that the Lorentzian description is insufficient to explain the spectral shape in energy regions away from resonances and a calculation of line-broadening from first principles is necessary. The latter has been done by including the Auger-Meitner effect leading to coupling between bound resonances and unbound states which have a continuous energy spectrum. This results in line-broadening different from Lorentzians. Fano's effect and energy-dependence of the Auger-Meitner cross-section are responsible for prominent asymmetries of peaks. With this treatment of spectral broadening we were able to reproduce the experimentally observed line-shape close to a resonance as well as away from it. Especially the increased spectral weight on the high energy side of the N_1 (4s) edge and in the endpoint region could be explained by the Auger-Meitner effect. The observed smaller line-width of N_1 (4s) as compared to M_1 (3s) could be attributed to the fact that N_1 is at a lower energy and hence couples to a smaller amount of final Auger-Meitner-states as compared to M_1 .

Although our methods account for all the observed spectral features and even predict further ones, currently hidden due to experimental resolution, some smaller quantitative discrepancies remain. Calculations still miss some broadening of the resonances, which are sharper than in experiment, and have reduced intensity in between the peaks. This indicates that further relaxation channels coupling to continuous energies have to be considered. These include coupling to the electro-magnetic

9. Summary

field leading to relaxation via emission of photons, double Auger-Meitner processes, where two electrons are ejected, and scattering of electrons into bands of the chemical environment, which is gold in the case of the shown experimental data.

Coupling to the electro-magnetic field can be treated in full analogy to the Auger-Meitner effect via introduction of a self-energy. In this case the number of bound electrons is conserved, which makes numerical calculations easier than in the Auger-Meitner case, because calculations already done for the bound states can be reused. However, due to the small Q-value of Ho, decay via photon emission will be small compared to the Auger-Meitner effect. It will become important for other EC isotopes with larger Q-values. Hence, measuring different EC spectra and comparison to theory would not only yield additional tests for our calculations, but would also explore energy-regimes where effects other than the Auger-Meitner process become dominantly responsible for line-broadening. Furthermore, ratios between Auger-Meitner electrons and emitted photons after electron capture in different isotopes are important observables in radio therapy [56–60]. Hence, extension of our methods to calculate these observables would have applications beyond the search for neutrino masses.

Including chemical environment could be done with the help of electronic structure calculations of a Ho atom embedded in a gold crystal. DFT or dynamical mean-field theory (DMFT) may be used as starting point to construct band-structure and single-particle basis for such a system. As Coulomb scattering can transfer electrons from Ho to the Au bands, we expect that this can also be treated in analogy to the Auger-Meitner effect, but with an energy-continuum that is bounded by the bandwidth instead of an unbound continuum. Hence, it will mostly effect the spectral shape in the vicinity of resonances. However, the chemical environment also leads to a Ho valence configuration different from the atomic case we studied in this work. This might open additional Auger-Meitner channels and hence could yield further broadening of resonances and enhanced intensity in their wings.

Coupling to continuous final states does not only yield broadening but also affects positions of resonances. Hence, inclusion of the above effects might also correct the observed differences in calculated and measured peak positions. Additionally increasing single-particle and many-body basis-size will improve accuracy of resonant energies further. Therefore, methods from renormalization should be considered.

Despite these discrepancies, our calculations of the electron capture spectrum including only bound states enabled us to determine the Ho Q-value to be 2838 ± 14 eV. This value has high accuracy and is in good agreement with literature where Q has been determined via Penning-trap mass-spectrometry [5].

For even more accurate future Q-value measurements using highly charged ^{163}Ho and ^{163}Dy ions in a Penning-trap it is necessary to calculate binding energies of the ions. In this work we describe the corresponding calculations and provide estimated atomic binding energies for Re^{29+} and Os^{29+} which can be used to benchmark precision of experiment and theory. In order to provide binding energies for estimation of the ^{163}Ho electron capture Q-value, the presented method can be easily adopted for Ho and Dy with arbitrary ionization.

As a byproduct of the $\text{Re}^{29+}/\text{Os}^{29+}$ studies, experimentalists discovered metastable states with long life-times and measured their excitation energies [4]. We employed the same framework used for the binding energies to compute those excitation energies and we obtained good agreement with experimental data and theoretical calculations from our co-authors.

In order to further improve excitation or binding energies reaching sub eV accuracy, our methods should be combined with renormalization techniques to handle the tremendous growth in the many-body Hilbert-space, which accompanies an increasing precision aim.

Besides electron capture spectroscopy our methods have further applications to x-ray spectroscopy. As we showed in the case of NiO, the Auger-Meitner effect leads to different broadenings of t_{2g} and e_g resonances, thereby affecting their relative intensities. The study of x-ray spectra from solids also guides us in the development of algorithms that combine band-structure calculations with our framework; especially when we want to include the gold environment of Ho in the detectors.

A. Weak interaction on spherical basis

In the following we derive the form of the effective Hamiltonian (2.51) governing weak interaction. We do this in more detail than in literature [93] and hopefully with a clean and comprehensible notation, such that the reader can use the complicated expressions for further calculations. The detailed form of the weak Hamiltonian becomes important when hyper-fine interactions are included to the electron capture spectrum, or when methods developed in this thesis are applied to different electron capture isotopes that decay via higher order forbidden transitions.

As discussed in section 2.2, the weak interaction is mediated by exchange bosons, which are massive in contrast to the photon. This massiveness leads to different interactions especially at low energies, where the mass of the exchange boson dominates all other energy scales. For this regime we obtained an effective current-current interaction with point-like potential $\delta(\mathbf{x}_1 - \mathbf{x}_2)$ leading to the effective weak Hamiltonian (2.23)

$$H_W = \frac{G_W}{\sqrt{2}} \sum_{a=1}^3 U_{ae} \int \bar{\psi}_{\nu_a}(\mathbf{x}) \gamma^\mu (1 - \gamma^5) \psi_e(\mathbf{x}) \bar{\psi}_n(\mathbf{x}) \gamma_\mu (1 - \lambda \gamma^5) \psi_p(\mathbf{x}) d^3x + \text{h.c.} \quad (\text{A.1})$$

Besides the different effective potential, the major differences compared to (2.36) are in the hadronic $J_W^\mu = \psi_n^\dagger \alpha^\mu (1 - \lambda \gamma^5) \psi_p$ and the leptonic current $J_W^\mu = \psi_e^\dagger \alpha^\mu (1 - \gamma^5) \psi_e$. They involve creation of a neutron ψ_n^\dagger (neutrino ψ_ν^\dagger) and annihilation of a proton ψ_p (electron ψ_e). As only left-handed leptons (SU(2)-doublets) couple weakly, the leptonic current contains a projection onto the sub-space of left-handed particles $(1 - \gamma^5)/\sqrt{2}$, where $\gamma^5 = i\gamma^0\gamma^1\gamma^2\gamma^3$. Protons and neutrons are composite particles made of quarks and gluons and hence the strength of vector-coupling is different from axial-coupling which is reflected in the parameter λ [93, 94].

Except for the neutrino created by electron capture almost every particle involved in this decay is in a bound state. Hence, it is convenient to expand the fields ψ on a basis of local orbitals as in (2.25). The radial parts of neutrino wave-functions are given by spherical Bessel-functions, as we treat the neutrino as free particle

$$g_{q,\kappa,a}(r) = \mathcal{N}_a r j_l(qr) \quad (\text{A.2})$$

$$f_{q,\kappa,a}(r) = \mathcal{N}_a \text{sign}(\kappa) \frac{q}{E_q + m} r j_{\bar{l}}(qr) \quad (\text{A.3})$$

$$\mathcal{N}_a = \frac{\sqrt{2}q}{\sqrt{\pi \left[1 + \left(\frac{q}{E_q + m_a} \right)^2 \right]}} \quad E_q = \sqrt{q^2 + m_a^2} \quad (\text{A.4})$$

A. Weak interaction on spherical basis

$j_l(qr)$ denotes the l -th spherical Besselfunction as function of neutrino momentum q and distance from the origin r . E_q is the energy dispersion for a relativistic particle of mass m and the normalization \mathcal{N}_a is chosen such that

$$\int g_{q,\kappa,a}(r)g_{p,\kappa,a}(r) + f_{q,\kappa}(r)f_{p,\kappa}(r)dr = \delta(q - p) \quad . \quad (\text{A.5})$$

The single-particle state of the neutrino is characterized by quantum numbers $\tau_\nu \equiv \{q, \kappa, a, m_{j_z}\}$ and a sum over all quantum numbers $\sum_{\tau_\nu} \equiv \sum_{a=1}^3 \sum_{\kappa_\nu, m_{j_z}} \int_0^\infty q^2 dq$ involves an integral over the neutrino's momentum. In this basis the Hamiltonian reads

$$\begin{aligned} \mathcal{H}_W &= \frac{G_W}{\sqrt{2}} \sum_{\tau_n \tau_p \tau_\nu \tau_e} U_{ae} n_{\tau_n}^\dagger \nu_{\tau_\nu}^\dagger e_{\tau_e} p_{\tau_p} \\ &\int \phi_n^\dagger (1 - \lambda \gamma^5) \phi_p \phi_\nu^\dagger (1 - \gamma^5) \phi_e - \phi_n^\dagger \boldsymbol{\alpha} (1 - \lambda \gamma^5) \phi_p \cdot \phi_\nu^\dagger \boldsymbol{\alpha} (1 - \gamma^5) \phi_e d^3x \\ &+ \text{h.c.} \end{aligned} \quad (\text{A.6})$$

Here, we explicitly evaluated the contraction over the four-index μ in (A.1) such that the Hamiltonian is split into a density-density interaction (first term in the integrand) and a current-current interaction (second term). The hadron density can be expanded on spherical harmonics [93]

$$\phi_n^\dagger (1 - \lambda \gamma^5) \phi_p = \sum_{l=0}^{\infty} \sum_{m=-l}^l (-1)^m \int \phi_n^\dagger Y_l^{-m} (1 - \lambda \gamma^5) \phi_p d\Omega Y_l^m \quad (\text{A.7})$$

where $d\Omega$ denotes the integral over the solid angle. Plugging this into (A.6) the density-density interaction reads

$$\begin{aligned} \mathcal{S}(\tau_n \tau_p \tau_\nu \tau_e) &\equiv \int \phi_n^\dagger (1 - \lambda \gamma^5) \phi_p \phi_\nu^\dagger (1 - \gamma^5) \phi_e d\Omega \\ &= \sum_{l=0}^{\infty} \sum_{m=-l}^l (-1)^m \int \phi_n^\dagger Y_l^{-m} (1 - \lambda \gamma^5) \phi_p d\Omega_{\text{nuc}} \int \phi_\nu^\dagger Y_l^m (1 - \gamma^5) \phi_e d\Omega_{\text{lep}} \quad . \end{aligned} \quad (\text{A.8})$$

Now we can use the definition of the orbital wave-functions (2.31) to write down the densities explicitly

$$\begin{aligned} \int \phi_n^\dagger Y_l^{-m} (1 - \lambda \gamma^5) \phi_p d\Omega_{\text{nuc}} &= g_n g_p \langle \mathcal{Y}_{j_n l_n}^{m_n} | Y_l^{-m} | \mathcal{Y}_{j_p l_p}^{m_p} \rangle \\ &+ f_n f_p \langle \mathcal{Y}_{j_n \bar{l}_n}^{m_n} | Y_l^{-m} | \mathcal{Y}_{j_p \bar{l}_p}^{m_p} \rangle \\ &- i\lambda g_n f_p \langle \mathcal{Y}_{j_n l_n}^{m_n} | Y_l^{-m} | \mathcal{Y}_{j_p \bar{l}_p}^{m_p} \rangle \\ &+ i\lambda f_n g_p \langle \mathcal{Y}_{j_n \bar{l}_n}^{m_n} | Y_l^{-m} | \mathcal{Y}_{j_p l_p}^{m_p} \rangle \\ &= (g_n g_p + f_n f_p) \langle \mathcal{Y}_{j_n l_n}^{m_n} | Y_l^{-m} | \mathcal{Y}_{j_p l_p}^{m_p} \rangle - i\lambda (g_n f_p - f_n g_p) \langle \mathcal{Y}_{j_n l_n}^{m_n} | Y_l^{-m} | \mathcal{Y}_{j_p \bar{l}_p}^{m_p} \rangle \quad . \end{aligned} \quad (\text{A.9})$$

Note that two angular integrals over two spin weighted \mathcal{Y}_{jl}^m and one normal Y_l^{-m} spherical harmonics appear. The first also appears in Coulomb interaction and it assures conservation of parity. The second however mixes the large and small part and will be responsible for parity violation. Both can be simplified using the Wigner-Eckhart theorem [154]

$$\langle \mathcal{Y}_{j_n l_n}^{m_n} | Y_J^{-M} | \mathcal{Y}_{j_p l_p}^{m_p} \rangle = (-1)^{j_n - m_n} \begin{pmatrix} j_n & J & j_p \\ -m_n & -M & m_p \end{pmatrix} \langle \mathcal{Y}_{j_n l_n} || Y_J || \mathcal{Y}_{j_p l_p} \rangle . \quad (\text{A.10})$$

The reduced matrix elements vanish if $l_n + l_p + J$ odd and otherwise read [85]

$$\langle \mathcal{Y}_{j_n l_n} || Y_J || \mathcal{Y}_{j_p l_p} \rangle = (-1)^{j_n + 1/2} \sqrt{(2j_n + 1)(2j_p + 1)} \begin{pmatrix} j_n & j_p & J \\ -1/2 & 1/2 & 0 \end{pmatrix} . \quad (\text{A.11})$$

Completely the same calculations can be applied to the lepton density and the results are plugged into the density-density interaction (A.8)

$$\begin{aligned} \mathcal{S}(\tau_n \tau_p \tau_\nu \tau_e) &= \sum_{JM} (-1)^{j_n - m_n + j_\nu - m_\nu + M} \begin{pmatrix} j_n & J & j_p \\ -m_n & -M & m_p \end{pmatrix} \begin{pmatrix} j_\nu & J & j_e \\ -m_\nu & M & m_e \end{pmatrix} \\ &\times \left[(g_n g_p + f_n f_p) \langle \mathcal{Y}_{j_n l_n} || Y_J || \mathcal{Y}_{j_p l_p} \rangle - i\lambda (g_n f_p - f_n g_p) \langle \mathcal{Y}_{j_n l_n} || Y_J || \mathcal{Y}_{j_p \bar{l}_p} \rangle \right] \\ &\times \left[(g_\nu g_e + f_\nu f_e) \langle \mathcal{Y}_{j_\nu l_\nu} || Y_J || \mathcal{Y}_{j_e l_e} \rangle - i(g_\nu f_e - f_\nu g_e) \langle \mathcal{Y}_{j_\nu l_\nu} || Y_J || \mathcal{Y}_{j_e \bar{l}_e} \rangle \right] . \end{aligned} \quad (\text{A.12})$$

The same shall be done for the current-current interaction in (A.6), but as a current transforms as vector-field under rotations it is much more convenient to expand the currents on a basis of vector spherical harmonics [93] defined by [100]

$$\mathbf{Y}_{JL}^M = \sum_{m=-L}^L \sum_{q=-1}^1 Y_L^m \mathbf{e}_q \langle Lm, 1q | JM \rangle . \quad (\text{A.13})$$

The basis vectors are linear combinations of the standard unit norm vectors in the three spatial dimensions

$$\mathbf{e}_0 = \hat{\mathbf{z}} \quad \mathbf{e}_1 = -(\hat{\mathbf{x}} + i\hat{\mathbf{y}}) / \sqrt{2} \quad \mathbf{e}_{-1} = (\hat{\mathbf{x}} - i\hat{\mathbf{y}}) / \sqrt{2} . \quad (\text{A.14})$$

Thus the hadron current reads

$$\phi_n^\dagger \boldsymbol{\alpha} (1 - \lambda \gamma^5) \phi_p = \sum_{J=0}^{\infty} \sum_{L=J-1}^{J+1} \sum_{M=-J}^J (-1)^M \int \phi_n^\dagger \boldsymbol{\alpha} \cdot \mathbf{Y}_{JL}^{-M} (1 - \lambda \gamma^5) \phi_p d\Omega \mathbf{Y}_{JL}^M \quad (\text{A.15})$$

and the current-current interaction is given by

$$\begin{aligned} \mathcal{V}(\tau_n \tau_p \tau_\nu \tau_e) &\equiv \int \phi_n^\dagger \boldsymbol{\alpha} (1 - \lambda \gamma^5) \phi_p \cdot \phi_\nu^\dagger \boldsymbol{\alpha} (1 - \gamma^5) \phi_e d\Omega \\ &= \sum_{J=0}^{\infty} \sum_{L=J-1}^{J+1} \sum_{M=-J}^J (-1)^M \int \phi_n^\dagger \boldsymbol{\alpha} \cdot \mathbf{Y}_{JL}^{-M} (1 - \lambda \gamma^5) \phi_p d\Omega_{\text{nuc}} \\ &\quad \times \int \phi_\nu^\dagger \boldsymbol{\alpha} \cdot \mathbf{Y}_{JL}^M (1 - \gamma^5) \phi_e d\Omega_{\text{lep}} . \end{aligned} \quad (\text{A.16})$$

A. Weak interaction on spherical basis

Again using the definition of the orbital wave-functions (2.31) and the matrix form of α

$$\alpha = \begin{pmatrix} 0 & \sigma \\ \sigma & 0 \end{pmatrix} \quad (\text{A.17})$$

where σ denote the Pauli-matrices, we obtain an explicit expression of the hadron current

$$\begin{aligned} \int \phi_n^\dagger \alpha \cdot \mathbf{Y}_{JL}^{-M} (1 - \lambda \gamma^5) \phi_p d\Omega_{\text{nuc}} &= -\lambda g_n g_p \langle \mathcal{Y}_{j_n l_n}^{m_n} | \sigma \cdot \mathbf{Y}_{JL}^{-M} | \mathcal{Y}_{j_p l_p}^{m_p} \rangle \\ &- \lambda f_n f_p \langle \mathcal{Y}_{j_n l_n}^{m_n} | \sigma \cdot \mathbf{Y}_{JL}^{-M} | \mathcal{Y}_{j_p l_p}^{m_p} \rangle \\ &+ i g_n f_p \langle \mathcal{Y}_{j_n l_n}^{m_n} | \sigma \cdot \mathbf{Y}_{JL}^{-M} | \mathcal{Y}_{j_p l_p}^{m_p} \rangle \\ &- i f_n g_p \langle \mathcal{Y}_{j_n l_n}^{m_n} | \sigma \cdot \mathbf{Y}_{JL}^{-M} | \mathcal{Y}_{j_p l_p}^{m_p} \rangle . \end{aligned} \quad (\text{A.18})$$

Due to the Clebsch-Gordan coefficients in the definition of the vector spherical harmonics only three types of matrix elements have to be calculated in the above expression, namely [100]

$$\langle \mathcal{Y}_{j_n l_n}^{m_n} | \sigma \cdot \mathbf{Y}_{J, J+1}^{-M} | \mathcal{Y}_{j_p l_p}^{m_p} \rangle = \sqrt{\frac{J+1}{2J+1}} \left(1 + \frac{\kappa_n + \kappa_p}{J+1} \right) \langle \mathcal{Y}_{j_n l_n}^{m_n} | Y_J^{-M} | \mathcal{Y}_{j_p l_p}^{m_p} \rangle \quad (\text{A.19})$$

$$\langle \mathcal{Y}_{j_n l_n}^{m_n} | \sigma \cdot \mathbf{Y}_{J, J}^{-M} | \mathcal{Y}_{j_p l_p}^{m_p} \rangle = \frac{\kappa_n - \kappa_p}{\sqrt{J(J+1)}} \langle \mathcal{Y}_{j_n l_n}^{m_n} | Y_J^{-M} | \mathcal{Y}_{j_p l_p}^{m_p} \rangle \quad (\text{A.20})$$

$$\langle \mathcal{Y}_{j_n l_n}^{m_n} | \sigma \cdot \mathbf{Y}_{J, J-1}^{-M} | \mathcal{Y}_{j_p l_p}^{m_p} \rangle = \sqrt{\frac{J}{2J+1}} \left(-1 + \frac{\kappa_n + \kappa_p}{J} \right) \langle \mathcal{Y}_{j_n l_n}^{m_n} | Y_J^{-M} | \mathcal{Y}_{j_p l_p}^{m_p} \rangle . \quad (\text{A.21})$$

Here we introduced the quantum number κ as defined in section 2.4.1. Plugging these equations into the hadron current one obtains for $L = J + 1$

$$\begin{aligned} \int \phi_n^\dagger \alpha \cdot \mathbf{Y}_{J, J+1}^{-M} (1 - \lambda \gamma^5) \phi_p d\Omega_{\text{nuc}} &= -\lambda g_n g_p \sqrt{\frac{J+1}{2J+1}} \left(1 + \frac{\kappa_n + \kappa_p}{J+1} \right) \langle \mathcal{Y}_{j_n l_n}^{m_n} | Y_J^{-M} | \mathcal{Y}_{j_p l_p}^{m_p} \rangle \\ &- \lambda f_n f_p \sqrt{\frac{J+1}{2J+1}} \left(1 - \frac{\kappa_n + \kappa_p}{J+1} \right) \langle \mathcal{Y}_{j_n l_n}^{m_n} | Y_J^{-M} | \mathcal{Y}_{j_p l_p}^{m_p} \rangle \\ &+ i g_n f_p \sqrt{\frac{J+1}{2J+1}} \left(1 + \frac{\kappa_n - \kappa_p}{J+1} \right) \langle \mathcal{Y}_{j_n l_n}^{m_n} | Y_J^{-M} | \mathcal{Y}_{j_p l_p}^{m_p} \rangle \\ &- i f_n g_p \sqrt{\frac{J+1}{2J+1}} \left(1 + \frac{\kappa_p - \kappa_n}{J+1} \right) \langle \mathcal{Y}_{j_n l_n}^{m_n} | Y_J^{-M} | \mathcal{Y}_{j_p l_p}^{m_p} \rangle \\ &= \sqrt{\frac{J+1}{2J+1}} \left[-\langle \mathcal{Y}_{j_n l_n}^{m_n} | Y_J^{-M} | \mathcal{Y}_{j_p l_p}^{m_p} \rangle \times \lambda \left(g_n g_p \left(1 + \frac{\kappa_n + \kappa_p}{J+1} \right) + f_n f_p \left(1 - \frac{\kappa_n + \kappa_p}{J+1} \right) \right) \right. \\ &\quad \left. + \langle \mathcal{Y}_{j_n l_n}^{m_n} | Y_J^{-M} | \mathcal{Y}_{j_p l_p}^{m_p} \rangle \times i \left(g_n f_p \left(1 + \frac{\kappa_n - \kappa_p}{J+1} \right) - f_n g_p \left(1 + \frac{\kappa_p - \kappa_n}{J+1} \right) \right) \right] . \end{aligned} \quad (\text{A.22})$$

In order to achieve a clean notation and focus on the important parts we introduce the following symbols that include all radial dependencies of the hadron current and are independent of m quantum numbers

$$R_{J,J+1}^1 \equiv -\sqrt{\frac{J+1}{2J+1}}\lambda \left(g_n g_p \left(1 + \frac{\kappa_n + \kappa_p}{J+1} \right) + f_n f_p \left(1 - \frac{\kappa_n + \kappa_p}{J+1} \right) \right) \quad (\text{A.23})$$

$$R_{J,J+1}^2 \equiv \sqrt{\frac{J+1}{2J+1}}i \left(g_n f_p \left(1 + \frac{\kappa_n - \kappa_p}{J+1} \right) - f_n g_p \left(1 + \frac{\kappa_p - \kappa_n}{J+1} \right) \right) . \quad (\text{A.24})$$

For $L = J - 1$ the hadron current has a similar form

$$\begin{aligned} & \int \phi_n^\dagger \boldsymbol{\alpha} \cdot \mathbf{Y}_{J,J-1}^{-M} (1 - \lambda \gamma^5) \phi_p d\Omega_{\text{nuc}} \\ &= \sqrt{\frac{J}{2J+1}} \left[-\langle \mathcal{Y}_{j_n l_n}^{m_n} | Y_J^{-M} | \mathcal{Y}_{j_p l_p}^{m_p} \rangle \lambda \left(g_n g_p \left(1 + \frac{\kappa_n + \kappa_p}{J+1} \right) + f_n f_p \left(-1 - \frac{\kappa_n + \kappa_p}{J} \right) \right) \right. \\ & \quad \left. + \langle \mathcal{Y}_{j_n l_n}^{m_n} | Y_J^{-M} | \mathcal{Y}_{j_p l_p}^{m_p} \rangle i \left(g_n f_p \left(1 + \frac{\kappa_n - \kappa_p}{J+1} \right) - f_n g_p \left(-1 + \frac{\kappa_p - \kappa_n}{J} \right) \right) \right] . \end{aligned}$$

and we again introduce some shorthand notation that covers the radial part of the current

$$\begin{aligned} R_{J,J-1}^1 &\equiv -\lambda \sqrt{\frac{J}{2J+1}} \left(g_n g_p \left(1 + \frac{\kappa_n + \kappa_p}{J+1} \right) + f_n f_p \left(-1 - \frac{\kappa_n + \kappa_p}{J} \right) \right) \\ R_{J,J-1}^2 &\equiv \sqrt{\frac{J}{2J+1}} i \left(g_n f_p \left(1 + \frac{\kappa_n - \kappa_p}{J+1} \right) - f_n g_p \left(-1 + \frac{\kappa_p - \kappa_n}{J} \right) \right) . \end{aligned}$$

Finally for $L = J$ the hadron current reads

$$\begin{aligned} \int \phi_n^\dagger \boldsymbol{\alpha} \cdot \mathbf{Y}_{J,J}^{-M} (1 - \lambda \gamma^5) \phi_p d\Omega_{\text{nuc}} &= \frac{\kappa_p - \kappa_n}{\sqrt{J(J+1)}} \langle \mathcal{Y}_{j_n l_n}^{m_n} | Y_J^{-M} | \mathcal{Y}_{j_p l_p}^{m_p} \rangle \lambda (g_n g_p - f_n f_p) \\ & \quad + \frac{\kappa_n + \kappa_p}{\sqrt{J(J+1)}} \langle \mathcal{Y}_{j_n l_n}^{m_n} | Y_J^{-M} | \mathcal{Y}_{j_p l_p}^{m_p} \rangle i (g_n f_p + f_n g_p) \end{aligned}$$

where we abbreviate

$$R_{J,J}^1 \equiv \frac{\kappa_n + \kappa_p}{\sqrt{J(J+1)}} i (g_n f_p + f_n g_p) \quad (\text{A.25})$$

$$R_{J,J}^2 \equiv \lambda \frac{\kappa_p - \kappa_n}{\sqrt{J(J+1)}} (g_n g_p - f_n f_p) . \quad (\text{A.26})$$

Using the above abbreviations, the hadron current can be expressed as

$$\int \phi_n^\dagger \boldsymbol{\alpha} \cdot \mathbf{Y}_{J,L}^{-M} (1 - \lambda \gamma^5) \phi_p d\Omega_{\text{nuc}} = R_{J,L}^1 \langle \mathcal{Y}_{j_n l_n}^{m_n} | Y_J^{-M} | \mathcal{Y}_{j_p l_p}^{m_p} \rangle + R_{J,L}^2 \langle \mathcal{Y}_{j_n l_n}^{m_n} | Y_J^{-M} | \mathcal{Y}_{j_p l_p}^{m_p} \rangle . \quad (\text{A.27})$$

A. Weak interaction on spherical basis

Here the same angular integrals as in the densities (A.9) appear, such that we can again use the Wigner-Eckhart theorem (A.10) and the reduced matrix elements (A.11) to obtain the current-current interaction

$$\begin{aligned}
\mathcal{V}(\tau_n \tau_p \tau_\nu \tau_e) &= \sum_{J=0}^{\infty} \sum_{L=J-1}^{J+1} \sum_{M=-J}^J (-1)^{j_n - m_n + j_\nu - m_\nu + M} \\
&\times \begin{pmatrix} j_n & J & j_p \\ -m_n & -M & m_p \end{pmatrix} \begin{pmatrix} j_\nu & J & j_e \\ -m_\nu & M & m_e \end{pmatrix} \\
&\times \left[R_{J,L}^1(\tau_n \tau_p) \langle \mathcal{Y}_{j_n l_n} || Y_J || \mathcal{Y}_{j_p \bar{l}_p} \rangle + R_{J,L}^2(\tau_n \tau_p) \langle \mathcal{Y}_{j_n l_n} || Y_J || \mathcal{Y}_{j_p l_p} \rangle \right] \\
&\times \left[R_{J,L}^1(\tau_\nu \tau_e) \langle \mathcal{Y}_{j_\nu l_\nu} || Y_J || \mathcal{Y}_{j_e \bar{l}_e} \rangle + R_{J,L}^2(\tau_\nu \tau_e) \langle \mathcal{Y}_{j_\nu l_\nu} || Y_J || \mathcal{Y}_{j_e l_e} \rangle \right].
\end{aligned} \tag{A.28}$$

The above expression has the same structure as the density-density interaction (A.12). Hence, we introduce one further notation

$$\mathcal{R}_{J,\mu}^1(\tau_n \tau_p, r) \equiv \begin{cases} -i\lambda (g_n(r) f_p(r) - f_n(r) g_p(r)) & \text{if } \mu = 0 \\ R_{J,L}^1(\tau_n \tau_p, r) | L = J + 2 - \mu & \text{if } \mu = 1, 2, 3 \end{cases} \tag{A.29}$$

$$\mathcal{R}_{J,\mu}^2(\tau_n \tau_p, r) \equiv \begin{cases} g_n(r) g_p(r) + f_n(r) f_p(r) & \text{if } \mu = 0 \\ R_{J,L}^2(\tau_n \tau_p, r) | L = J + 2 - \mu & \text{if } \mu = 1, 2, 3 \end{cases} \tag{A.30}$$

which allows us to write the weak-interaction Hamiltonian in compact form

$$\begin{aligned}
\mathcal{H}_W &= \frac{G_W}{\sqrt{2}} \sum_{\tau_n \tau_p \tau_\nu \tau_e} U_{ae} n_{\tau_n}^\dagger \nu_{\tau_\nu}^\dagger e_{\tau_e} p_{\tau_p} \sum_{JM} (-1)^{j_n - m_n + j_\nu - m_\nu + M} \\
&\times \begin{pmatrix} j_n & J & j_p \\ -m_n & -M & m_p \end{pmatrix} \begin{pmatrix} j_\nu & J & j_e \\ -m_\nu & M & m_e \end{pmatrix} \\
&\times \int \left[\mathcal{R}_{J\mu}^1(\tau_n \tau_p, r) \langle \mathcal{Y}_{j_n l_n} || Y_J || \mathcal{Y}_{j_p \bar{l}_p} \rangle + \mathcal{R}_{J\mu}^2(\tau_n \tau_p, r) \langle \mathcal{Y}_{j_n l_n} || Y_J || \mathcal{Y}_{j_p l_p} \rangle \right] \\
&\times \left[\mathcal{R}_J^{1\mu}(\tau_\nu \tau_e, r) \langle \mathcal{Y}_{j_\nu l_\nu} || Y_J || \mathcal{Y}_{j_e \bar{l}_e} \rangle + \mathcal{R}_J^{2\mu}(\tau_\nu \tau_e, r) \langle \mathcal{Y}_{j_\nu l_\nu} || Y_J || \mathcal{Y}_{j_e l_e} \rangle \right] dr.
\end{aligned} \tag{A.31}$$

This is the microscopic Hamiltonian governing weak-interaction between nucleons, electrons and neutrinos. However, For the description of electron capture one needs to consider the full nucleus instead of single nucleons. The nucleons form multiplets of definite total angular momentum I . Now we deduce the Hamiltonian matrix-elements in such a many-nucleon multiplet basis from the microscopic Hamiltonian (A.31).

First we note that creation operators c_{jm}^\dagger are irreducible spherical tensor operators (irreds.) of degree (or rank) j . Therefore, their product can be written as [154]

$$n_{j_n m_n}^\dagger p_{j_p m_p} = (-1)^{j_p - m_p} \sum_{Kq} T_K^q \langle j_n, m_n, j_p, -m_p | Kq \rangle \tag{A.32}$$

$$T_K^q = \sum_{m_1 m_2} (-1)^{j_p - m_2} n_{j_n m_1}^\dagger p_{j_p m_2} \langle j_n, m_1, j_p, -m_2 | Kq \rangle \tag{A.33}$$

where T_q^K is itself an irred. of degree K . Hence, we can apply the Wigner-Eckhart theorem [154] to the following matrix-element

$$\begin{aligned} \langle \psi_{\text{nuc}}^f, I_f, M_{I_f} | n_{j_n m_n}^\dagger p_{j_p m_p} | \psi_{\text{nuc}}^i, I_i, M_{I_i} \rangle &= (-1)^{j_p - m_p + I_f - M_{I_f} + j_n + j_p - J} \sum_{Kq} \quad (\text{A.34}) \\ &\times \begin{pmatrix} I_f & K & I_i \\ -M_{I_f} & q & M_{I_i} \end{pmatrix} \langle K, -q | j_n, -m_n, j_p, m_p \rangle \langle \psi_{\text{nuc}}^f, I_f || T_K(j_n, j_p) || \psi_{\text{nuc}}^i, I_i \rangle . \end{aligned}$$

Here $|\psi_{\text{nuc}}^i, I_i, M_{I_i}\rangle$ and $|\psi_{\text{nuc}}^f, I_f, M_{I_f}\rangle$ denote initial and final nuclear states with total angular momentum I . The fact that Wigner 3-j symbols are related to Clebsch-Gordan coefficients via [155]

$$\begin{pmatrix} j_n & J & j_p \\ -m_n & -M & m_p \end{pmatrix} = \frac{(-1)^{J+M+2j_p}}{\sqrt{2J+1}} \langle j_n, -m_n, j_p, m_p | JM \rangle \quad (\text{A.35})$$

can be used to simplify the Hamiltonian by exploiting the orthogonality relation of Clebsch-Gordan coefficients [154]

$$\sum_{m_n m_p} \langle K, -q | j_n, -m_n, j_p, m_p \rangle \langle j_n, -m_n, j_p, m_p | JM \rangle = \delta_{KJ} \delta_{-q, M} . \quad (\text{A.36})$$

To evaluate the sum over m_n, m_p and use the above orthogonality relation, we have to also use $(-1)^{m_n + m_p} = (-1)^M$. We insert unity $\mathbb{1} = \mathbb{1}_{\text{lep}} \otimes \sum_{\psi_{\text{nuc}}^f} |\psi_{\text{nuc}}^f, I, M\rangle \langle \psi_{\text{nuc}}^f, I, M|$ twice in the microscopic Hamiltonian (A.31), where $\sum_{\psi_{\text{nuc}}^f} \equiv \sum_{\psi_{\text{nuc}}^f, I_f, M_{I_f}}$ abbreviates the sum over all quantum numbers characterizing the nuclear many-body state and $\mathbb{1}_{\text{lep}}$ is the identity on the leptonic Fock-space. Using further (A.34) and (A.35) leads to

$$\begin{aligned} \mathcal{H}_W &= \frac{G_W}{\sqrt{2}} \sum_{\tau_\nu \tau_e} U_{ae} \sum_{\psi_{\text{nuc}}^i, \psi_{\text{nuc}}^f} \sum_{JM} \frac{(-1)^{j_\nu - m_\nu + I_f - M_{I_f} + M}}{\sqrt{2J+1}} \\ &\times \begin{pmatrix} I_f & J & I_i \\ -M_{I_f} & -M & M_{I_i} \end{pmatrix} \begin{pmatrix} j_\nu & J & j_e \\ -m_\nu & M & m_e \end{pmatrix} \\ &\times \int \sum_{\tau_n \tau_p} \left[\mathcal{R}_{J\mu}^1(\tau_n \tau_p, r) \langle \mathcal{Y}_{j_n l_n} || Y_J || \mathcal{Y}_{j_p \bar{l}_p} \rangle + \mathcal{R}_{J\mu}^2(\tau_n \tau_p, r) \langle \mathcal{Y}_{j_n l_n} || Y_J || \mathcal{Y}_{j_p l_p} \rangle \right] \\ &\times \langle \psi_{\text{nuc}}^f, I_f || T_J(j_n, j_p) || \psi_{\text{nuc}}^i, I_i \rangle \\ &\times \left[\mathcal{R}_J^{1\mu}(\tau_\nu \tau_e, r) \langle \mathcal{Y}_{j_\nu l_\nu} || Y_J || \mathcal{Y}_{j_e \bar{l}_e} \rangle + \mathcal{R}_J^{2\mu}(\tau_\nu \tau_e, r) \langle \mathcal{Y}_{j_\nu l_\nu} || Y_J || \mathcal{Y}_{j_e l_e} \rangle \right] \text{dr} \\ &\times v_{\tau_\nu}^\dagger e_{\tau_e} \otimes |\psi_{\text{nuc}}^f, I_f, M_f\rangle \langle \psi_{\text{nuc}}^i, I_i, M_i| . \quad (\text{A.37}) \end{aligned}$$

In order to simplify notation we introduce a nuclear form factor

$$\begin{aligned} \mathcal{N}_{J\mu}^{I_i I_f}(r) &\equiv \sum_{\tau_n \tau_p} \left[\mathcal{R}_{J\mu}^1(\tau_n \tau_p, r) \langle \mathcal{Y}_{j_n l_n} || Y_J || \mathcal{Y}_{j_p \bar{l}_p} \rangle + \mathcal{R}_{J\mu}^2(\tau_n \tau_p, r) \langle \mathcal{Y}_{j_n l_n} || Y_J || \mathcal{Y}_{j_p l_p} \rangle \right] \\ &\times \langle \psi_{\text{nuc}}^f, I_f || T_K(j_n, j_p) || \psi_{\text{nuc}}^i, I_i \rangle \quad (\text{A.38}) \end{aligned}$$

A. Weak interaction on spherical basis

and define

$$p_J^{I_i I_f}(\tau_\nu, \tau_e) \equiv \frac{G_W}{\sqrt{2(2J+1)}} \int \mathcal{N}_{J\mu}^{I_i I_f}(r) \left[\mathcal{R}_J^{1\mu}(\tau_\nu \tau_e, r) \langle \mathcal{Y}_{j_\nu l_\nu} || Y_J || \mathcal{Y}_{j_e l_e} \rangle \right. \\ \left. + \mathcal{R}_J^{2\mu}(\tau_\nu \tau_e, r) \langle \mathcal{Y}_{j_\nu l_\nu} || Y_J || \mathcal{Y}_{j_e l_e} \rangle \right] \mathbf{d}r . \quad (\text{A.39})$$

With the above abbreviations the Hamiltonian is most compactly written as

$$\mathcal{H}_W = \sum_{\tau_\nu, \tau_e} U_{ae} \sum_{\psi_{\text{nuc}}^i, \psi_{\text{nuc}}^f} \sum_{JM} (-1)^{j_\nu - m_\nu + I_f - M_{I_f} + M} \\ \times \begin{pmatrix} I_f & J & I_i \\ -M_{I_f} & -M & M_{I_i} \end{pmatrix} \begin{pmatrix} j_\nu & J & j_e \\ -m_\nu & M & m_e \end{pmatrix} \\ \times p_J^{I_i I_f}(\tau_\nu, \tau_e) v_{\tau_\nu}^\dagger e_{\tau_e} \otimes |\psi_{\text{nuc}}^f, I_f, M_f\rangle \langle \psi_{\text{nuc}}^i, I_i, M_i| . \quad (\text{A.40})$$

This is form (2.51) and hence our derivation is finished.

B. List of publications

- [1] ***Ab initio* calculation of the calorimetric electron capture spectrum of ^{163}Ho : Intra-atomic decay into bound-states**, M. Braß, C. Enss, L. Gastaldo, R. J. Green and M. W. Haverkort, Phys. Rev. C 97, 054620 (2018)

As principal author I contributed to this publication by performing all calculations and producing plots and tables. This involved implementing algorithms to calculate the Hamiltonian on an atomic basis as described in section 2.4 and furthermore, application of methods detailed in chapter 3.

- [2] **High-resolution and low-background ^{163}Ho spectrum: interpretation of the resonance tails**, C. Velte, F. Ahrens, A. Barth, K. Blaum, M. Braß, M. Door, H. Dorrer, Ch. E. Dllmann, S. Eliseev, C. Enss, P. Filianin, A. Fleischmann, L. Gastaldo, A. Goeggelmann, T. Day Goodacre, M. W. Haverkort, D. Hengstler, J. Jochum, K. Johnston, M. Keller, S. Kempf, T. Kieck, C. M. Knig, U. Kster, K. Kromer, F. Mantegazzini, B. Marsh, Yu. N. Novikov, F. Piquemal, C. Riccio, D. Richter, A. Rischka, S. Rothe, R. X. Schssler, Ch. Schweiger, T. Stora, M. Wegner, K. Wendt, M. Zampaolo and K. Zuber, Eur. Phys. J. C 79: 1026 (2019)

As co-author I contributed to this publication by providing the calculation of the EC spectrum with lorentzian broadening as described in chapter 4. Furthermore, I performed the Bayesian analysis to determine the Q-value.

- [3] **Ab initio calculation of the electron capture spectrum of ^{163}Ho : Auger-Meitner decay into continuum states**, M. Braß and M. W. Haverkort, New J. Phys. 22, 093018 (2020)

As principal author I contributed to this publication by developing algorithms to determine energy dependent line-broadening due to the Auger-Meitner effect as described in chapter 5. I performed all calculations and produced all plots.

- [4] **Detection of metastable electronic states by Penning trap mass spectrometry**, R. X. Schüßler, H. Bekker, M. Braß, H. Cakir, J. R. Crespo López-Urrutia, M. Door, P. Filianin, Z. Harman, M. W. Haverkort, W. J. Huang, P. Indelicato, C. H. Keitel, C. M. König, K. Kromer, M. Müller, Y. N. Novikov, A. Rischka, C. Schweiger, S. Sturm, S. Ulmer, S. Eliseev and K. Blaum, Nature Vol. 581, 42 (2020)

As co-author my contribution to this publication has been the calculation of the corresponding excitation energies in Quanyt and the development of an extrapolation algorithm to increase accuracy and determine uncertainties, which is described in section 7.1.

Bibliography

- [1] M. Braß, C. Enss, L. Gastaldo, R. J. Green and M. W. Haverkort, *Phys. Rev. C* **97**, 054620 (2018)
- [2] C. Velte et al., *Eur. Phys. J. C* **79**, 1026 (2019)
- [3] M. Braß and M. W. Haverkort, *New J. Phys.* **22**, 093018 (2020)
- [4] R. X. Schüßler et al., *Nature* Vol. 581, 42 (2020)
- [5] S. Eliseev et al., *Phys. Rev. Lett.* **115**, 062501 (2015)
- [6] J. Chadwick, *Verhandl. Dtsch. Phys. Ges.* **16**, 383 (1914)
- [7] C.S. Wu "History of Beta Decay", in: "Beitrge zur Physik und Chemie des 20. Jahrhunderts" (O. R. Frisch, F. A. Paneth, F. Laves, P. Rosbaud, eds.), Vieweg+Teubner Verlag, Wiesbaden (1959)
- [8] E. Fermi, *Zeitschrift f. Phys.* **88**, 161 (1934)
- [9] Ch. Kraus et al., *Eur. Phys. J. C* **40**, 447 (2005)
- [10] V. N. Aseev et al., *Phys. Rev. D* **84**, 112003 (2011)
- [11] M. Aker et al. (KATRIN collaboration), *Eur. Phys. J. C* **80**, 264 (2020)
- [12] A. A. Esfahani et al. (Project 8 collaboration), *Journal of Physics G: Nuclear and Particle Physics* , **44**, 5, 054004 (2017)
- [13] B. Alpert et al. (HOLMES collaboration), *Eur. Phys. J. C*, **75**, 112 (2015)
- [14] L. Gastaldo et al. (ECHO collaboration), *Eur. Phys. J. Special Topics* **226**, 1623 (2017)
- [15] M. P. Croce et al. (NuMECS collaboration), *Journal of Low Temperature Physics* **184**, 938 (2016)
- [16] C. L. Cowan et al., *Science* Vol. 124, 3212, 103 (1956)
- [17] G. C. Wick, "Sulle Propriet della Materia Nucleare", *Nuovo Cim* **11**, 227 (1934)
- [18] L. W. Alvarez, *Phys. Rev.* **52**, 134 (1937)
- [19] P. A. M. Dirac, *Proceedings of the Royal Society A.* **114**, 243 (1927)

BIBLIOGRAPHY

- [20] E. Majorana, "Teoria simmetrica dellelettrone e del positrone", Nuovo Cim 14, 171 (1937)
- [21] Y. Gando et al. (Kamland-Zen Collaboration), PoS NOW2018, 068 (2018)
- [22] D.Q. Adams et al. (CUORE Collaboration), Phys. Rev. Lett. 124, 122501 (2020)
- [23] M. Agostini et al., J. Phys.: Conf. Ser. 1342, 012005 (2020)
- [24] G. Cao et al. (EXO-200 and nEXO Collaborations), PoS HQL2018, 054 (2018)
- [25] G. Danby et al., Phys. Rev. Lett. Vol. 9, 1, 36 (1962)
- [26] B. Pontecorvo, Sov. Phys. JETP, Vol. 26, 5, 984 (1968)
- [27] R. Davis, Jr., D. S. Harmer and K. C. Hoffman, Phys. Rev. Lett. 20, 1205 (1968)
- [28] Q. R. Ahmad et al., (SNO Collaboration), Phys. Rev. Lett. 87, 071301 (2001)
- [29] Y. Fukuda et al. (Super-Kamiokande Collaboration), Phys. Rev. Lett. 81, 1562 (1998)
- [30] Y. Abe et al. (Double Chooz Collaboration), Phys. Rev. Lett. 108, 131801 (2012)
- [31] F. P. An et al., Phys. Rev. Lett. 108, 171803 (2012)
- [32] G. Mention et al., Phys. Rev. D 83, 073006 (2011)
- [33] W. Hampel et al. (GALLEX Collaboration) Physics Letters B 420, 114 (1998)
- [34] J. N. Abdurashitov et al. (SAGE Collaboration), Phys. Rev. C 59, 2246 (1999)
- [35] C. Giunti and M. Laveder, Phys. Rev. C 83, 065504 (2011)
- [36] A. Aguilar et al. (LSND Collaboration), Phys. Rev. D 64, 112007 (2001)
- [37] A. A. Aguilar-Arevalo et al. (MiniBooNE Collaboration), Phys. Rev. Lett. 110, 161801 (2013)
- [38] A. A. Aguilar-Arevalo et al. (MiniBooNE Collaboration), Phys. Rev. Lett. 121, 221801 (2018)
- [39] M. Maltoni and T. Schwetz, Phys. Rev. D 76, 093005 (2007)
- [40] C. Giunti and E. M. Zavanin, Modern Physics Letters A, Vol. 31, 1, 1650003 (2016)
- [41] J. Kostensalo, J. Suhonen, C. Giunti and P.C. Srivastava, Physics Letters B 759, 542 (2019)
- [42] L. Hayen, J. Kostensalo, N. Severijns and J. Suhonen Phys. Rev. C 100, 054323 (2019)

- [43] C. Velte, "Measurement of a high energy resolution and high statistics ^{163}Ho electron capture spectrum for the ECHo experiment", Dissertation, Ruperto-Carola-University of Heidelberg (2019)
- [44] S. Hannesta, *Progress in Particle and Nuclear Physics* 65, 185 (2010)
- [45] J. Lesgourgues and S. Pastor, *Physics Reports* 429, 307 (2006)
- [46] S. R. Choudhury and S. Hannestad, arXiv:1907.12598 (2019)
- [47] F. T. Avignone III, S. R. Elliott and J. Engel, *Rev. Mod. Phys.* 80, 481 (2008)
- [48] Z. Maki, M. Nakagawa, S. Sakata, *Progress of Theoretical Physics* 28, 5, 870 (1962)
- [49] H.V. Klapdor-Kleingrothaus, *Eur. Phys. J. A* 12, 147154 (2001)
- [50] F. Capozzi et al., *Phys. Rev. D* 95, 096014 (2017)
- [51] J. F. Beacom, R. N. Boyd and A. Mezzacappa, *Phys. Rev. Lett.* 85, 17, 3568 (2000)
- [52] J. F. Beacom, R. N. Boyd and A. Mezzacappa, *Phys. Rev. D* 63, 073011 (2001)
- [53] J. Jia, Y. Wang and S. Zhou, *Chinese Physics C* 43, 9, 095102 (2019)
- [54] A. I. Kassis, *International Journal of Radiation Biology* 80, 11-12, 789 (2004)
- [55] B. Cornelissen and K. A. Vallis, *Current Drug Discovery Technologies* 7, 263 (2010)
- [56] A. A. S. Tavares and J. M. R. S. Tavares, *International Journal of Radiation Biology* 86, 4, 261 (2010)
- [57] F. Buchegger et al., *European Journal of Nuclear Medicine and Molecular Imaging* 33, 1352 (2006)
- [58] B. Q. Lee et al., *Computational and Mathematical Methods in Medicine* 2012, 651475 (2012)
- [59] B. Q. Lee et al., *International Journal of Radiation Biology* 92, 11, 641 (2016)
- [60] N. Falzone et al., *Phys. Med. Biol.* 62, 2239 (2017)
- [61] A. De Rújula, *Nucl. Phys. B* 188, 3, 414 (1981)
- [62] A. De Rújula and M. Lusignoli, *Physics Letters B* 188, 4-6, 429 (1982)
- [63] A. De Rújula and M. Lusignoli, arXiv:1510.05462
- [64] A. De Rújula and M. Lusignoli, *JHEP* 05, 015 (2016)

BIBLIOGRAPHY

- [65] A. Faessler et al., *J. of Phys. G: Nuclear and Particle Physics* 42, 1, 015108 (2014)
- [66] A. Faessler and F. Šimkovic, *Phys. Rev. C* 91, 045505 (2015)
- [67] A. Faessler et al., *Phys. Rev. C* 91, 064302 (2015)
- [68] A. Faessler, L. Gastaldo, F. Šimkovic, *Phys. Rev. C* 95, 045502 (2017)
- [69] R. G. H. Robertson, *Phys. Rev. C* 91, 035504 (2015)
- [70] T. A. Carlson and C. W. Nestor, *Phys. Rev. A* 8, 2887 (1973)
- [71] M. E. Peskin, D. V. Schroeder, "An introduction to quantum field theory", Westview Press, (2016)
- [72] Yorikiyo Nagashima, "Elementary Particle Physics, Volume 2: Foundations of the Standard Model", 1st Edition, WILEY-VCH Verlag GmbH & Co. KGaA. (2013)
- [73] C. Giunti, C. W. Kim and U. W. Lee, *Phys. Rev. D* 45, 7, 2414 (1992)
- [74] A. L. Fetter, J. D. Walecka, "Quantum theory of many-particle systems", Dover Publ. (2003)
- [75] F. Schwabl, "Quantenmechanik für Fortgeschrittene", Springer Berlin Heidelberg (2008)
- [76] P. Hohenberg and W. Kohn, *Phys. Rev.* 136, B864 (1964)
- [77] M. Levy, *Proc. Natl. Acad. Sci. USA* 76, 12, 6062 (1979)
- [78] J. P. Perdew and Y. Wang, *Phys. Rev. B* 45, 23, 13 244 (1992)
- [79] X. Blase, "Introduction to Density Functional Theory" in: "Many-Body Methods for Real Materials Modeling and Simulation"(E. Pavarini, E. Koch and S. Zhang, eds.), Vol. 9, Verlag des Forschungszentrum Jülich (2019), ch. 1
- [80] W. Kohn and L. J. Sham, *Phys. Rev.* 140, A1133 (1965)
- [81] K. Koepernik and H. Eschrig, *Phys. Rev. B* 59, 1743 (1999)
- [82] I. Opahle, K. Koepernik and H. Eschrig, *Phys. Rev. B* 60, 14035 (1999)
- [83] H. Eschrig, M. Richter and I. Opahle, *Theoretical and Computational Chemistry* (2004), p. 723
- [84] G. Breit, *Phys. Rev.* 34, 553 (1929)
- [85] W.R. Johnson, K.T. Cheng and M.H. Chen, *Theoretical and Computational Chemistry* 14, 120 (2004)

- [86] E. P. Wigner "On the Matrices Which Reduce the Kronecker Products of Representations of S. R. Groups", in: "Quantum Theory of Angular Momentum" (L. C. Biedenharn and H. van Dam, eds.), Academic Press, New York (1965), pp.87-133
- [87] E. W. Weisstein, "Wigner 3j-Symbol." From MathWorld—A Wolfram Web Resource. <https://mathworld.wolfram.com/Wigner3j-Symbol.html>
- [88] D. V. Griffiths and I. M Smith, "Numerical methods for engineers: a programming approach", Boca Raton: CRC Press (1991)
- [89] Y. Qiu and C. F. Fischer, J. Comp. Phys. 156, 257271 (1999)
- [90] M. Tanabashi et al. (Particle Data Group), Phys. Rev. D 98, 030001 (2018)
- [91] I. Angeli and K. P. Marinova, Atomic Data and Nuclear Data Tables 99, 1, 69 (2013)
- [92] I. Esteban, et al., J. High Energ. Phys. 2017, 87 (2017)
- [93] W. Bambynek et al., Rev. Mod. Phys. 49, 1, 77 (1977)
- [94] A. Kropf and H. Paul, Z. Physik 267, 129 (1974)
- [95] R. Casalbuoni, "The Standard Model of Electroweak Interactions", lecture notes, Università di Firenze, lectures given at the Otranto School, September 1997
- [96] S. Bilenky, "Introduction to the Physics of Massive and Mixed Neutrinos", Lecture Notes in Physics 817, Springer Heidelberg Dordrecht London New York (2010)
- [97] Z. Maki, M. Nakagawa, S. Sakata, Progress of Theoretical Physics 28, 5, 870 (1962)
- [98] S. Fukuda et al. (Super-Kamiokande Collaboration), Phys. Rev. Lett. 86, 5656 (2001)
- [99] J. Cullum, R. A. Willoughby, Journal of Computational and Applied Mathematics 12&13, 37 (1985)
- [100] W. R. Johnson, S. A. Blundell, and J. Sapirstein, Phys. Rev. A 37, 8, 2764 (1988)
- [101] Y. Saad, J. R. Chelikowsky and S. M. Shontz, Siam Rev. 52, 1, 3 (2010)
- [102] I. Shavitt "The Method of Configuration Interaction", in: "Methods of Electronic Structure Theory" (H. f. Schaefer III, ed.), Modern Theoretical Chemistry Vol. 3, Springer Science + Business Media New York, (1977), pp. 189-275
- [103] R. K. Nesbet, Phys. Rev. 155, 51 (1967)
- [104] R. K. Nesbet, Phys. Rev. A 2, 661 (1970)

BIBLIOGRAPHY

- [105] K. Lánczos, *Journal of Research of the National Bureau of Standards* 45, 4, 255 (1950)
- [106] R. G. Grimes, J. G. Lewis, and H. D. Simon, *Siam J. Matrix Anal. Appl.* 15, 1, 228 (1994)
- [107] M. W. Haverkort et al., *Europhys. Lett.* 108, 57004 (2014)
- [108] M. W. Haverkort, *J. Phys.: Conf. Ser.* 712, 012001 (2016)
- [109] One can download the code and find documentation at <http://www.Quanty.org>
- [110] M. W. Haverkort, private communication
- [111] E. Koch, "Exact Diagonalization and Lanczos Method" in: "Many-Body Methods for Real Materials Modeling and Simulation" (E. Pavarini, E. Koch and S. Zhang, eds.), Vol. 9, Verlag des Forschungszentrum Jülich (2019), ch. 7
- [112] G.D. Mahan, *Phys. Rev.* 163, 612 (1967)
- [113] S. B. Crampton, D. Kleppner and N. F. Ramsey, *Phys. Rev. Lett.* 11, 338 (1963)
- [114] M. Merstorf, M. Braß and M. W. Haverkort, publication in preparation, will be made available on arxiv.org
- [115] L. Meitner "Über die Entstehung der β -Strahl-Spektren radioaktiver Substanzen", *Z. Phys.* 9, 1, 131 (1922)
- [116] P. Auger "Sur les rayons secondaires produits dans un gaz par des rayons X", *C.R.A.S.* 177, 169 (1923)
- [117] H. Weyl, *Math. Ann.* 68, 220 (1910)
- [118] O.A. Rubtsova, V.I. Kukulín and V.N. Pomerantsev, *Ann. Phys.* 360, 613 (2015)
- [119] Commandant Benoît "Note sur une méthode de résolution des équations normales provenant de l'application de la méthode des moindres carrés à un système d'équations linéaires en nombre inférieure celui des inconnues. Application de la méthode à la résolution d'un système défini d'équations linéaires (procédé du Commandant Cholesky)." *Bulletin géodésique* 2, 67 (1924)
- [120] U. Fano, *Phys. Rev.* 124, 1866 (1961)
- [121] L. G. Parratt, *Rev Mod Phys* 31, 3, 616 (1959)
- [122] J. Yano and V. K. Yachandra, *Photosynth. Res.* 102, 241 (2009)
- [123] J. J. Rehr, *Radiation Physics and Chemistry* 75, 1547 (2006)

- [124] M. Siegbahn and T. Magnusson, *Nature* 132, 895 (1933)
- [125] M. Siegbahn and T. Magnusson, *Nature* 133, 257(1934)
- [126] H. M. O'Bryan and H. W. B. Skinner, *Phys. Rev.* 45, 370 (1934)
- [127] G. S. Henderson, F. M.F. de Groot and B. J.A. Moulton, *Reviews in Mineralogy and Geochemistry* 78, 1, 75 (2014)
- [128] E. A. Stern, *Phys. Rev. B* 10, 3027 (1974)
- [129] E. Pavarini, "Crystal-Field Theory, Tight-Binding Method and Jahn-Teller Effect" in: "Correlated Electrons: From Models to Materials Modeling and Simulation"(E. Pavarini, E. Koch, F. Anders, and M. Jarrell, eds.), Vol. 2, Verlag des Forschungszentrum Jlich (2012), ch. 6
- [130] L. H. Gade "Koordinationschemie" Wiley-VCH (19XX), ch. 4, pp. 190-193
- [131] K. S. Kim, *Chemical Physics Letters* 26, 2, 234 (1974)
- [132] D. Alders et al., *Phys. Rev. B* 57, 11623 (1998)
- [133] H. Yavaş et al., *J. Phys. Condens. Matter* 22, 485601 (2010)
- [134] L. Braicovich et al., *Phys. Rev. Lett.* 104, 077002 (2010)
- [135] J. N. Hancock et al., *Phys. Rev. B* 80, 092509 (2009)
- [136] C.-C. Kao, W. A. L. Caliebe, J. B. Hastings and J.-M. Gillet, *Phys. Rev. B* 54, 16361 (1996)
- [137] R. S. Markiewicz, M. Z. Hasan and A. Bansil, *Phys. Rev. B* 77, 094518 (2008)
- [138] V. Krewald et al., *Chem. Sci.* 6, 1676 (2015)
- [139] Jue Wu, Yong Yang and Wanli Yang, *Dalton Trans.* 49, 13519 (2020)
- [140] C. L. Chen et al., *Supercond. Sci. Technol.* 24, 115007 (2011)
- [141] L. J. P. Ament et al., *Rev. Mod. Phys.* 83, 705 (2011)
- [142] H. A. Kramers, W. Heisenberg, *Z. Physik* 31, 681 (1925)
- [143] A. Georges, G. Kotliar, W. Krauth and M. J. Rozenberg, *Rev. Mod. Phys.* 68, 1, 13 (1996)
- [144] D. Vollhardt, *Ann. Phys.* 524, 1, 1 (2012)
- [145] P. W. Anderson, *Phys. Rev.* 124, 41 (1961)

BIBLIOGRAPHY

- [146] Y. Lu, M. Höppner, O. Gunnarsson and M. W. Haverkort, *Phys. Rev. B*, 90, 085102 (2014)
- [147] J. Repp et al., *Appl. Phys. B* 107, 983 (2012).
- [148] C. Roux et al., *Appl. Phys. B* 107, 997 (2012).
- [149] M.G. Kozlov, M.S. Safronova, J.R. Crespo López-Urrutia and P.O. Schmidt *Rev. Mod. Phys.* 90, 045005 (2018)
- [150] Z. Harman, private communication
- [151] R. E. Powell, *Journal of Chemical Education* 45, 1, 45 (1968)
- [152] W. Fulton and J. Harris "Representation Theory", Springer (2004)
- [153] J. Walcher, "Lie-Gruppen und Darstellungstheorie", lecture notes, University of Heidelberg, lectures given in winter term 2015/16
- [154] S. Scherer "Symmetrien und Gruppen in der Teilchenphysik", Springer Spektrum (2016), ch. 4, pp. 139-189
- [155] R. Shaw "Wigner 3j-symbols and the Lorentz group", in: "Group Theoretical Methods in Physics" (A. Janner, T. Janssen, M. Boon, eds.), Lecture Notes in Physics, vol 50. Springer, Berlin, Heidelberg (1976)

Acknowledgements

I would like to thank all those people who supported me during my doctoral studies and enriched these four years with exciting discussions, by sharing their knowledge and most important with their company.

Dear Maurits Haverkort, thank you for all your input and ideas that made me think in ways different from what I had been taught before. Your intuitive view on solutions to physical problems and how you present them in presentations and publications is among the most important things I learned during these years.

Dear Loredana Gastaldo, thank you for supporting me with my presentations at all these conferences and workshops. Especially for making the connection to Milano. The workshops you organized in Trento where those scientific events I enjoyed most.

Dear Antje Hoheisel and Heinrike Braß, thank you for proofreading my thesis and all your suggestions that made this work easier to read and better to understand.

Lieber Peter Braß, danke für deine zahlreichen Vorschläge zur Strukturierung der Abschnitte und Kapitel. Wann immer ich unentschlossen mit einer diesbezüglichen Entscheidung war, haben deine Argumente mich entweder in meiner Entscheidung bestärkt, oder eine bessere Alternative aufgewiesen.

Dear Simon Heinze, Moritz Drescher, Marc Merstorf and Kambis Veschgini, thank you for the amazing time at work, your support for code-development, all the discussions we had and for the time after work full of board-games and other activities.

So long, and thanks for all the cake.